LBL--15591

LBL-15591

DE83 011740

ATOMIC PHOTOELECTRON-SPECTROSCOPY STUDIES USING SYNCHROTRON RADIATION

Paul Harvey Kobrin
(Ph.D. Thesis)

Materials and Molecular Research Division
Lawrence Berkeley Laboratory
and
Department of Chemistry
University of California
Berkeley, California 94720

DISCLAIMER

This work was supported by the Director, Office of Energy Research, Office of Basic Energy Sciences, Chemical Sciences Division of the U. S. Department of Energy under Contract No. DE-AC03-76SF00098. It was performed at the Stanford Synchrotron Radiation Laboratory, which is supported by the NSF through the Division of Materials Research.

Table of Contents

ATOMIC PHOTOELECTRON SPECTROSCOPY STUDIES USING SYNCHROTRON RADIATION

Paul Harvey Kobrin

Materials and Molecular Research Division
Lawrence Berkeley Laboratory
and
Department of Chemistry
University of California
Berkeley, California 94720

Abstract

Photoelectron spectroscopy combined with tunable synchrotron radiation has been used to study the photoionization process in several atomic systems. The time structure of the synchrotron radiation source at the Stanford Synchrotron Radiation Laboratory (SSRL) was used to record time-of-flight (TOF) photoelectron spectra of gaseous Cd, Hg, Ne, Ar, Ba, and Mn. The use of two TOF analyzers made possible the measurement of photoelectron angular distributions as well as branching ratios and partial cross sections.

Dramatically different energy dependences of the partial cross sections for producing the lowest $^2D_{5/2}$, $^2D_{3/2}$, $^2S_{1/2}$, and $^2P_{3/2,1/2}$ ionic states of Cd^+ were observed for photon energies in the neighborhood of the $[4d^9(5s5p\ ^3P)]\ ^2P_{3/2}6s\ ^1P_1$ autoionization resonance at 588Å. Partial decay widths from the excited resonance state have been determined by fitting the resonance lineshapes to a theoretical

expression for the partial cross sections. Resonance profiles in the photoelectron angular-distribution asymmetry parameter for the $^2D_{5/2}$ and $^2D_{3/2}$ channels were also measured.

In Hg, the relative cross sections, subshell branching ratios and angular-distribution asymmetry parameters of the 4f, 5p, and 5d subshells were measured between 50 and 270 eV. In addition, the 4f asymmetry parameter was measured up to 600 eV. These quantities show dramatic effects accompanying Cooper minima in the 5d and 5p subshells and a large centrifugal barrier in the 4f → εg channel.

The feasibility of studying the energy dependence of core-level photoemission satellites in gases at high photon energies (up to 3320 eV) was shown in a study of the K-shell photoelectron satellites in Ne and Ar.

Photoelectron spectroscopy of Ba-5p hole states was studied in the energy range $20 \leq h\nu \leq 29$ eV. The variations of the $Ba^+ 5p^6nl$ (nl = 6s, 5d, 6p, 7s, and 6d) photoelectron peak intensities were measured in the 20-21 eV autoionization region. In addition, angular-distribution measurements were performed for the 6s, 5d, and 5p states. Above 21 eV, 5p ionization begins to dominate, and the Auger spectra were used to monitor the production of the various 5p-hole states.

The partial cross sections and photoelectron angular distributions for several lines in Mn have been measured near the 3p threshold at photon energies between 50 and 72 eV. A configuration-interaction analysis has been applied to help identify the origins of the observed 3d correlation satellites.

I. INTRODUCTION

In this dissertation atomic photoionization is studied using photoelectron spectroscopy combined with tunable synchrotron radiation. Photoelectron cross section and angular distribution measurements are reported from atomic Ne, Ar, Mn, Cd, Ba, and Hg. Interpretation of the experimental observations involves the effects of autoionization, electron correlation, and relativity.

The photoabsorption spectrum of an atomic system below its first ionization potential is characterized by a discrete set of symmetric absorption lines. The energies of each of these lines is equal to the excitation energy, E_{ni}, of a particular excited state, n, of the neutral atom:

$$h\nu = E_{ni} = E_n - E_i \qquad (1)$$

In the dipole approximation, the intensity of each of these photoabsorption lines is proportional to the square of a dipole matrix element between the ground and excited states,

$$f_{ni} = \frac{2m\nu}{3\hbar}\left|\langle \Psi_n^{(N)} \left| \sum_{\mu}^{N} r_\mu \right| \Psi_i^{(N)} \rangle\right|^2, \qquad (2)$$

where ν is the excitation frequency and Ψ_i and Ψ_n are the N-electron wavefunctions of the ground and excited states, respectively.

Photoabsorption well above the first ionization potential leads predominantly to photoionization. The photoemission spectrum at a given photon energy, $h\nu$, is known as the photoelectron spectrum, and it is characterized by a discrete set of photoelectron lines. The kinetic energy, ε_j, of each of these lines is related to the binding energy, I_j, of a particular state, j, of the ion by the relation

$$\varepsilon_j = h\nu - I_j \quad . \tag{3}$$

In the dipole approximation, the intensity of each of these photoelectron lines is proportional to the sum of the squares of dipole matrix elements between the initial ground state of the neutral atom and the final ion-electron continuum states. The cross section for producing the ionic state j is given by

$$\sigma_j(\varepsilon) = \frac{4\pi^2 \alpha a_0^2}{3}(\varepsilon + I_j)\sum_k |\langle \Psi_j^{(N-1)} \phi_k(\varepsilon) | \sum_\mu^N r_\mu | \Psi_i^{(N)} \rangle|^2 \quad , \tag{4}$$

where $\Psi_j^{(N-1)}$ is the wavefunction of the N-1 electron ion, $\phi_k(\varepsilon)$ is the wavefunction of the continuum electron, α is the fine structure constant (1/137), and a_0 is the Bohr radius.

In addition to its cross section, each photoelectron line has a spatial angular distribution that, for linearly polarized light, is of the form

$$\frac{d\sigma_j(\epsilon)}{d\Omega} = \frac{\sigma_j(\epsilon)}{4\pi}[1 + \beta_j(\epsilon)P_2(\cos\theta)] \quad , \tag{5}$$

where $\sigma_j(\epsilon)$ is the integrated cross section, θ is the angle between the photoelectron direction and the polarized photon electric vector, $P_2(x)$ is the second Legendre polynomial, and $\beta_j(\epsilon)$ is the asymmetry parameter. The angular distribution is completely characterized by $\beta(\epsilon)$, which can vary between -1 and 2. The continuum channels, k, contribute coherently to the asymmetry parameter as opposed to incoherently to the cross section in Eq. 4. The cross section and asymmetry parameter thus provide complementary information.

When the excitation energy of a discrete state of the neutral atom lies above the first ionization potential (ie. in the continuum) then the degenerate neutral and continuum states can mix. As a result of this mixing, photoabsorption at the excitation energy can lead to autoionization. Autoionization features appear as rapid variations in the otherwise slowly varying $\sigma_j(\epsilon)$ and $\beta_j(\epsilon)$ parameters. In addition, the mixing of the neutral and continuum states can lead to an asymmetric absorption feature and similarily to an asymmetric feature in the $\sigma_j(\epsilon)$ and $\beta_j(\epsilon)$ parameters.

Chapter VI is concerned with the autoionization structure found in the 5p excitation region of Ba. Barium autoionization is peculiar in that some of the absorption features lead to double ionization and the emission of two electrons.

In Chapt. III an asymmetric autoionizing feature in the Cd absorption spectrum is shown to produce distinctive profiles in each of the $\sigma_j(\epsilon)$ and $\beta_j(\epsilon)$ parameters. These profiles are shown to

contain unique information about the interaction of the quasi-bound state of the neutral atom and the numerous ion-electron continuum states.

Most portions of absorption spectra are devoid of narrow autoionizing resonances. The variations of the $\sigma_j(\varepsilon)$ and $\beta_j(\varepsilon)$ in these regions are due to the slow changes in the continuum wavefunctions, $\phi_k(\varepsilon)$. Accurate ab initio calculations of $\sigma_j(\varepsilon)$ and $\beta_j(\varepsilon)$ often require inclusion of relativistic and correlation effects. Several theoretical methods are currently being developed and tested by comparisons to atomic systems for which there are experimental data. Chapter IV is concerned with photoionization of Hg above $h\nu$ = 50 eV, a region in which there has been virtually no previous experimental work. As one of the heavy stable elements (Z = 80), Hg is a particularly important system in the study of relativistic effects.

The configurations of "main lines" in a photoelectron spectrum are obtained by the removal of one electron from the ground state configuration of the neutral atom. The configurations of smaller lines, known as "satellite lines," are obtained by removing one electron and promoting another. The creation of these satellite lines is said to involve the breakdown of the one-electron or single-particle approximation. In reality, the mechanism for creating satellite lines, a single photon excitation, is no different than the mechanism for creating the main lines. Equation 4 applies equally well to all photoelectron lines. A theoretical treatment of satellite lines requires the inclusion of the effects of electron correlation. In Chapt. V, the first energy-dependent studies of the K-shell satellites in Ne and

Ar are reported. Electron correlation also plays a prominent role in the creation of satellite lines in Ba (Chapt. VI). In Chapt. VII, a configuration interaction analysis is used to explain the satellite structure in Mn.

The following chapter presents some experimental details that are not presented elsewhere and that are common to the experiments that follow.

II. EXPERIMENTAL

The experimental aspects of this dissertation involve the coupling of a light source, a sample source, and an electron analysis technique. The light source is monochromatized synchrotron radiation, the sample source is an oven capable of producing metal vapors, and the electron analysis technique is the double-angle time-of-flight (DATOF) method. This chapter includes a description of the components as well as an indication of the manner in which the experiments were performed.

The TOF apparatus was built and tested by Mike White, Richard Rosenberg, and coworkers before I joined the research group. As an historical matter, Table I lists all of the experiments performed with the TOF apparatus prior to September 1982. The first successful experiments, in 1978 and 1979, involved the measurement of spectra at autoionizing resonances in atomic barium and the measurement of the β-parameter for the xenon 5s photoelectron near its Cooper minimum. Over the following three years, the apparatus was refined, the efficiency was improved, and experiments were completed on two dozen atomic and molecular systems. My emphasis during this time was on atomic metal vapors. One of my goals was to perform quantitative experiments on metal vapors, particularly angular-distribution measurements.

All of the experiments were performed at the Stanford Synchrotron Radiation Laboratory (SSRL), which is located at the Stanford Linear Accelerator Center (SLAC) 50 miles from Berkeley. The most valuable

commodity in this work is "beam time." This is the time allotted to our research group by the administration at SSRL. Beam time takes the form of short "runs" two to four times per year. Table I lists the runs that have involved the TOF apparatus. Each run lasts about two weeks, 24 hours a day, with perhaps a couple of days off in the middle. The efficient use of this valuable beam time was one of the criteria used in designing the equipment, in developing a data processing scheme, and in performing the experiments.

Four people were nominally required to execute the experiments. Two would work at night and two would work during the day. Figure 1 shows a photograph of the individuals who were involved in most of these experiments.

The virtues of synchrotron radiation from an electron storage ring have been described by Winick.[1] Briefly, the storage ring provides an intense radiation continuum that is highly polarized and time structured.

Figure 2 depicts the overall experimental scheme. Photon pulses having a ~0.3 nsec width and a 780 nsec repetition period are monochromatized before entering the sample chamber. The photoelectrons are then collected at two angles with respect to the photon polarization direction. The time-of-flight spectrum of these photoelectrons is equivalent to their kinetic-energy spectrum. Figure 3 shows how the electron signal is amplified by the dual microchannel-plate assembly and is then coincidenced with a signal from the electron storage ring.

With routing electronics, the signals from both analyzers are directed into the same time-to-amplitude converter and then into two different quadrants of an multichannel analyzer (MCA). A more complete description of the apparatus can be found in Ref. 2.

A. Monochromators and Windows

The radiation emitted from a storage ring bending magnet is dispersed by a monochromator that is suitable for a particular energy range. The three different monochromators used in this work are described in this section.

Between the 10^{-10} torr monochromator and our 10^{-4} torr vacuum chamber is a thin-film window. Both aluminum and vitreous carbon windows were used in this work and their transmission characteristics are described below. The 3/8 inch diameter windows are 1500Å thick, mounted on conflat mini-flanges, and are obtained from Luxel.[3] An interlock system involving ion gauges, two pneumatic gate valves and a few other valves and sensors is used to protect the UHV monochromator from a vacuum catastrophe. This interlock system has been described previously.[4] The only modification has been the interlocking of the chamber gate valve that protects the window from a vacuum failure in the main chamber.

8° line: This beam line, officially designated branch line I-2, has a 1-meter Seya-Namioka monochomator that is described by Rehn et al.[5] Without a window, this line is useful from 4 to ~34 eV and has a flux of $\sim 10^{10}$ photons/sec under typical operating conditions. The flux through the aluminum window is shown in Fig. 4. For the Ba

and Cd work done on this beam line, a fixed monochromator bandpass of 2.5Å FWHM was used.

4° line: Branch line III-1, known as the new 4°-line, has a grazing-incidence grasshopper monochromator that was used up to 600 eV for the Hg experiment. A detailed description of this monochromator can be found in Ref. 6. The monochromator has adjustable entrance and exit slits, an adjustable refocussing mirror, and two gratings interchangeable in vacuum. Both the Mn and Hg experiments were done with a 1200 l/mm holographically-ruled grating.

Both the aluminum and carbon windows were used on this beam line. The flux through these windows are shown in Fig. 5, which shows that the transmission of the carbon window is greater for energies between the aluminum $L_{2,3}$-edge at 72 eV and the carbon K-edge at 280 eV.

2° line: Branch line III-3 uses a double crystal monochromator, known as "Jumbo," that has been described by Hussain et al.[7] Jumbo holds up to four interchangeable sets of crystals. Beryl crystals that span the energy range between 800 and 1800 eV were used for the Ne experiment, and germanium crystals that span the range between 2000 and 4500 eV were used for the Ar experiment. The carbon window was used on this line because its transmission is >99% above 800 eV.

B. Metal Vapor Oven

To vaporize Ba, Cd, Mn and Hg (as well as Eu, Sm, Tm and Li to date), a resistively-heated inductively wound oven was used. The basic criteria for this oven are:

i) To attain a temperature of 1000°C.

ii) To avoid creating any electric or magnetic fields in the interaction region.

iii) To contain sufficient sample in order to operate for 24-72 hours without refilling.

iv) To be able to flow gas through the same orifice for calibration purposes.

v) To keep most of the metal vapor from reaching the channel plate detectors and the thin film window.

vi) To be able to introduce the oven into the chamber easily and quickly.

vii) To be able to change metal samples easily and quickly, without changing the alignment of the oven.

The oven went through several design changes during my tenure. The first design failed criterion (iv) during the TOF-8 run when condensed Ba clogged the gas passage. The second design is shown as Fig. 1 of Chapter III, and Figs. 6-9 of this chapter are pictures of the oven. The clogging problem was overcome by the use of an active valve that is opened and closed from outside the chamber.

The outer-body piece was made from 304 stainless steel prior to TOF-12, when it was replaced by a molybdenum piece. While molybdenum can be used to higher temperatures, 304 stainless steel has the advantage that it is impervious to nitric acid, thus simplifying cleaning. The use of a large diameter body allows for a large sample volume (3.5 cc), while the smaller diameter nozzle is necessary to get as close as possible to the interaction region.

Starting with TOF-12, the external heating wires were purchased with an enclosed connection at one end and enclosed transitions to thicker nickel wires at the other end. The wires were made of Nichrome V with MgO insulation and an Inconel sheath. Other materials that can safely operate at higher temperatures could be used in the future. Three or four of these heating wires have provided up to 200-400 watts.

To help keep the metal vapor from reaching the critical elements in the chamber, an unheated skimmer was used starting with TOF-12. The skimmer has a 7 mm diameter opening and only intersects the metal atoms having a trajectory greater than 60° from the normal. The large size of this opening keeps it from clogging. For the Hg experiment, where clogging from condensed liquid was not a problem, a smaller, 5 mm diameter skimmer that intersected trajectories greater than 45° was used.

To protect the turbomolecular pump on the main chamber from being coated with condensed metal, a 1000 liter/sec cryopump[9] was purchased. Using two 10 inch conflat gate valves,[10] the turbomolecular pump can be used to pump gases when the oven is cold, and then isolated from the chamber when the oven is hot.

To reach temperatures above 800-900°C (i.e., to vaporize Mn), additional heating power was required. To accomplish this, an inner oven that has the same size as the normal sample cup (Fig. 1, Chapt. III) was built. The inner oven (Fig. 10) has an Al_2O_3 core around which tungsten heating wires are noninductively wound. An Al_2O_3 tube around the heating wires serves to shield the wires from metal

vapor. The inner oven is supported by a stainless steel tube through which travel two shielded power leads. These leads are connected to the tungsten heating wires by a set of molybdenum pins. The metal sample is put into a mullite sample cup which fits into the inner oven. The inner oven provided ~100 watts during the Mn experiment.

Up to and including TOF-12, the oven was mounted on a homemade XYZ stage mounted on a 2-3/4 inch diameter flange on the bottom of the main chamber. The only problem with this configuration was that the Z-motion of the XYZ stage was not truly decoupled from the XY-motions. When a 6 inch long stainless steel oven is heated to 1000°C, it lengthens 3 mm (1 mm if it is made of molybdenum). Since it is desirable to put the oven as close as possible to the photon beam (i.e., 1-3 mm away), the cold oven must be positioned 3-5 mm out of the beam. Had the oven expanded into the photon beam, it would have been necessary to change the Z position while the oven was hot, which would have disturbed the XY alignment. Although this never occurred, the possibility of it occurring prompted us to commandeer an old UHV Varian XYZ stage for the project. This stage allows the Z-motion to be decoupled from the XY-motion.

It proved to be good practice to do experiments with room temperature gases at the beginning of a run, with the gas inlet described by White,[2] and to do experiments on metal vapors at the end. This allowed the bugs to be worked out of the rest of the system while the well-behaved gases were being used, and allowed the room temperature gas experiments to be completed before the window and detectors could be coated with metal.

C. TOF Analysis

Figure 11 shows one of the two TOF analyzers. Their design has been described by White et al.[2] Each analyzer has several grids and an electrostatic cage that allows a constant potential to be applied for two-thirds of the flight path. Figure 12 is a schematic of the potential system. In the absence of any applied potential, the flight time, T, is given by

$$T = \frac{KL_T}{E^{1/2}} \tag{1}$$

where L_T is the total path length (~28 cm), E is the electron kinetic energy, and K is a constant. This equation can easily be inverted to solve for E(T).

When a potential, V, is applied to the electrostatic cage, the time-of-flight is given by

$$T = \frac{KL_1}{E^{1/2}} + \frac{KL_3}{(E-V)^{1/2}} + \frac{K(L_2+L_4)}{V}\left[(E+V)^{1/2} - E^{1/2}\right] \tag{2}$$

where the first term is the flight time through the initial field-free region, the second term is the flight time through the electrostatic cage, and the third term is the sum of the flight times through the accelerating and decelerating regions. Equation 2 cannot be inverted to solve for E(t), so an iterative method is used.

To transform a time spectrum into an energy spectrum requires knowing the prompt channel (i.e., the zero time) and the distance L_1. All other quantities are known. When the inside of the chamber becomes

coated with a metal sample, a contact potential may develop between the interaction region and the inside of the analyzer drift tube. To account for this, a fitted contact potential parameter (of up to 2 volts) is added to E in Eq. 2.

The resolution of the TOF analyzer is limited by the time width of the ~0.3 nsec light pulse and the ΔL uncertainty in the initial position of the electron, caused by the finite size of the interaction region. The performance of the TOF analyzer on the 8° line with no retarding potential has been discussed by White et al.[2] For kinetic energies, E, less than ~100 eV, the resolution $\Delta E/E$ is essentially constant, and equal to $2\Delta L/L_T$. On the 4° and 8° lines, this fraction is usually 2.5%-3.5% for each analyzer, while it is closer to 5% on the 2° line, where the horizontal focus is larger.

When a positive or negative potential, V, is applied to the electrostatic cage, the total time-of-flight is changed but the time uncertainty, due to the finite interaction volume, remains the same. The theoretical resolution, with a potential applied to the electrostatic cage, is shown in Fig. 13. Figure 13 is a plot of $[\Delta E/(E-V)]/(2\Delta L/L_T)$ versus V/E, which allows all values of E and V to be represented by one curve. The quantity $\Delta E/(E-V)$ is found to be relatively constant from $-0.5 < V/E < 1.0$. Thus, a 100 eV electron that is retarded by 50 volts will have slightly better resolution (ΔE) than a 50 eV electron for which no retarding is applied.

For a given photoelectron line to maintain a constant resolution, ΔE, one would want to have nominally a constant E-V. This mode of

operation, called "constant final kinetic energy," was used for the Hg experiment to resolve the 4f-doublet at most photon energies.

In the absence of retarding, the transmission of our TOF analyzer is essentially constant, except at low kinetic energies, where the effects of stray fields become more important. The analyzers have several apertures that define the 3° acceptance angle. When a retarding potential is applied to the electrostatic cage, the transmission of the analyzer decreases because of lensing at the first pair of grids. The curve in Fig. 14 shows the theoretical and experimental transmission as a function of (E-V)/E, where the retarding potential, V, is taken to be a positive quantity. Note that the decrease in transmission is predicted to be less than the fraction (E-V)/E. The transmission was measured during the TOF-9 run on the 2° line and during the TOF-12 run on the 4° line. While agreement with theory is poor, considering the transmission as a function of (E-V)/E has helped to decrease the number of calibration points necessary.

The Double-Angle Method. The differential cross section for photoionization from a randomly oriented sample with linearly polarized light has been given in Chapt. I. With one detector at $\theta = 0^\circ$ and one at $\theta = 54.7^\circ$, the asymmetry parameter is given by

$$\beta(E) = -1 + \frac{N(0^\circ, E)/N(54.7^\circ, E)}{f(E)}$$

where $N(\theta,E)$ is the number of electrons detected and $f(E)$ is the relative collection efficiency of the two analyzers. Calibration of $f(E)$ is made by measuring photoelectron lines with known $\beta(\epsilon)$'s. Corrections to this scheme have been discussed by Southworth et al.[10]

These corrections account for the finite collection solid angle, finite source volume, and imperfect linear polarization of the light. The corrections are generally less than 0.03 β-units.

On the 8° line, measurements of f(E) are made using He and a 1:1:1 mixture of Ar, Kr and Xe. This rare-gas mixture provides five calibration lines simultaneously. (The Ar doublet is usually not resolved.) On the 4° line, the Ne 2s and 2p lines are used for calibration.

D. Data System

During the last three years, the data acquisition and processing system was upgraded immensely. Originally (before TOF-5), the data was accumulated in a Hewlett Packard MCA, dumped to magnetic tape that could be read by the large LBL mainframe computers, and transferred to an Intel 8010 microprocessor that was operated by a 110 baud teletype. The first addition was an HP-7220A digital plotter that could plot two 1024-channel spectra in under 3 minutes. The plotter, that has digitizing capabilities, was also used to define the integration regions of the spectra. Then a Digital Equipment Corp. LSI-11/23 computer was obtained. The new computer enabled us to run a more sophisticated operating program, increase our speed, and store data on floppy disks for easy access back in Berkeley. A Canberra Series 40 MCA later replaced the HP MCA. The new MCA provided a faster method for defining the integration regions and allowed for more automated data acquisition. The present state of the data processing system includes a sophisticated operating program, a high speed line printer, and two

computer interfaced scalers that monitor the gas pressure and phcton intensity. There is now less than 1 minute of down time between spectra, and it is not difficult for one hurried person to keep things going, though not indefinitely.

REFERENCES

1. H. Winick, in Synchrotron Radiation Research, H. Winick and S. Doniach, eds. (Plenum, New York, 1980).

2. M. G. White, R. A. Rosenberg, G. Gabor, E. D. Poliakoff, G. Thornton, S. H. Southworth, and D. A. Shirley, Rev. Sci. Instrum. 50, 1268 (1979); M. G. White, Ph.D. thesis, University of California, Berkeley (1979), Lawrence Berkeley Laboratory report No. LBL-9527.

3. Luxell Corporation, Friday Harbor, Washington.

4. R. A. Rosenberg, Ph.D. thesis, University of California, Berkeley (1979); Lawrence Berkeley Laboratory report No. LBL-8948.

5. V. Rehn, A. D. Baer, J. L. Stanford, D. S. Kyser, and V. O. Jones, in VUV Radiation Physics, E. Koch, R. Haensel, and C. Kunz, eds. (Pergamon-Vieweg, London/Braunsweig, 1974), p. 780.

6. F. C. Brown, R. Z. Bachrach, and N. Lien, Nucl. Instrum. Meth. 152, 73 (1978).

7. Z. Hussain, E. Umbach, D. A. Shirley, J. Stohr, and J. Feldhaus, Nucl. Instrum. Meth. 195, 115 (1982).

8. SEMCO, Inc., Hollywood, California.

9. CTI-Cryogenics, Waltham, Massachusetts.

10. S. Southworth, C. M. Truesdale, P. H. Kobrin, D. W. Lindle, W. D. Brewer, and D. A. Shirley, J. Chem. Phys. 76, 143 (1982).

Table I. Time-of-flight runs

Date	Run	Samples	Beam Line	Participants[a]
F 78	2	Ba	8°	MW, RR, EP, GT, SS
Sp 79	3	Xe	8°	MW, RR, EP, SS, PK, DL
Sp 79	4	Xe, HI	8°	MW, RR, EP, SS, PK, DL
F 79	5	H_2	8°	SS, PK, CT, DL, WB
Sp 80	6	H_2, D_2, H_2O, CS_2 CO_2, N_2O, NO, OCS	8°	SS, PK, CT, DL
Sp 80	7	Xe	4°	SS, PK, CT, DL, SO
Sp 80	8	Ba	8°	SS, PK, CT, DL
Sp 81	9	Ne, Ar	2°	SS, PK, CT, DL, UB
Sp 81	10	Xe, CO	4°	SS, PK, CT, DL, UB
Sp 81	11	CO_2 OCS, Cd, Ba, CH_3I, CH_3Br	8°	SS, PK, CT, DL, UB
F 81	12	CO, CO_2, He, Ne, Mn, N_2	4°	PK, CT, DL, UB, HK
Sp 82	13	Kr, CH_3I, CF_4, NO, OCS, Hg, Eu	4°	PK, CT, DL, UB, HK, TF, PH

[a] MW=Mike White, RR=Richard Rosenberg, EP=Erwin Poliakoff, GT=Geoff Thornton, SS=Steve Southworth, PK=Paul Kobrin, DL=Dennis Lindle, CT=Carlton Truesdale, WB=William Brewer, SO=Shige Owaki, UB=Uwe Becker, HK=Hans Kerkhoff, TF=Trish Ferrett and PH=Phil Heimann.

FIGURE CAPTIONS

Fig. 1 Picture taken spring 1981 at SSRL. From left-to-right: Carlton "Trues" Truesdale, Dennis Lindle, Uwe Becker, Steve Southworth, and Paul Kobrin.

Fig. 2 Schematic of the double-angle time-of-flight (DATOF) method.

Fig. 3 Schematic of one of the TOF analyzers with associated electronics. A = 1 MΩ, B = 422 kΩ, C = 1 MΩ, D = 619 kΩ, E = 750 kΩ. MONO = monochromator. CS = ceramic spacer. MS = mylar spacer. MCP = 40 mm diameter microchannel plate. DC = decoupling capacitor. CA = coaxial anode. DT = decoupling transformer. CFD = constant fraction discriminator. Attn = attenuator. DD = differential discriminator. TAC = time-to-amplitude converter. PHA/MCA = combination pulse hight analyzer and multichannel analyzer.

Fig. 4 The photon flux as a function of wavelength on the 8° line after passing through an aluminum window. Measured using a sodium salycilate VUV-to-visible converter and an RCA 8850 photomultiplier tube calibrated with an NBS photodiode.

Fig. 5 The photon flux as a function of energy on the 4° line after passing through an aluminum (solid curve) or a carbon window (dashed curve). The first order flux through the carbon window is shown as a dotted curve. The relative scaling of the solid and dashed curves is estimated to be within 10%. The intensities were measured using a sodium salycilate scintillator and fixed monochromator slit settings which

corresponds to a fixed $\Delta E/(E)^2$. The minimum in the Al curve near 280 eV is due to the K-edge absorption of carbon deposited on the optical surfaces of the beam line.

Fig. 6 Parts of the metal vapor oven. On the left: two heating cables wound into a double-helix. Center-bottom: the metal outer structure, sample cup, and stainless-steel foil heat shield. Center-top: the nozzle heating cable. Right: three pieces of alumina heat shielding.

Fig. 7 Parts of the metal vapor oven: the sample cup, outer structure, and heating cables.

Fig. 8 Partially assembled oven, showing heating cables and outer support stalk.

Fig. 9 Fully assembled oven.

Fig. 10 The inner oven. The inner-oven shield, ceramic body and conductor set pin are made of Al_2O_3; the intermediate conductor and filament screws are made of molybdenum; and the heating supply screws and support stalk are made of 304 stainless-steel.

Fig. 11 The disassembled TOF analyzer, showing (from left-to-right) one of two μ-metal shields, detector/electron multiplier and gold-plated aluminum drift tube with defining aperture. The retarding cage is the top-third of the center structure.

Fig. 12 Schematic of the TOF analyzer showing dimensions relavent for time-to-energy conversion.

Fig. 13 The theoretical resolution of the TOF analyzer. E is the electron kinetic energy and V is the potential of the electrostatic cage. The positive values of the ordinate correspond to accelerated electrons.

Fig. 14 The theoretical and experimental transmission of the TOF analyzers. The retarding potential V is a positive quantity. The open circles were obtained during TOF-9 and the X's were obtained during TOF-12.

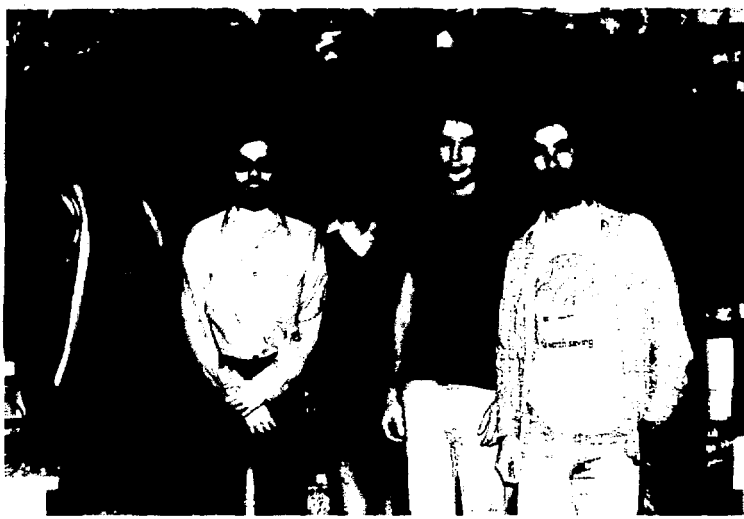

XBB 815-4402

Fig. 1

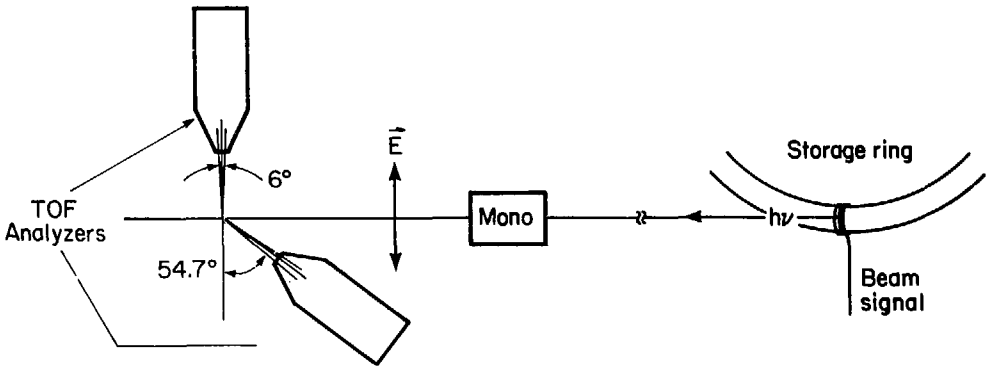

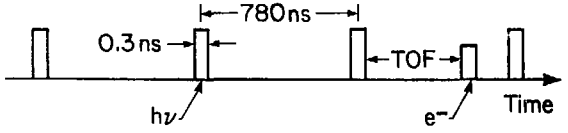

Fig. 2

XBL 7910-4225

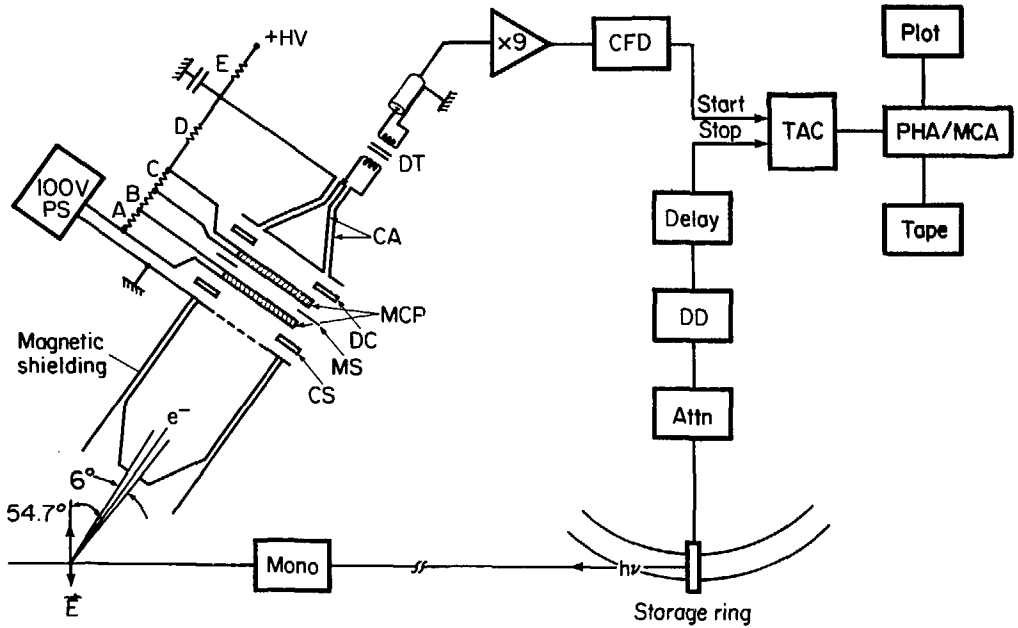

Fig. 3

XBL 792-619

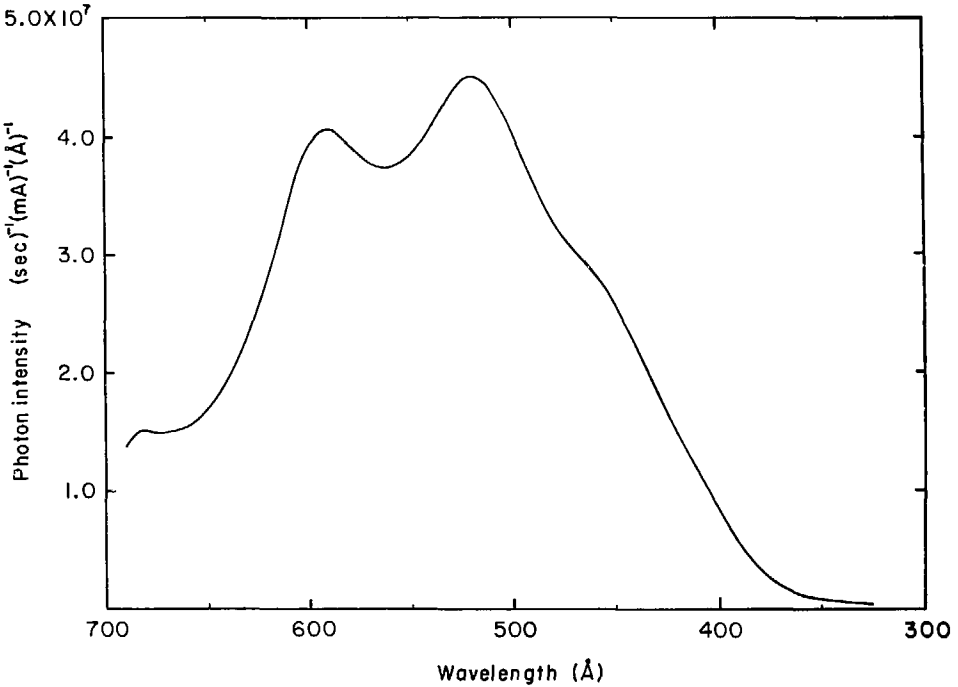

Fig. 4

X8L 809-11808

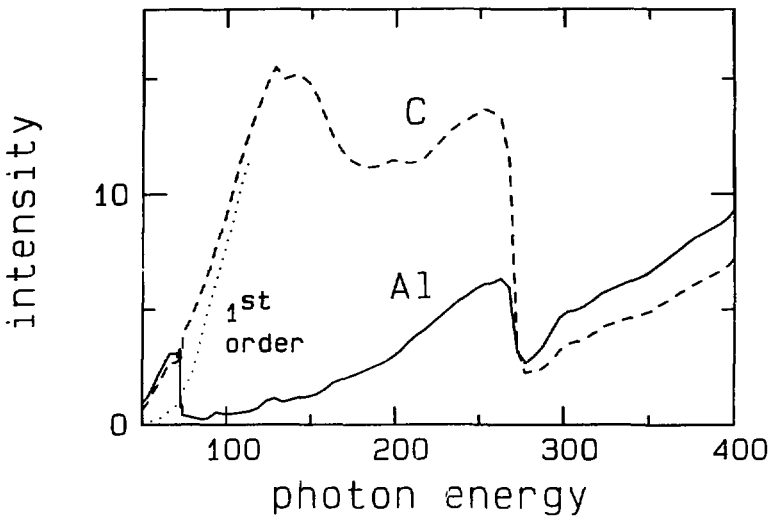

XBL 821-7927

Fig. 5

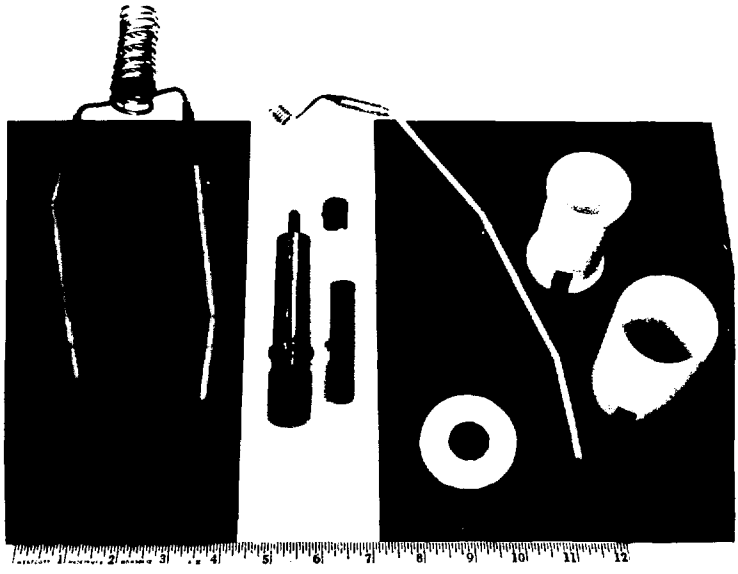

CBB 810-9600

Fig. 6

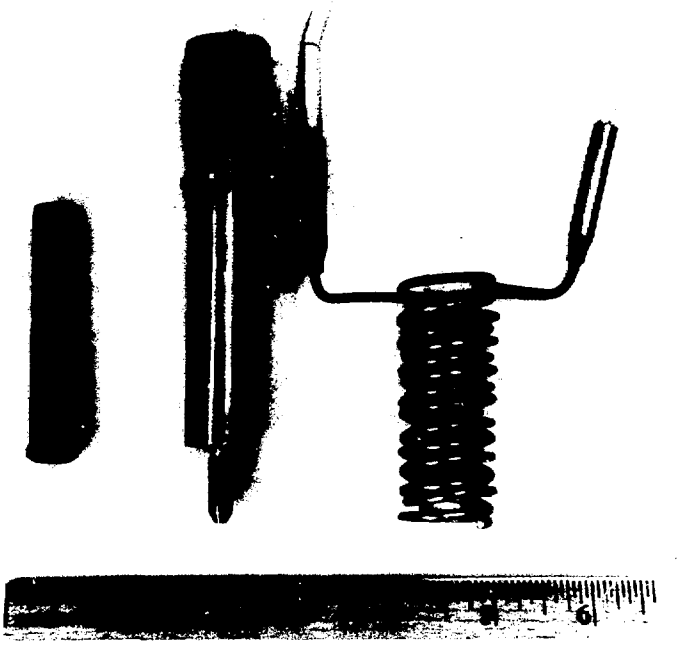

CBB 810-9602

Fig. 7

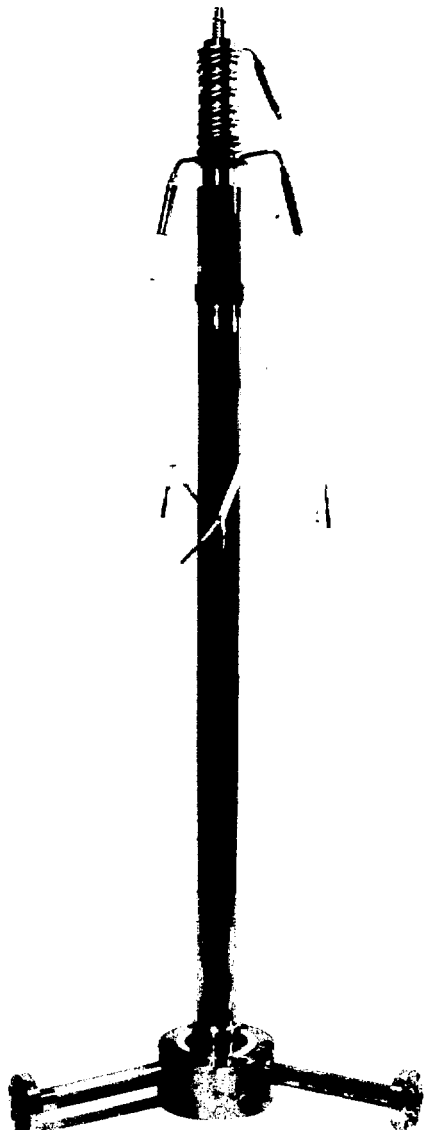

Fig. 8 CBB 810-9596

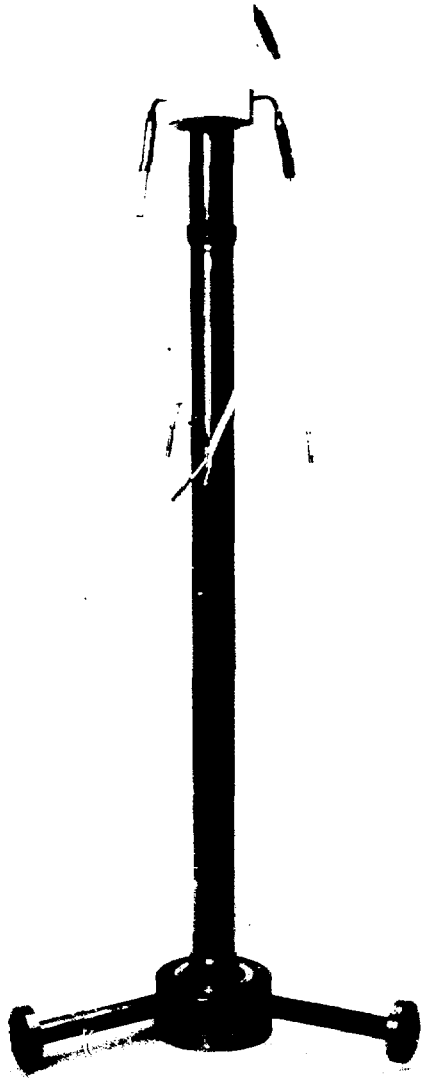

Fig. 9 CBB 810-9598

INNER OVEN

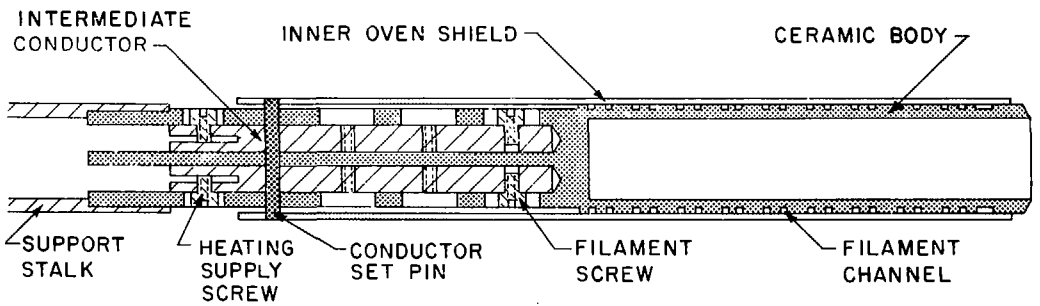

Fig. 10

XBL 831 - 23

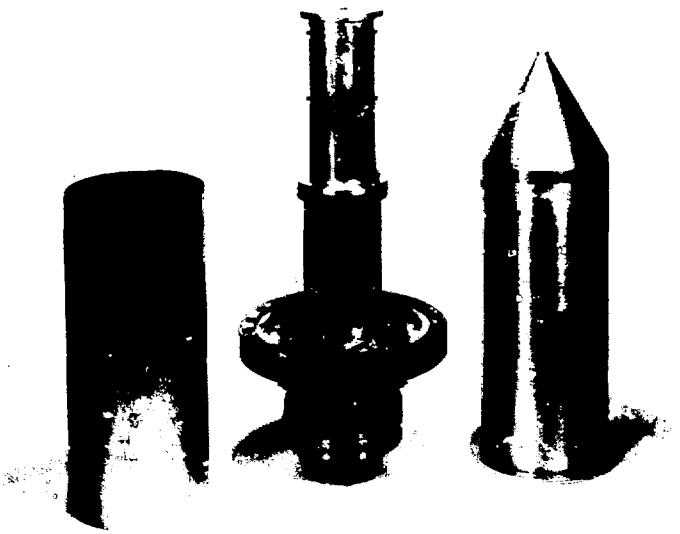

CBB 793-3980

Fig. 11

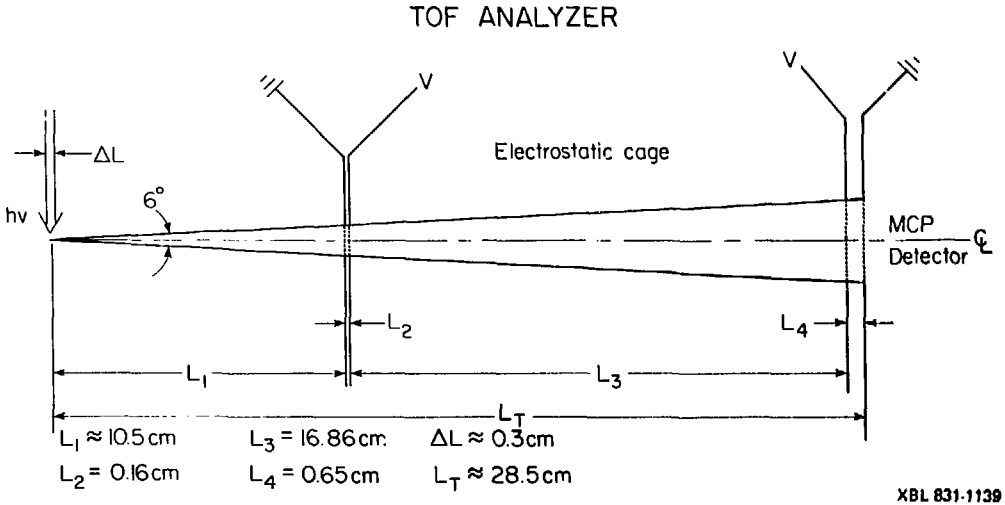
TOF ANALYZER
V
V
Electrostatic cage
ΔL
hv
6°
MCP
Detector
L2
L4
L1
L3
LT
L1 ≈ 10.5 cm
L3 = 16.86 cm
ΔL ≈ 0.3 cm
L2 = 0.16 cm
L4 = 0.65 cm
LT ≈ 28.5 cm
XBL 831-1139

Fig. 12

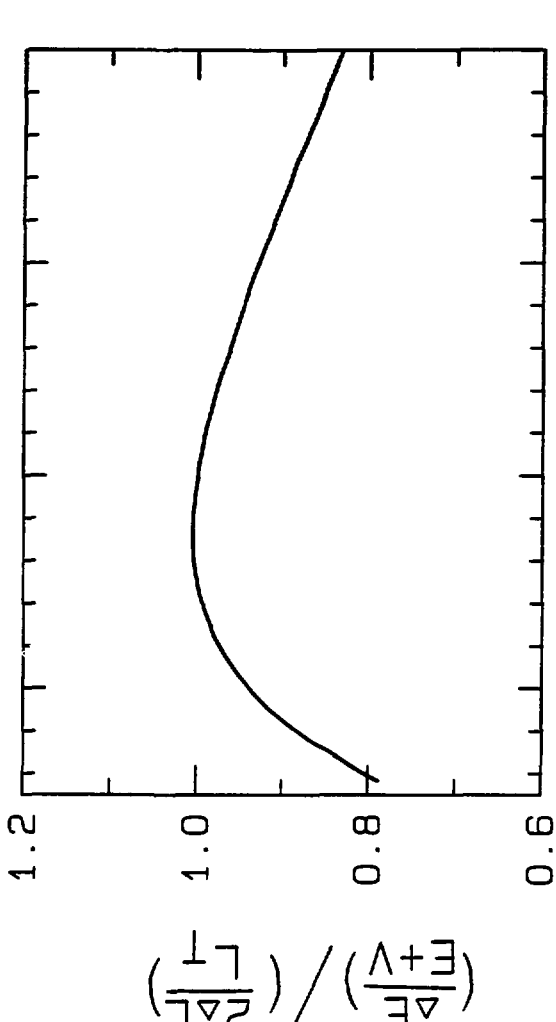
1.2
1.0
0.8
0.6
-0.5
0.0
0.5
1.0
V/E
$\left(\frac{\Delta E}{E+V}\right) / \left(\frac{2\Delta L}{L_T}\right)$
XBL 831-7928

Fig. 13

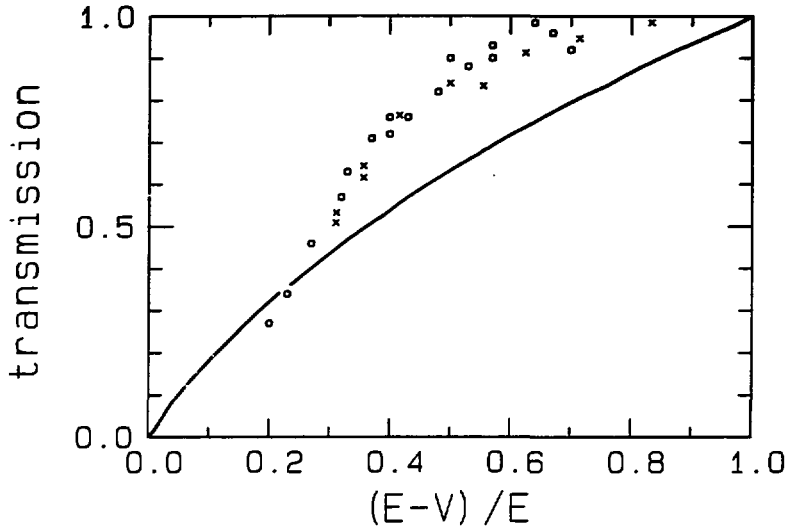

XBL 831-7925

Fig. 14

III. AUTOIONIZING RESONANCE PROFILES IN THE PHOTOELECTRON SPECTRA OF ATOMIC CADMIUM*

ABSTRACT

Photoelectron spectra have been taken of atomic Cd with synchrotron radiation between 19 and 27 eV using the Double-Angle Time-of-Flight method. Dramatically different energy dependences of the partial cross-sections for producing the lowest $^2D_{5/2}$, $^2D_{3/2}$, $^2S_{1/2}$, and $^2P_{3/2,1/2}$ ionic states of Cd^+ were observed for photon energies in the neighborhood of the $[4d^9(5s5p\ ^3P)]\ ^2P_{3/2}6s\ ^1P_1$ autoionizing resonance at 588Å. Partial decay widths from the excited resonance state have been determined by fitting the resonance lineshapes to theoretical expressions for the partial cross-sections. Resonance profiles in the photoelectron angular-distribution asymmetry parameter for the $^2D_{5/2}$ and $^2D_{3/2}$ channels are also reported. The $^2P_{3/2,1/2}$ satellite is found to decrease slightly relative to the $^2S_{1/2}$ main line in the 19-25 eV range. Three new satellite peaks have been detected with intensities enhanced by autoionization.

A. INTRODUCTION

In recent years considerable effort has been spent elucidating several aspects of Cd I photoionization. Much interest has been focused on the excitation of 4d electrons, which are affected by both intrashell and intershell correlations, and on the intermediate-Z nature of Cd, which cannot be treated satisfactorily in either a pure LS or jj coupling scheme.

Many-body-perturbation theory (MBPT)[1] has been used to calculate the absolute photoionization cross-section measurements,[2,3] which could not be described correctly by single-electron calculations. Harrison's[4] early angular distribution measurements of the 4d photoelectrons using a He I source (584Å) prompted theoretical investigations based on MBPT,[1] the Dirac-Slater (DS) approximation,[5] the Dill-Fano angular momentum transfer approach,[6] and Dirac-Fock (DF) theory.[7] Recently new experimental measurements with resonance lamps[8] have shown better agreement with the calculations.

The role of relativistic effects was investigated by Walker and Waber,[5] who examined the Cd 4d branching ratio by making Dirac-Slater calculations. Their work suggested that most of the variation from the statistical value is due to the difference in kinetic energies of the two spin-orbit split components at a fixed photon energy. Measurements with synchrotron radiation[9] and recent Dirac-Fock calculations[10] have also addressed this problem.

Alignment in the Cd^+ $^2D_{3/2}$ and $^2D_{5/2}$ states produced through photoionization with He I radiation has been detected[11,12] by measuring

the degree of linear polarization of the flourescence to the Cd^+ ground state. Comparisons with MBPT,[1] Hermann-Skillman[13] and relativistic DF[7] calculations have left some discrepancies.

The nature of the satellite peaks in the photoelectron spectra of Cd^+ and other group IIA and IIB elements has been of interest because of the possibility of using them to study electron correlations.[14,15] Agreement of satellite intensities with the initial-state configuration interaction (ISCI) model, using multi-configuration Hartree-Fock (MCHF) calculations, has not been good.[16]

An investigation with synchrotron radiation revealed resonances in the Cd I absorption spectrum, corresponding to double electron excitations in a single-particle picture.[17] These excitations have been attributed to excited-state configuration mixing.

The effects of autoionizing resonances on absorption spectra were treated in the pioneering work of Fano.[18,19] Their effects on the more sensitive photoelectron spectrum have also been explored theoretically.[20-22] Most experiments to date on atomic systems have been concerned with the Rydberg states of rare gases between the first and second ionization thresholds, where only one final state is produced.[23] More tantalizing data have been obtained beyond the second ionization threshold in atoms[24] and in molecules where the problem is theoretically intractable.[25,26]

The fortuitous overlap of the He I line with an autoionizing level of Ba I was found to enhance many of the otherwise weak satellite lines.[27-29] Synchrotron radiation was subsequently used to excite

resonances in atomic barium[30] and more recently in atomic copper,[31] in order to study the structure of the autoionizing levels and their interaction with the continua.

This experiment on Cd was prompted by a desire to study several final ionic states in the neighborhood of a broad autoionizing resonance. Metal vapors provide some of the best resonances for such a study, and the 588Å feature in the Cd I absorption spectrum was chosen as an especially promising case. We report here the largest set of partial cross-section and angular distribution profiles yet obtained for an atomic autoionizing resonance. In particular, the partial cross-section profiles for the $(4d^{10}5s)\ ^2S_{1/2}$, $(4d^9 5s^2)\ ^2D_{5/2}$, $(4d^9 5s^2)\ ^2D_{3/2}$, $(4d^{10}5p)\ ^2P_{3/2}$, and $(4d^{10}5p)\ ^2P_{1/2}$ ionic states, as well as the angular distribution asymmetry profiles of the $(4d^9 5s^2)\ ^2D_{5/2}$ and $(4d^9 5s^2)\ ^2D_{3/2}$ photoelectrons, have been measured in the region of the 588Å resonance. Three heretofore unobserved satellite peaks were also detected at several photon energies between 22 and 24 eV.

Our experimental procedures are described in Section B. The nonresonant measurements of the 4d and 5s photoelectrons are presented in Section C. Section D addresses the effects of the 588Å resonance, the correlation satellite intensities are presented in Section E, and our conclusions are summarized in Section F.

B. EXPERIMENTAL

The partial cross-sections and angular distributions of the Cd photoelectrons were measured by the double-angle time-of-flight (DATOF) method, using the pulsed synchrotron radiation from SPEAR at the Stanford

Synchrotron Radiation Laboratory.[32] The vacuum of the SPEAR ring was isolated from our sample chamber by a 1500Å thick aluminum window. The light was monochromatized (2.5Å FWHM) by the Seya-Namioka monochromator on the 8° beam line. The two time-of-flight (TOF) detectors were placed at 0° and 54.7° (the "magic angle") with respect to the polarization direction of the >97% polarized synchrotron radiation, allowing us to make partial cross-section and angular distribution measurements simultaneously.

Our TOF photoelectron spectrometer has been described previously.[32,33] It is ideally suited for studying the low-intensity photoelectrons from metal vapors because of its high efficiency and excellent signal-to-noise ratio. Without retarding, the analyzers have a resolution equal to ~3% of the kinetic energy. The standard gas inlet was replaced by a new stainless-steel effusive oven with a 1-mm diameter orifice, noninductively wound heater cables, and alumina insulation. To do quantitative experiments with the TOF spectrometer it is necessary to admit calibration gases through the oven's orifice. A potential problem with having a passage for the calibration gas is that the metal vapor may condense in and eventually clog the passage. This problem is most acute for those metals which form low-density solids upon condensation (such as barium). To circumvent the problem an active valve was designed to close the gas passage when it was not in use.

The oven (Fig. 1) consists of an outer stainless steel cylindrical piece which includes the orifice and onto which are fixed the Semco heating cables[34] and alumina heat shields. Except for the orifice, the outer structure is gas-tight. The inner stainless-steel structure consists of the sample cup, which is screwed to a long rod that extends outside the chamber. The valve seal is made between the top of the sample cup and the outer oven wall, thus confining the metal vapor to the sample cup and oven orifice. This design also allows the sample cup to be removed for refilling without changing the alignment of the oven with respect to the analyzers and photon beam. It was not necessary to refill the Cd oven during the work reported here, as the 3.5 cc capacity of the sample cup was adequate for 24 hrs of operation. An oven temperature of approximately 300°C (corresponding to a Cd vapor pressure of ~0.1 torr) was monitored by two thermocouples, one mounted on the exterior of the outer structure, the other near the base of the sample cup. It was necessary to use the thermocouple readings to make small pressure corrections to the partial cross-sections. The angular distribution and branching ratio measurements do not require corrections for pressure or photon flux when the DATOF method is used.[33]

The synchrotron light intensity was monitored by a sodium salicylate scintillator and an optical phototube separated by a 300-500 nm bandpass filter. With the sodium salicylate fluorescence maximum at 420 nm we were able to filter out enough of the oven's black-body radiation to continue monitoring the synchrotron radiation while the oven was hot.

The main chamber was pumped by a 1000 ℓ/sec cryopump and a 500 ℓ/sec turbomolecular pump, which was valved off while the oven was in use to avoid metal vapor contamination. The chamber pressure was 1×10^{-5} torr when no calibration gas was flowing and below 1×10^{-4} torr whenever gas was flowing. For internal calibration many of the Cd^+ spectra were taken with a small amount of argon present. The $Ar^+ {}^2P_{3/2,1/2}$ peaks do not overlap any of the Cd^+ peaks, as shown in Fig. 2.

The error bars on our results represent counting statistics only. Uncertainties arising from background subtraction are negligible for the 5s, $4d_{5/2}$ and $4d_{3/2}$ main lines but could be significant for the weaker satellite lines. Systematic errors in both the "magic angle" analyzer transmission function used to derive branching ratios and partial cross-sections, and in the relative analyzer transmission function used to derive the angular-distribution asymmetry parameter, β, should be small and should vary slowly with photoelectron energy.

C. ASYMMETRY PARAMETERS AND BRANCHING RATIO OF THE 4d PEAKS

From the work of Mansfield[17] we know that the 20.5 - 24.5 eV region of the absorption spectrum of Cd I is densely populated by autoionizing features. At these resonances large variations can be expected in the 4d branching ratio and the angular-distribution asymmetry parameters, which would otherwise be slowly varying functions of energy. The values observed experimentally for these parameters are thus dependent on the excitation bandwidth, which will determine the extent of the averaging over direct and resonant processes. Calculations which do not

include any resonant effects should be more directly comparable with measurements outside of the 20.5 - 24.5 eV region.

The angular distributions of the $4d_{5/2}$ and $4d_{3/2}$ photoelectrons have been calculated and measurements have been made previously at several rare-gas laboratory-source energies between 21.22 and 40.81 eV. We report here the first measurements of these angular distributions using continuously tunable synchrotron radiation. Our results are shown in Fig. 3.

Figure 3 is divided into three panels for clarity. The parameters $\beta(4d_{5/2})$ and $\beta(4d_{3/2})$ are presented in panels (a) and (b), respectively, with a common photon-energy axis as abscissa. Identical curves have been drawn in Figs. 3(a) and 3(b). These curves have no theoretical significance but are given to guide the eye. The data fall into two sets: those outside the 588Å resonance region which follow the curve to a fair degree of accuracy, and those near resonance, which depart sharply from this curve. To compare the two asymmetry parameters further, we have deleted the "resonance" points and replotted the rest in Fig. 3(c) with a kinetic-energy abscissa. The 588Å resonance region is discussed in Section D of this paper.

Before proceeding, it is useful to state a caveat regarding this type of separation of photoemission data into resonant and nonresonant energy regions. The separation is, of course, arbitrary, but this is only a numerical problem. For example, a resonance energy "region" can be defined as extending some number of resonance bandwidths. Of more practical concern, the observation or nonobservation of a reso-

nance depends on the bandwidth of the excitation radiation. Care is thus needed in comparing data from different laboratories. More vexing is the residual doubt about whether a data point "off the curve" represents a resonance or just a bad measurement. The data sets presented in this paper often show scatter which appears to exceed the statistical errors. While we always tend to suspect unknown errors, which are difficult to rule out in synchrotron radiation studies because of possible fluctuations in the beam position, there is also the possibility that some of the deviant points arise from weak resonances.

From Fig. 3(c) we note that our data show good agreement with the six points given by Schönhense, which are, on the average, slightly lower than ours. From Figs. 3(a) and 3(b), comparison at equal photon energies gives, on the average, $\beta(4d_{3/2}) > \beta(4d_{5/2})$. However, this is a small effect, which disappears when the comparison is made at equal kinetic energies, as shown in Fig. 3(c). The theoretical curves predict the β values qualitatively, but deviate systematically in a quantitative comparison. The increase in the experimental β values at low energies is stronger than predicted by any of the theories. The data do not confirm the difference between $\beta(4d_{5/2})$ and $\beta(4d_{3/2})$ predicted by the Dirac-Fock theory in Fig. 3(c). Finally we note, but do not show, that Schönhense's data at kinetic energies above 10 eV rise well above the Dirac-Fock curves.

The Cd 4d branching ratio $\sigma(4d_{5/2})/\sigma(4d_{3/2})$ has been calculated by the Dirac-Slater[5] and Dirac-Fock[10] methods and has been measured previously at 21.22, 40.81, and 48.37 eV with resonance lamps[14,37] and between 19 and 30 eV with 6Å bandpass synchrotron radiation.[9] Our

measurements with a 2.5Å bandpass are shown, along with the previous results, in Fig. 4. Our results show the effect of the 588Å resonance for the first time in some detail. Outside the resonance region our data tend to confirm the earlier synchrotron radiation work. The scatter in our results in the $h\nu$ = 22-24 eV region may arise in part from additional resonances, as discussed above.

Both calculations fail to predict the continued rise in the branching ratio below 20.5 eV, while above 24.5 eV the DS curve is a little too high and the DF curve is a little too low. The poor agreement of the DF calculations at the low kinetic energies has been attributed to the use of jj coupling for this intermediate-Z atom. The DF calculations for Hg show better agreement.[10] Inclusion of continuum-state configuration interaction (CSCI) between the various jj channels should also improve the agreement in Cd.

Johnson et al.[38] have calculated the Cd 5s partial cross-section using the relativistic random-phase approximation (RRPA). In order to put our relative cross-sections on an absolute scale we have scaled our total cross-section to the measurements of Cairns et al.[2] over the 20-26 eV range. The RRPA calculation is then a factor of two larger than our measurements between 19.5 and 27 eV. We can account for two of the major deficiencies in the calculation. One is that Johnson et al. overestimate the total Cd cross-section due to the absence of core relaxation in their calculations. To account for this we can compare branching ratios instead of absolute cross-sections. The other problem is that the RRPA calculation neglected the effects of two-electron excitations which are responsible for the appearance of the 5p satel-

lite. To account for this we can compare the RRPA 5s cross-section to the sum of the 5s and 5p cross-sections. In Fig. 5 we compare our ratio of the 5s plus 5p cross-sections to the total cross-section together with the 5s to the total ratio from the RRPA calculations. While the RRPA calculation is still ~10% lower than our points it appears as if we have accounted for most of the major discrepancy.

D. THE 588Å RESONANCE REGION

1. Excitation properties.

The most prominent feature in the absorption spectrum of Cd I between 19 and 30 eV is a very broad asymmetric resonance centered at 588Å. Mansfield[17] has assigned this resonance as:

$$(4d^{10}5s^2)\ {}^1S_0 + h\nu \rightarrow [4d^9(5s5p\ {}^3P)]^2{}_{3/2}6s\ {}^1P_1 \quad , \qquad (1)$$

the first (n=6) member of the $[4d^9(5s5p\ {}^3P)]^2P_{3/2}ns$ series, which has a series limit at 522Å. This series of absorptions, which would involve the simultaneous excitation of one valence (5s) and one subvalence (4d) electron, cannot be explained in a single-particle theory without correlation. Mansfield has attributed these double excitations to excited-state configuration mixing (ESCI) because of the weak or nonappearance of the $4d^9 5s6snp$ series which would have indicated ISCI. ESCI refers to the mixing of various bound-state configurations. This predominance of ESCI is probably caused by larger 5s-6s mixing in the effective po-

tential of the $4d^{-1}5p$ configuration of the excited state than in the effective potential of the closed $4d^{10}$ core of the ground state.

In the ESCI model the states of the Rydberg series $4d^9(5s5p\ ^3P)^2P_{3/2}$ ns,nd (J=1) contain admixtures of other states with the same parity and angular momentum. Let us write for the state excited at 588Å

$$|\phi_{6s}\rangle = a_1|\ [4d^9(5s5p\ ^3P)]^2P_{3/2}6s\ ^1P_1\rangle + a_2\ |(4d^95s^25p)\ ^1P_1\rangle + \ldots \quad , \tag{2}$$

where

$$\sum_i a_i^2 = 1 \quad .$$

The amplitude coefficient a_1 of the basis function nominally characterizing the state is taken to be positive, and a_2 may be one of the smaller mixing coefficients. The "double excitations" from the ground state are primarily due to small admixtures of configurations which are connected to the ground state by strong one-electron dipole transitions. Because of the strong transitions

$$(4d^{10}5s^2)\ ^1S_0 \rightarrow (4d^95s^25p)\ ^{1,3}P_1 \tag{3}$$

at 12.13 and 12.82 eV, the $4d^95s^25p$ configuration is the most likely to appear admixed in Eq. (2). The oscillator strengths for these transitions are $f(^1P_1) = 0.07$ and $f(^3P_1) = 0.53$.[39] Hartree-Fock (HF) calcu-

lations[40] suggest that the state usually called $^3P_1$ at 12.82 eV is actually 85% $^1P_1$ and the state called $^1P_1$ at 12.13 eV is only 14% $^1P_1$.

While the 588Å feature is by no means an isolated resonance, it appears to have an order of magnitude more oscillator strength than nearby resonances, so that it may be considered alone for most of the present analysis.

Very little work has been done on the decay of an autoionizing state into several final ionic states. If the outgoing channels reached through the autoionizing decay can also be reached by direct photoemission, then the two processes can interfere. Fano[18,19] showed that the interference in absorption caused by a discrete state, ϕ, embedded in many continua, denoted by μ, causes an absorption lineshape that has the form:

$$\sigma(\varepsilon) = \sigma_t \left[\rho^2 \frac{(q + \varepsilon)^2}{1 + \varepsilon^2} + 1 - \rho^2 \right] \tag{4}$$

$$\varepsilon = \frac{E - E_0}{\Gamma/2}$$

where q and ρ^2 are constant over the resonance, E_0 is the resonance energy and Γ is the resonance width.

The q parameter, known as the Fano parameter, is given by

$$q = \frac{\langle \phi | \vec{r} | g \rangle}{\pi \sum_{\mu} \langle \phi | V | \mu \rangle \langle \mu | \vec{r} | g \rangle} \tag{5}$$

and ρ, which gives the strength of the interference, is given by

$$\rho = \frac{\sum_{\mu} \langle \phi | V | \mu \rangle \langle \mu | \vec{r} | g \rangle}{\left(\sum_{\mu} \langle \phi | V | \mu \rangle^2 \right)^{1/2} \left(\sum_{\mu} \langle \mu | \vec{r} | g \rangle^2 \right)^{1/2}} \qquad (6)$$

where g represents the ground state, Φ is the discrete state that has been modified by the continuum and V is the coulomb interaction.

The oscillator strength of the 588Å resonance can be obtained by fitting the lineshape in Eq. (4) to the total photoelectron yield from our measurements. The oscillator strength, f, is related to the parameters in Eq. (4) by

$$gf = (0.78) q^2 \rho^2 \sigma_t \Gamma \qquad (7)$$

where g is the statistical weight 2J + 1, σ_t is expressed in Mb, Γ is measured in Rydbergs and f, q and ρ^2 are dimensionless. With q = -0.62, ρ^2 = 0.27 and, Γ = 5.1 x 10^{-3} Ry from the fit to our total photoelectron yield, σ_t = 7.3 Mb and J = 0, we obtain f = 7.8 x 10^{-4}. Using this f-value together with those for Eq. (3) yields a $(4d^9 5s^2 5p)\ ^1P_1$ component a_2^2 = 1 x 10^{-3}. This small degree of configuration mixing shows that the strong appearance of these "double excitation" series is due primarily to the strength of the transitions in Eq. (3) and not to the magnitude of the mixing coefficient.

2. Partial cross-sections.

Starace[20] has addressed the problem of the form of the expression for each of several different outgoing channels in the neighborhood of a resonance. Davis and Feldkamp[21] have derived equivalent expressions using a different approach. We shall use the notation of Starace. His expression for the cross section of the μth observable photoemission channel at energy E is:

$$\sigma(\mu,\varepsilon) = \frac{\sigma_0(\mu)}{1+\varepsilon^2}\left\{\varepsilon^2 + 2\varepsilon[q\mathrm{Re}(\alpha_\mu) - \mathrm{Im}(\alpha_\mu)] + 1 - 2q\mathrm{Im}(\alpha_\mu)\right.$$

$$\left.-2\mathrm{Re}(\alpha_\mu) + (q^2+1)|\alpha_\mu|^2\right\} \qquad (8)$$

where $\sigma_0(\mu)$ is the off-resonance partial cross-section for the μth asymptotically observable final state of the ion-electron system, ε and q are the parameters that are used to characterize the total absorption in Eq. (4), and the complex parameter α_μ is taken as constant over the resonance. The α_μ parameters are given by[41]

$$\alpha_\mu = \frac{\langle \phi|V|\mu\rangle}{\langle g|\vec{r}|\mu\rangle}\left[\frac{2\pi}{\Gamma}\sum_\mu \langle g|\vec{r}|\mu\rangle\langle\mu|V|\phi\rangle\right] \quad . \qquad (9)$$

The summation extends over all observable photoelectron channels μ, so that the term in square brackets is common to all channels.

Figures 6 and 7 show the partial cross-sections obtained in the resonance region for each of the observed photoelectron peaks. The solid curves in Figs. 6 and 7 represent least-squares fits to the function

$$\sigma(\epsilon) = \sigma_0(\epsilon)\left(\frac{C_1 + C_2\,\epsilon + \epsilon^2}{1 + \epsilon^2}\right) \qquad (10)$$

convoluted with a function describing the monochromator bandpass (a truncated triangular function with 2.5Å FWHM). Here $\sigma_0(\epsilon)$ is a slowly varying nonresonant partial cross-section (we used a power series in ϵ to order ϵ^2) and ϵ is the reduced energy variable of Eq. (4). The resonance width $\Gamma = 0.07$ eV and position $E_0 = 21.10$ eV were held fixed to be consistent for the entire set of profiles. The resonance position is in good agreement with the 21.09 eV (588Å) value obtained in absorption.[17] The 2.5Å (= 0.09 eV at 21.1 eV) monochromator bandpass is slightly larger than the linewidth (Γ = FWHM = 0.07 eV), making an accurate determination of Γ difficult.

The energy dependence of $\sigma(\epsilon)$ in Eq. (10) is identical to that in Eqs. (4) and (8). However, Eq. (4) represents the total absorption profile and does not apply to a partial cross-section.* This similarity has led some experimenters to fit partial cross-section data to Eq. (4) and thus extract an effective q and ρ^2. It should be noted that the treatments of Refs. 19–21 do not provide a simple theoretical expression for a q or ρ^2 for each photoionization channel. The fitting parameters are given in Table II. The C_1 and C_2 parameters for the total absorption cross-section correspond to $q = -0.62$ and $\rho^2 = 0.27$ as given above.[42]

The $4d_{5/2}$ and $4d_{3/2}$ partial cross-sections have similar profiles, with the $4d_{3/2}$ showing more interference. The total cross-section, which receives over 90% of its intensity from the 4d channels, has a shape similar to the 4d partial cross-sections. The resonance profile of the 5s channel is opposite that of the absorption: i.e., the 5s minimum is on the low energy side of the maximum while the absorption minimum is on the high energy side of the maximum. The 5s intensity shows a larger fractional rise (= 1.2) than do the 4d's. The unresolved 5p's have a nearly Lorentzian profile, with a fractional increase of 1.9. The 5p profile is slightly higher on the low energy side but a symmetric Lorentzian will fit it within experimental error.

What does it mean physically for the 5s and 4d resonances to have opposite phases? From Eqs. (8) and (9) we see that the resonance lineshape for each channel is determined by the α_μ parameter for that channel. The α_μ parameter is in turn a function of the amplitude matrix elements describing the resonant (autoionization) and nonresonant (photoemission) paths from the ground state to the particular ionic state in question. These matrix elements can, of course, have a wide range of values, depending on the electronic structure of the particular states under study. Of the four parameters E_0, Γ, ρ^2 and q that describe the absorption process, only E_0 and Γ carry over to each photoemission resonance. The ρ^2 and q parameters, if they are regarded as channel-sensitive quantities, are replaced for <u>each</u> photoemission resonance by a set of α_μ parameters in addition to the absorption-q; i.e., two numbers for each channel μ in addition to the integral q value derived from the absorption profile.

Now it is clear why Eqs. (8) and (10) cannot be combined to solve for $Re(\alpha_\mu)$ and $Im(\alpha_\mu)$. The problem is that several outgoing channels μ (where μ specifies the fine-structure level of the core, the orbital and total angular momenta of the continuum electron and the coupling of the core and continuum electron) are present and unresolved in a photoemission intensity measurement, which only selects the final kinetic energy of the outgoing electron. For example the $4d_{5/2}$ photoelectron peak contains three outgoing channels:

$$\begin{aligned}(4d^{10}5s^2)\ {}^1S_0 + h\nu &\rightarrow (4d^9 5s^2)\ {}^2D_{5/2} + \epsilon p_{3/2} \\ &\rightarrow (4d^9 5s^2)\ {}^2D_{5/2} + \epsilon f_{5/2} \\ &\rightarrow (4d^9 5s^2)\ {}^2D_{5/2} + \epsilon f_{7/2}.\end{aligned} \tag{11}$$

Each observable cross section $\sigma(j,\epsilon)$ for a particular photoelectron peak j will then be the sum of several $\sigma(\mu,\epsilon)$ in Eq. (8). The result is a form similar to Eq. (8), in which the $\sigma_0(\mu)$ has been replaced by $\sigma_0(j)$, the total off-resonance partial cross-section of the unresolved channels, and $Re(\alpha_\mu)$, $Im(\alpha_\mu)$, and $|\alpha_\mu|^2$ have been replaced by $Re\langle\alpha\rangle_j$, $Im\langle\alpha\rangle_j$, and $\langle|\alpha|^2\rangle_j$, which are averaged quantities that have been weighted by the $\sigma_0(\mu)$. Using the Schwartz inequality we know that

$$(Re\langle\alpha\rangle_j)^2 + (Im\langle\alpha\rangle_j)^2 \leq \langle|\alpha|^2\rangle_j \tag{12}$$

so that the modified Eq. (8) is therefore dependent upon three unknown quantities $Re\langle\alpha\rangle_j$, $Im\langle\alpha\rangle_j$, and $\langle|\alpha|^2\rangle_j$. Because the fitting of experimental data to Eq. (10) yields only two parameters, it is impossible to solve for these three unknown quantities.

While it is not feasible in general to draw specific qualitative conclusions from the photoemission intensity resonance profiles above, there are exceptions. For example, the 5p partial cross-section is nearly Lorentzian which would imply little interference between the resonant and nonresonant processes that contribute to its intensity. This point will be discussed further in Section V. In the case of a Lorentzian lineshape the height is given by

$$\sigma(5p,\varepsilon=0) = \rho^2\sigma_t \frac{5p}{\Gamma}(q^2+1) \qquad (13)$$

which is obtained from Eq. (8) in the limit of $\sigma_0(5p) \to 0$. The same result has been obtained independently by Wendin[43] for a two-channel case. This yields the partial decay width Γ_{5p} in the case of no interaction between the autoionizing and direct photoemission processes of the 5p channels (see Table III).

For the 5s final ionic state there are only two outgoing channels: the $\varepsilon p_{1/2}$ and $\varepsilon p_{3/2}$ waves. The dipole and Coulomb matrix elements for these two channels determine two of the α_μ parameters: $\alpha_{5s\varepsilon p_{1/2}}$ and $\alpha_{5s\varepsilon p_{3/2}}$. When the spin-orbit interaction in the εp continuum is small, which is likely because of the diffuse nature of the continuum waves, and the ^1P resonance state shows no singlet-triplet mixing,[17] then the partial decay widths of the two channels become equal and the phase difference between the two dipole matrix elements becomes negligible. Under these assumptions Eq. (12) becomes

$$(\mathrm{Re}\langle a\rangle_{5s})^2 + (\mathrm{Im}\langle a\rangle_{5s})^2 = \gamma^{-1}\langle |a|^2\rangle_{5s} \qquad (14)$$

where γ depends only on the real ratio of the two dipole matrix elements. To determine γ we use the off-resonance value of the angular-distribution asymmetry parameter, β, for the 5s photoelectrons[5] which we have measured to be 1.85 ± 0.1. It should be mentioned that because the two dipole matrix elements are not equal off resonance, we would expect β_{5s} to change over the resonance even though the resonance state is LS coupled. Our measurements of β_{5s} near the resonance show a scatter down to $\beta = 1.4$ that cannot be interpreted in terms of a single resonance. A value of β equal to ~1.85 agrees with calculations[38] that show a Cooper minimum below threshold and leads to a value of γ equal to ~1.06. Equations (8), (10) and (14) and the fitting parameters in Table II may then be used to obtain $\mathrm{Re}\langle\alpha\rangle_{5s}$, $\mathrm{Im}\langle\alpha\rangle_{5s}$ and $\langle|\alpha|^2\rangle_{5s}$. To do so, it is necessary to solve a rather complicated quadratic equation for $\mathrm{Re}\langle\alpha\rangle_{5s}$ and pick one of the two solutions. We reject the solution corresponding to $\langle|\alpha|^2\rangle_{5s} > 1$ as implausible, because it would imply that the 5s channels receive a 13 times larger fraction of the resonance decay than of the direct photoionization. The parameters for the plausible solution are given in Table III.

This analysis of the s channel is considerably more complicated when the resonance state has intermediate coupling and lies near a Cooper minimum as does the strong $(4d^9 5s^2 5p)\ ^1P_1$ resonance at 12.13 eV. In this case a strong variation of β_{5s} over the resonance is to be expected and additional measurements of the spin polarization are necessary to obtain the internal distribution of the $\varepsilon p_{1/2}$ and $\varepsilon p_{3/2}$ continuum waves. The spin polarization which was recently measured by Schäfers et al.[44] shows that the spin-orbit interaction near this reso-

nance is strongly influenced and enhanced by the coupling between the discrete resonance and the continuum states.

Information about the α parameters for the 4d channels can also be obtained. Using the definitions of α_μ in Eq. (9) and ρ in Eq. (6) we find

$$\langle|\alpha|^2\rangle_j \frac{\sigma_0(j)}{\sigma_t} = \rho^2 \frac{\Gamma_j}{} \tag{15}$$

where Γ_j is the partial width and $\sigma_0(j)$ is the partial cross-section for any set of channels. Using a sum rule for the Γ_j

$$\sum_j \Gamma_j = \Gamma \tag{16}$$

we can also obtain

$$\sum_j \frac{\sigma_0(j)}{\sigma_t} \langle|\alpha|^2\rangle_j = \rho^2 \quad . \tag{17}$$

Since we have already found Γ_{5p} and $\langle|\alpha|^2\rangle_{5s}$ we can solve Eqs. (15) and (17) for $\langle|\alpha|^2\rangle_{4d}$, which is a weighted average of the $4d_{5/2}$ and $4d_{3/2}$ groups of channels. This done, we can use the line profile fitting parameters C_1 and C_2 for the 4d channels to solve for $\mathrm{Re}\langle\alpha\rangle_{4d}$ and $\mathrm{Im}\langle\alpha\rangle_{4d}$. These results are also listed in Table III. A check of the results in Table III can be made using the following relations:

$$\sum_j \sigma_0(j)\, \mathrm{Re}\langle\alpha\rangle_j = \rho^2 \sigma_t$$

and (Eq. 18)

$$\sum_j \sigma_0(j)\, \mathrm{Im}\langle\alpha\rangle_j = 0$$

which can be derived in an analogous manner to Eqs. (41) and (42) in Ref. 20. The results in Tables II and III are in good agreement with Eq. (18).

A description of the partial cross-section results in terms of the derived α parameters proceeds as follows. The values of $\langle|\alpha|^2\rangle_j$ for the 4d, 5s and 5p electrons show that the partial decay widths are divided among the three channels in accordance with their partial cross-sections, with the 5p channel having twice its share. The real and imaginary parts of $\langle\alpha\rangle_{5s}$ and $\langle\alpha\rangle_{4d}$ show the distinct phase shift between the Coulomb interaction integrals of the 4d and 5s channels, which is also apparent in the profiles of the partial cross-sections.

3. Fano q parameter.

All of the asymmetric absorptions detected in the 20-24 eV energy region displayed negative q values. Mansfield showed that the $4d^{10}5p$ ns,nd series as well as the $[4d^9(5s5p\ ^3P)]\ ^2P_{3/2}$ ns series probably derive their oscillator strength from interactions with the $(4d^95s^25p)\ ^{1,3}P_1$ states. By elucidating the factors that cause the 588Å resonance to have a negative q, we may learn something about the other resonances as well.

The sign of the q parameter depends on the signs of the matrix elements in Eq. (5). First we consider the transition matrix element $\langle\phi|\vec{r}|g\rangle$ of the direct absorption which for the 588Å transition is given by Eq. (2) as

$\langle \phi_{6s} | \vec{r} | (4d^{10}5s^2)\ ^1S_0 \rangle \equiv$

$$a_2 \langle (4d^9 5s^2 5p)\ ^1P_1 | \vec{r} | (4d^{10}5s^2)\ ^1S_0 \rangle \quad . \qquad (19)$$

The HF radial integral[40] $\int_0^\infty R_{4d} R_{5p}\, r dr$ together with the corresponding angular part shows that the $\langle (4d^9 5s^2 5p)\ ^1P_1 | \vec{r} | (4d^{10}5s^2)\ ^1S_0 \rangle$ matrix element is positive.

To calculate the matrix elements in the denominator of Eq. (5) we make use of Eq. (6) and published calculations of the $4d \rightarrow \varepsilon p, \varepsilon f$ cross sections and radial integrals. The denominator of Eq. (5) represents the indirect photoabsorption amplitude in which an electron is photoexcited to the continuum and then scattered into the resonance state. The calculations for Cd,[1] Sn,[45] and Xe[46] show roughly equal cross sections for the $4d \rightarrow \varepsilon p$ and $4d \rightarrow \varepsilon f$ channel in the low energy region. Because only the calculations on Sn gave radial integrals rather than just cross sections, we have adjusted the Sn results to our experimental 4d cross section. These scaled integrals and the values in Tables II and III were then used to solve Eq. (6) in a nonrelativistic framework for the partial decay widths into the $4d^9 5s^2 \varepsilon p$ and $4d^9 5s^2 \varepsilon f$ channels. Because of the quadratic character of Eq. (6), there are two solutions, one with the p-wave as the dominant decay channel and one with the f-wave dominant. Without configuration mixing in the excited state there would be a vanishing $\Gamma_{\varepsilon f}$ due to angular momentum conservation. We have thus chosen the solution with the p-wave fraction greater than the f-wave which gives $\Gamma_{\varepsilon p}/\Gamma_{\varepsilon f} > 9$ regardless of the sign of the $4d^{10}5s\varepsilon p$ channel contribution. Thus the denominator of Eq. (5) is pos-

itive, which leads to the final conclusion that the negative sign of the q-parameter is due to the negative sign of the mixing coefficient a_2. The sign of a_2 is relative to certain wave function sign conventions. Since the considerations leading to the positive denominator above would be generally applicable to all of the Cd I resonances in this region, we may expect that the corresponding mixing coefficients of the $(4d^9 5s^2 5p)\ ^1P_1$ state for all of these resonances are negative. We note that, given certain assumptions, an analysis of this kind can yield the sign of the amplitude coefficient when interference with the continuum is present. Without interference the sign would be inaccessible.

4. Resonance effects on the angular distribution and branching ratio.

Other parameters sensitive to the effects of the 588Å resonance are the Cd 4d branching ratio (Fig. 8) and the angular distributions of the 4d electrons, expressed as the asymmetry parameters (Fig. 9). Starace[20] has discussed the problem of the branching ratio of a spin-orbit split pair in the neighborhood of a resonance for the case in which no additional final ionic states are accessible. His specialized branching ratio formulae are therefore not applicable to the problem at hand. The shape of the 4d branching ratio is caused by the $4d_{3/2}$ having larger percentage variations due to interference than the $4d_{5/2}$. This is supported by our expectation that the p-wave is the dominant decay channel from the autoionizing state and that the $4d_{3/2}$ has more p-wave contributions than the $4d_{5/2}$ from direct ionization.

Kabachnik and Sazhina[22] have derived a general expression for angular distribution profiles near autoionizing resonances. Angular distributions have different dependences than partial cross-sections on the matrix elements that characterize the excitation and decay of the autoionizing state. Kabachnik and Sazhina's expression can be cast in the form

$$\beta(j,\varepsilon) = \beta_0(j) \frac{A_1(j) + A_2(j)\varepsilon + \varepsilon^2}{\rho^2(q^2-1) + 1 + 2\rho^2 q\,\varepsilon + \varepsilon^2} \qquad (20)$$

where ε, q and ρ^2 are the same as in Eq. (4), $\beta_0(j)$ is the off-resonant asymmetry parameter and $A_1(j)$ and $A_2(j)$ are constants.

Our angular distribution data for the 4d electrons (Fig. 9) are not adequate to provide very accurate lineshape parameters. In Fig. 9 we have plotted curves of the form of Eq. (20) convoluted with the monochromator bandpass and with E_0, Γ, q and ρ^2 taken from the total cross-section fit. The resonances in Fig. 9 appear asymmetric with increases in β of over 0.5 unit, which would become 1.0 unit in the absence of monochromator broadening. It can be seen that measurements made at the 21.21 eV He I resonance energy are affected by the resonance.

E. CORRELATION SATELLITES

Through detailed studies of the energy dependences of correlation satellites it is possible to distinguish between the largely energy-independent interactions (i.e., ISCI and final-ionic-state configuration interaction, FISCI) and the energy-dependent configuration mixings

in the final state which include the outgoing photoelectron. Such investigations have been performed only for the rare gases.[47] Correlation satellites from the photoionization of Cd have been observed previously.[14-16] This earlier work was restricted to the $(4d^{10}5p)\ ^2P_{3/2,1/2}$ satellites, which were the only ones detected at He I (21.21 eV) and He II (40.8 eV) resonance-lamp energies. The total 5p intensity, relative to the 5s main line, was found to be 15% by Süzer et al.[14] and 10% by Hush et al.[15] at 21.21 eV. At 40.8 eV[15] the $5p_{1/2}$ peak was obscured by an inelastic loss line, but the $5p_{3/2}$ to 5s ratio appeared to be the same as at 21.21 eV. By comparisons with Zn and Hg, it was concluded that most of the 5p satellite intensity arose from ISCI.[14] FISCI is not expected to contribute to the p satellite intensities of group IIA and IIB elements, for which the final ionic state is a single electron outside a closed shell.

Hansen[16] calculated MCHF expansion coefficients for Zn, Cd and Hg which give 5p satellite intensities that are too small by factors of 2.5 to 5.0. Suzer et al. pointed out that the MCHF expansion coefficient ratios would have to be multiplied by the cross-section ratios for the different configurations, to yield relative intensities. This correction has never been made.

Our measurements of the 5p:5s ratio, shown in Fig. 10, has a slightly downward-sloping "baseline" value which is ~0.22 at 21 eV. The 588Å resonance and two resonances at 22.83 and 22.91 eV perturb this smooth background. (This figure also illustrates the difficulty of obtaining a baseline when autoionization is present!)

Let us address the question of how large the effect of the 588Å resonance will be on measurements made with a He I resonance lamp. Using the fits in Figs. 5 and 6 and Table II we calculate that the term in parentheses in Eq. (10) modifies the direct photoemission intensity ($\sigma_0(\varepsilon)$ in Eq. 10) by factors of: 1.42 (5s), 1.02 (5p), 0.88 ($4d_{5/2}$), and 0.83 ($4d_{3/2}$). This would cause the 5p:5s ratio measured with He I resonance light to be 28 percent lower than the desired "off-resonance" value. The 5p:5s ratio of 0.15 of Süzer et al. is then in good agreement with the 0.22 value obtained in this work.[48]

The 5p:5s ratio shows a peaked resonance profile, with an enhancement factor of 2, about the 588Å resonance, as discussed in the previous section. Decay of the $[4d^9(5s5p\ ^3P)]^2P_{3/2}6s\ ^1P_1$ main component into the $4d^{10}5p\varepsilon\ell$ continuum via autoionization leads only to an outgoing εd wave, by angular momentum conservation. The nearly Lorentzian profile of the 5p partial cross-section signifies only weak interference between the resonant and nonresonant processes that produce the 5p satellite. This implies resonance enhancement by autoionization superimposed on a mostly ISCI-generated background. The absorption spectrum shows that the Rydberg series converging on the $4d^{10}5p$ limit probably derive their strength from interactions with the $(4d^{10}5s^2)\ ^1S_0 \rightarrow (4d^95s^25p)\ ^{1,3}P_1$ resonance.[17] Because this bound-state mixing (ESCI) should persist beyond the 5p threshold it is likely that part of the 5p satellite intensity originates from this interaction. To gauge the magnitude of this interchannel coupling we have plotted three curves in Fig. 10, each representing a different fraction of ISCI. The ISCI fraction is taken as being an energy-independent contribution to the 5p:5s

branching ratio. Interchannel coupling with the bound $(4d^9 5s^2 5p)\ ^{1,3}P_1$ states at 12.8 eV is assumed to fall off as $1/E^2$. The data suggest that the ISCI contribution to the branching ratio is around 0.15, which would correspond to a $(4d^9 5s^2 5p)\ ^{1,3}P_1$ admixture coefficient at 21 eV of less than 10^{-3}. Lower-energy measurements will be required to ascertain better the magnitude of the interchannel coupling contribution.

Two points were taken at 22.83 and 22.91 eV, to coincide almost precisely with two of the strongest resonances seen by Mansfield at 22.83 and 22.92 eV. Mansfield tentatively assigned these features as:

$$\underline{22.83\ eV}\ [4d^9(5s5p\ ^3P)]^2P_{3/2}6d$$

and

$$\underline{22.92\ eV}\ [4d^9(5s5p\ ^3P)]^4D_{1/2}6d.$$

The 5p:5s ratio is found to increase at these resonant energies.

The branching ratio of the 5p spin-orbit split satellite lines is shown in Fig. 11. The solid curve was obtained by self-consistently fitting the $5p_{3/2}$ (a) and $5p_{1/2}$ (b) cross-sections to Eq. (10) convoluted with the monochromator bandpass, the total 5p cross-section to a symmetric Lorentzian equal to a+b, and the 5p branching ratio to a/b. The resulting curve is given by:

$$R(5p) = 1.45\left(\frac{3.24 + 0.33\epsilon + \epsilon^2}{2.78 - 0.48\epsilon + \epsilon^2}\right) .$$

The point at 20.81 eV is probably low due to a sharp resonance at 20.83 eV. If the (unresolved) 5p partial cross-section is a symmetric Lorentzian, then the $5p_{3/2}$ partial cross-section has a larger high-energy tail and the $5p_{1/2}$ partial cross-section has a larger low-energy tail. Previous measurements of p branching ratios at the He I energy[14,15] showed a nonmonotonic decrease from Zn to Cd to Hg due to the close proximity of the 588Å resonance in Cd. Our off-resonance value of 1.45 ± .10 and the ~2.0 and 0.3 values obtained for Zn and Hg, respectively, clearly show the trend of increasing $(p_{1/2})^2$ mixing with the $(ns)^2$ primary configuration as spin-orbit coupling increases.[49]

Three other satellite lines were seen for the first time in our spectra. They correspond to the 6s, 5d, and 6p ionic states listed in Table I. By comparison with the higher binding-energy satellites found in the group IIA elements, we would expect ISCI to produce these satellites with no more than 2% of the intensity of the 5s main line. As can be seen in Table IV, the intensities detected in our experiment were far greater than this.

The highest binding-energy (6p) satellite was detected only at the 22.83 and 22.92 eV resonances, while the 6s satellite was seen at two additional wavelengths. At the 22.92 eV resonance the 6s satellite had an intensity equal to 90% of the 5s main line, as shown in Fig. 2. Since the 22.92 eV resonance width (<1Å) is considerably less than our monochromator bandpass, the 6s satellite is probably many

times larger than the 5s main line at 22.92 eV. The 5d satellite did not show enhancement due to autoionization at only a few selected resonances; rather it was enhanced in every spectrum that was recorded between 22 and 24 eV. Since the 5d satellite has a binding energy of 20.1 eV, its absence below 22 eV photon energy may be only a result of our lower sensitivity to low kinetic-energy electrons. The same may be true of the 6s satellite below 22 eV.

Production of the 6s and 5d satellites by the autoionizing states between 22 and 24 eV can probably be explained by ESCI and Auger decay. The resonant states contain admixtures of several configurations having the form

$$(4d^9 5s5p6s)\ {}^1P_1$$

and

$$(4d^9 5s5p5d)\ {}^1P_1$$

with various forms of internal coupling.[17] These admixtures can Auger decay to the 5d and 6s satellites.

F. CONCLUSIONS

The following conclusions were drawn from this investigation of photoemission from cadmium vapor in the $h\nu$ = 19 - 27 eV range:

1. The 4d peaks show resonant behavior in both $\beta(\epsilon)$ and the branching ratio near 588Å. Deviations of the off resonance branching ratio from Dirac-Fock calculations were observed, indicating the need for a more exact treatment of this intermediate-Z atom.

2. The 5s cross-section is lower by about a factor of two than predictions based on RRPA theory. It was shown how most of this difference could be attributed to approximations made in the RRPA calculation.

3. Photoelectron cross-sections showed pronounced, and very different, resonance profiles at the 588Å resonance for the 4d, 5s, and 5p lines. Thus photoemission resonances contain more information, and require a more detailed theory, than absorption resonances.

4. Parameters were derived from the cross-section data for the 4d, 5s, and 5p lines at the 588Å resonance, using a theoretical formalism given by Starace and by Davis and Feldkamp, together with a plausible set of assumptions.

5. The resonance behavior of $\beta(\epsilon)$ for the 4d peaks could be fitted by an expression of the form given by Kabachnik and Sazhina, using parameters derived from the cross-section data and additional amplitude parameters.

6. The energy dependence of the 5p correlation satellite was studied. Analysis showed that this satellite arises mostly from initial-state configuration interaction (ISCI).

7. The 5p peak intensity was greatly enhanced at the 22.83 eV and 22.92 eV resonances.

8. The $5p_{3/2}$ and $5p_{1/2}$ satellites were analyzed separately, and an earlier discrepancy in the systematics of np satellites in group IIB elements was resolved.

9. Three new satellites - 6s, 5d, and 6p - were observed for the first time, with high intensities probably caused by autoionization.

In summary, this study has further demonstrated the feasibility and value of variable-energy photoemission measurements on metal vapors. By observing several new phenomena in photoemission from Cd, we have shown that correlation effects can be elucidated in several ways in this type of experiment.

REFERENCES

*Paper published with co-authors U. Becker, S. Southworth, C.M. Truesdale, D.W. Lindle, and D.A. Shirley, Phys. Rev. A 26, 842 (1982).

1. S. L. Carter and H. P. Kelley, J. Phys. B 11, 2467 (1978).
2. R. B. Cairns, H. Harrison and R. I. Schoen, J. Chem. Phys. 51, 5440 (1969).
3. K. Codling, J. R. Hamley and J. B. West, J. Phys. B. 11, 1713 (1978).
4. H. Harrison, J. Chem. Phys. 52, 901 (1970).
5. T. E. H. Walker and J. T. Waber, J. Phys. B 7, 674 (1974).
6. C. E. Theodosiou, J. Phys. B 12, L673 (1979).
7. C. E. Theodosiou, A. F. Starace, B. R. Tambe and S. T. Manson, Phys. Rev. A 24, 301 (1981).
8. G. Schönhense, J. Phys. B 14, L187 (1981).
9. S. P. Shannon and K. Codling, J. Phys. B 11, 1193 (1978).
10. B. R. Tambe, W. Ong and S. T. Manson, Phys. Rev. A 23, 799 (1981).
11. C. D. Caldwell and R. N. Zare, Phys. Rev. A 16, 255 (1977).
12. W. Mauser and W. Melhorn, Extended Abstr. VI Int. Conf. on VUV Radiation Physics, Charlottesville, Virginia 1980 (unpublished), II-7.
13. E. G. Berezhko, N. M. Kabachnik and V. S. Rostovsky, J. Phys. B 11, 1749 (1978).
14. S. Süzer, S. T. Lee and D. A. Shirley, Phys. Rev. A 13, 1842 (1976).
15. N. S. Hush and S. Süzer, Chem. Phys. Lett. 46, 411 (1977).

16. J. E. Hansen, Phys. Rev. A 15, 810 (1977).

17. M. W. D. Mansfield, Proc. R. Soc. London, Ser. A 362, 129 (1978).

18. U. Fano, Phys. Rev. 124, 1866 (1961).

19. U. Fano and J. W. Cooper, Phys. Rev. 137, A1364 (1965).

20. A. F. Starace, Phys. Rev. A 16, 231 (1977).

21. L. C. Davis and L. A. Feldkamp, Phys. Rev. B 23, 6239 (1981).

22. N. M. Kabachnik and I. P. Sazhina, J. Phys. B 9, 1681 (1976).

23. W. R. Johnson, K. T. Cheng, K. N. Huang and M. LeDourneuf, Phys. Rev. A 22, 989 (1980) and B. Brehm and K. Hofler, Phys. Lett. 68A, 437 (1978).

24. J. Codling, J. B. West, A. C. Parr, J. L. Dehmer and R. Stockbauer, J. Phys. B 13, L693 (1980).

25. J. H. D. Eland, Mol. Phys. 40, 917 (1980).

26. J. B. West, K. Codling, A. C. Parr, D. L. Ederer, B. E. Cole, R. Stockbauer and J. L. Dehmer, J. Phys. B 14, 1791 (1981) and A. C. Parr, D. L. Ederer, B. E. Cole, J. B. West, R. Stockbauer, K. Codling and J. L. Dehmer, Phys. Rev. Lett. 46, 22 (1981).

27. B. Brehm and A. Bucher, Int. J. Mass Spectrom. Ion Phys. 15, 463 (1974).

28. B. Brehm and K. Hofler, Int. J. Mass Spectrom. Ion Phys. 17, 371 (1975).

29. S. -T. Lee, S. Süzer, E. Matthias, R. A. Rosenberg and D. A. Shirley, J. Chem. Phys. 66, 2496 (1977).

30. R. A. Rosenberg, M. G. White, G. Thornton and D. A. Shirley, Phys. Rev. Lett. 43, 1384 (1979).

31. D. Chandesris, C. Guillot, G. Chauvin, J. LeCante and Y. Petroff, Phys. Rev. Lett. 47, 1273 (1981).

32. M. G. White, R. A. Rosenberg, G. Gabor, E. D. Poliakoff, G. Thornton, S. H. Southworth and D. A. Shirley, Rev. Sci. Instrum. 50, 1286 (1979).

33. S. Southworth, C. M. Truesdale, P. H. Kobrin, D. W. Lindle, W. D. Brewer and D. A. Shirley, J. Chem. Phys. 76, 143 (1982).

34. Semco Inc., North Hollywood, California. Two conductor Nichrome V wires insulated by MgO inside an Inconel 600 sheath.

35. C. E. Moore, Atomic Energy Levels, Vol. 3. NBS Circular 467.

36. S. Süzer, P. R. Hilton, H. S. Hugh and S. Nordholm, J. Electron Spectrosc. Relat. Phenom. 12, 357 (1977).

37. J. L. Dehmer and J. Berkowitz, Phys. Rev. A 10, 484 (1974).

38. W. R. Johnson, V. Radojević, P. Deshmukh and K. T. Cheng, to be published, Phys. Rev. A 25, 337 (1982).

39. G. V. Marr and J. M. Austin, Proc. Roy. Soc. London, Ser. A 310, 137 (1969).

40. M. Wilson, J. Phys. B 1, 736 (1968).

41. P. C. Kemeny, J. A. R. Samson and A. F. Starace, J. Phys. B 10, L201 (1977).

42. The q values in Ref. 17 are all of the wrong sign.

43. G. Wendin, Proceedings of the Daresbury One-Day Meeting, Daresbury Laboratory, Feb. 1978, Ed. B. D. Buckley.

44. F. Schafers, G. Schönhense, and U. Heinzmann, Z. Phys. A 304, 41 (1982).

45. A. Ron, Y. S. Kim and R. H. Pratt, Phys. Rev. A 24, 1260 (1981).

46. S. T. Manson, private communication.

47. See M. Y. Adam, F. Wuilleumier, S. Krummacher, V. Schmidt and W. Mehlhorn, J. Phys. B 11, L413 (1978) and references therein.

48. The peak areas in Refs. 14 and 15 do not represent angle integrated partial cross sections since the electrons were sampled 90° from the propagation axis of the unpolarized light. This would most likely give a ratio lower than the desired angle integrated one.

49. The Hg p branching ratio may also be perturbed by a resonance. See M. W. D. Mansfield, Astrophys. J. 180, 1011 (1973).

Table I. Cd^+ Photoelectron Peaks

Ionic State	Abbreviation	Binding energy (eV)[a]
$4d^{10}5s\ ^2S_{1/2}$	5s	8.99
$4d^{10}5p\ ^2P_{1/2}$	$5p_{1/2}$	14.46
$4d^{10}5p\ ^2P_{3/2}$	$5p_{3/2}$	14.77
$4d^9 5s^2\ ^2D_{5/2}$	$4d_{5/2}$	17.59
$4d^9 5s^2\ ^2D_{3/2}$	$4d_{3/2}$	18.28
$4d^{10}6s\ ^2S_{1/2}$	6s	19.28
$4d^{10}5d\ ^2D_{5/2,3/2}$	5d	20.12
$4d^{10}6p\ ^2P_{3/2,1/2}$	6p	20.77

[a]From Ref. 35.

Table II. Fitting parameters for the partial and total cross-sections. See Eq. (4) for the defining equation.

Ionic State	C_1	C_2	$\sigma_0(\epsilon = 0)$ (Mb)[a,b]
$4d^{10}5s\ ^2S_{1/2}$	1.81 (.10)	1.31 (.10)	0.378
$4d^{10}5p\ ^2P_{3/2,1/2}$	2.89 (.30)	-0.46 (.26)	0.084
$4d^{9}5s^2\ ^2D_{5/2}$	0.76 (.03)	-0.35 (.04)	4.36
$4d^{9}5s^2\ ^2D_{3/2}$	0.76 (.04)	-0.56 (.05)	2.51
Total	0.83 (.04)	-0.34 (.05)	7.34

[a]Uncertainty ≤ 1 in last significant figure.

[b]Slope and curvature of $\sigma_0(\epsilon)$ not given.

Table III. Partial decay widths and α parameters.

Ionic State	(Γ_j/Γ)x100	$\langle \mid \alpha \mid^2 \rangle$	Re$\langle\alpha\rangle$	Im$\langle\alpha\rangle$
$4d^{10}5p\ ^2P_{3/2,1/2}$	5.8	1.38		
$4d^{10}5s\ ^2S_{1/2}$ [a]	6.6	0.35	-0.41	-0.40
$4d^9 5s^2\ ^2D_{5/2,3/2}$	87	0.25	0.31	0.02

[a]The γ in Eq. 14 was inverted and the 5s parameters in Table III were slightly different in the published version of this chapter.

Table IV. Satellite intensities relative to the 5s main line (= 100)[a]

Photon energy (ev)	6s	5d	6p
21.91	0 (10)	27 (4)	0 (10)
22.41	30 (5)	19 (4)	0 (8)
22.83	40 (3)	7 (2)	6 (2)
22.91	88 (5)	20 (3)	19 (3)
23.00	20 (2)	7 (2)	0 (8)
23.41	0 (10)	31 (3)	0 (7)
23.91	0 (10)	12 (2)	0 (6)

[a]Where intensity equals 0 the value in parenthesis represents an upper limit.

FIGURE CAPTIONS

Figure 1. Metal vapor oven. 1. Stainless-steel sample cup. 2. Rigid stainless-steel outer structure. 3. Heating cables. 4. Alumina heat shields. 5. Stainless-steel foil heat shields. The inner diameter of the sample cup is 10 mm.

Figure 2. TOF photoelectron spectrum of Cd^+ taken with the "magic-angle" detector. The accumulation time was 1000 sec. The photoelectron peaks are listed in Table I.

Figure 3. The Cd 4d photoelectron asymmetries. The present $4d_{5/2}$ and $4d_{3/2}$ measurements are shown in panels (a) and (b) respectively. The identical solid curves in (a) and (b) are for visual comparison only. In (c) the filled and open circles represent our $4d_{5/2}$ and $4d_{3/2}$ measurements. The filled and open triangles represent the $4d_{5/2}$ and $4d_{3/2}$ measurements of Schönhense, Ref. 8. The theoretical calculations are from: MBPT, Ref. 1; DS, Ref. 5; DF, Ref. 7; and x's, GIPM, Ref. 36.

Figure 4. The 4d branching ratio. The filled circles represent our results; the open triangles, the measurements of Shannon and Codling Ref. 9; the open square, the measurement of Süzer et al. Ref. 14; the measurement of Dehmer and Berkowitz Ref. 37 of 1.75 at 21.11 eV is not shown. The DS and DF curves represent the Dirac-Slater and Dirac-Fock calculations of Tambe et al. Ref. 10.

Figure 5. The fraction of the total cross-section in the combined 5s and 5p peaks. The curve from Johnson et al. Ref. 38 shows the RRPA calculation of the fraction of the total cross-section in the 5s state.

Figure 6. Partial cross-section measurements of the $4d_{5/2}$ (filled circles), and $4d_{3/2}$ (open circles) photoelectrons. The solid curves are least squares fits to Eq. (10) convoluted with the monochromator bandpass. Fitting parameters are given in Table II. Dashed curves show fits with monochromator broadening deleted.

Figure 7. Same as Fig. 6, for 5s and (unresolved) 5p photoelectrons.

Figure 8. The 4d branching ratio measurements near the 588Å resonance. The solid and dashed curves are ratios of the solid and dashed curves in Fig. 6.

Figure 9. Asymmetry parameter measurements of the (a) $4d_{5/2}$ and (b) $4d_{3/2}$ photoelectrons near the 588Å resonance. The solid curves are visual fits to Eq. (20) convoluted with the monochromator bandpass.

Figure 10. The 5p:5s branching ratio. The curves near the resonance region are represented by the parameters in Table II. The contribution from ISCI in the dotted curve is 0.22, the solid curve 0.15 and the dashed curve 0.06. The remaining contribution is from interchannel coupling as discussed in the text.

Figure 11. The 5p branching ratio measurements near the 588Å resonance. The open square represents the measurements of Süzer et al. Ref. 14 and Hush et al. Ref. 15. The solid curve, R(5p), is discussed in the text and includes monochromator broadening. The dashed curve does not include broadening.

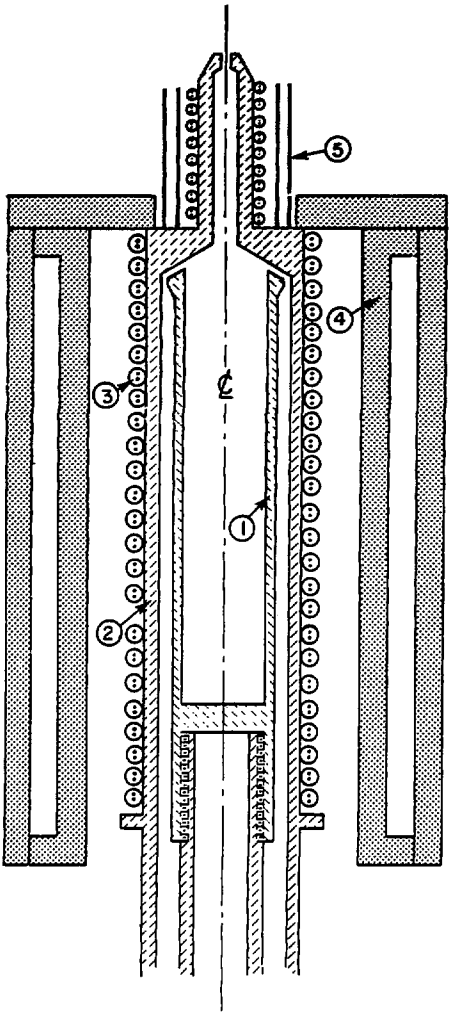

XBL 819-2499

Fig. 1

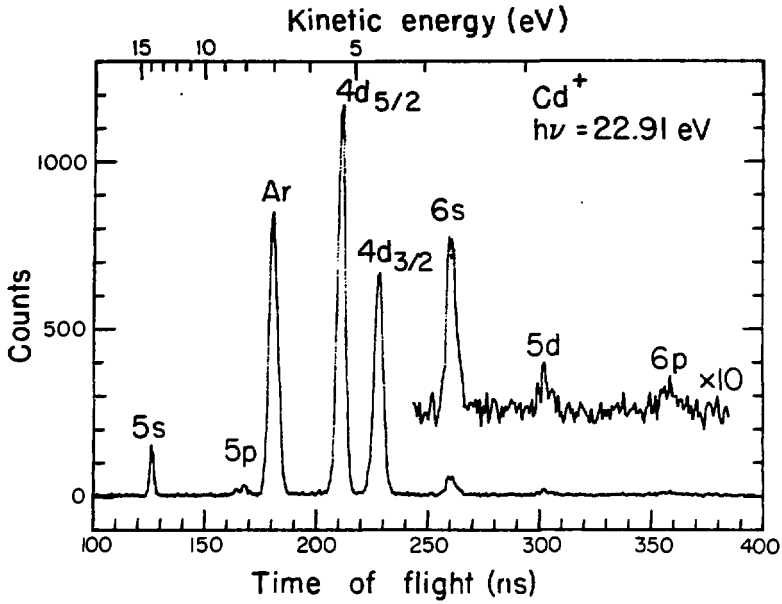

XBL 8110-7344A

Fig. 2

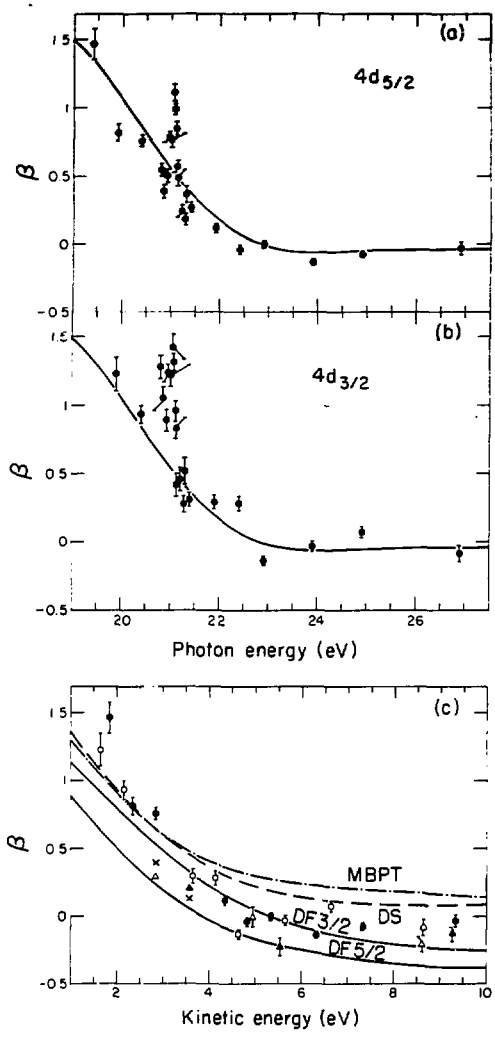
(a)
$4d_{5/2}$
β
(b)
$4d_{3/2}$
Photon energy (eV)
(c)
MBPT
DS
DF3/2
DF5/2
Kinetic energy (eV)
XBL8110-7342A

Fig. 3

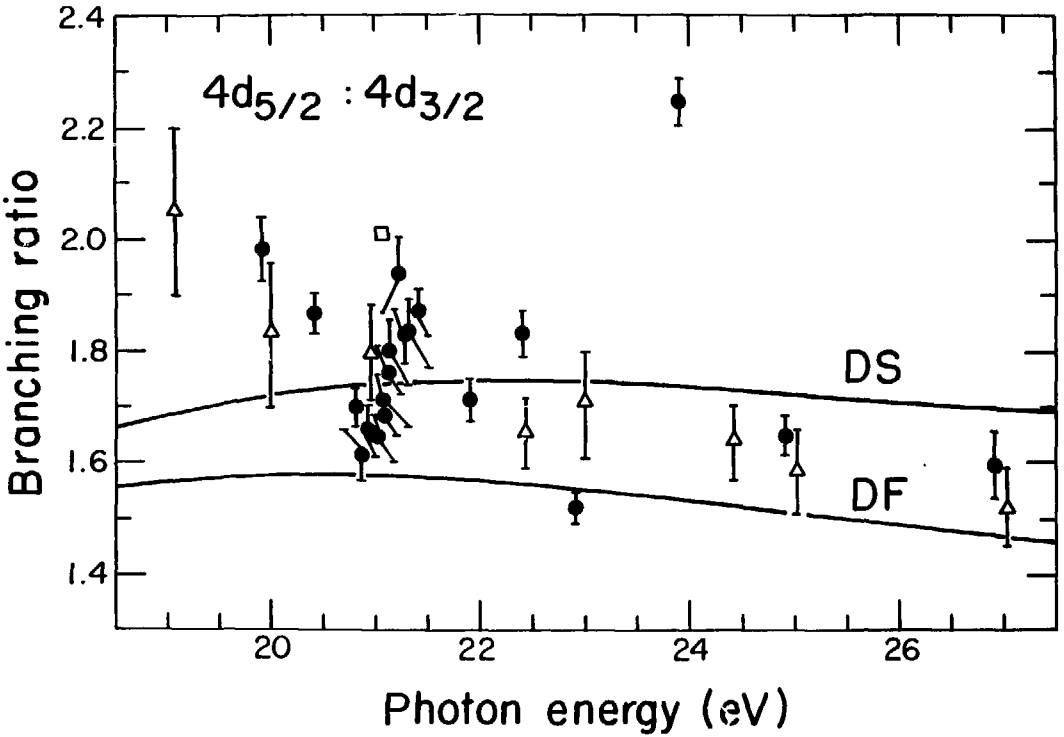

Fig. 4

XBL8110-7350

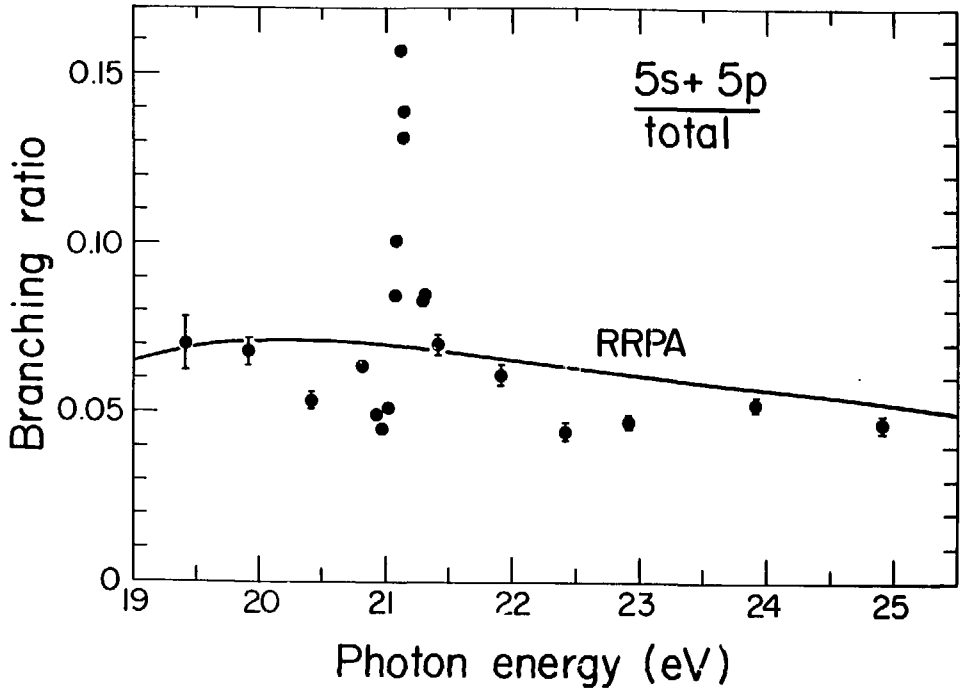

Fig. 5

XBL822-4478

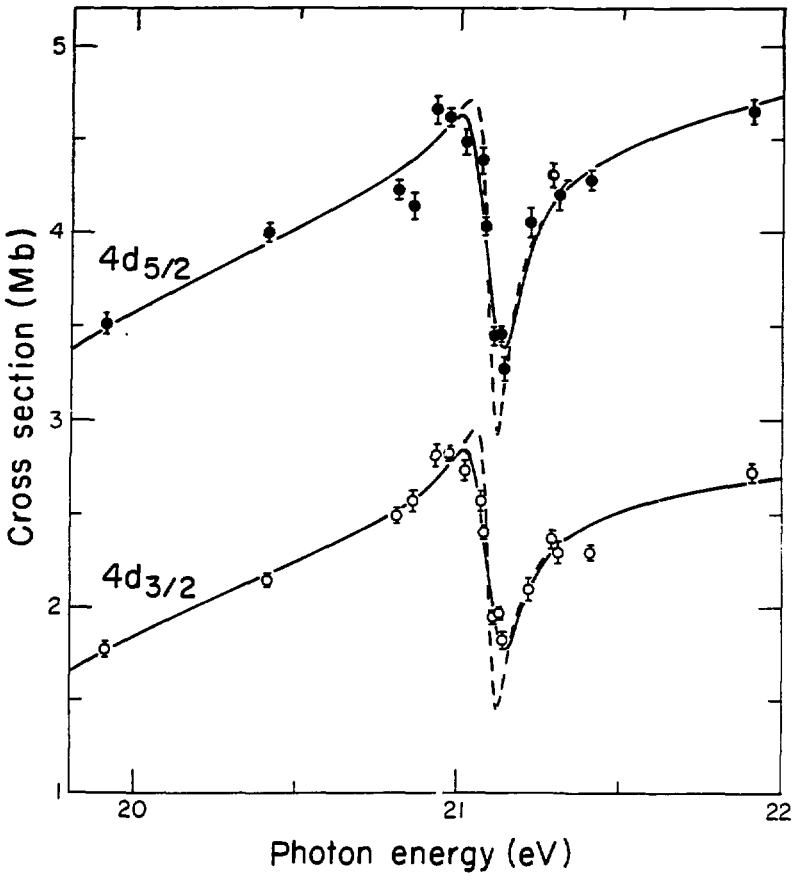

Fig. 6

XBL8110-7353

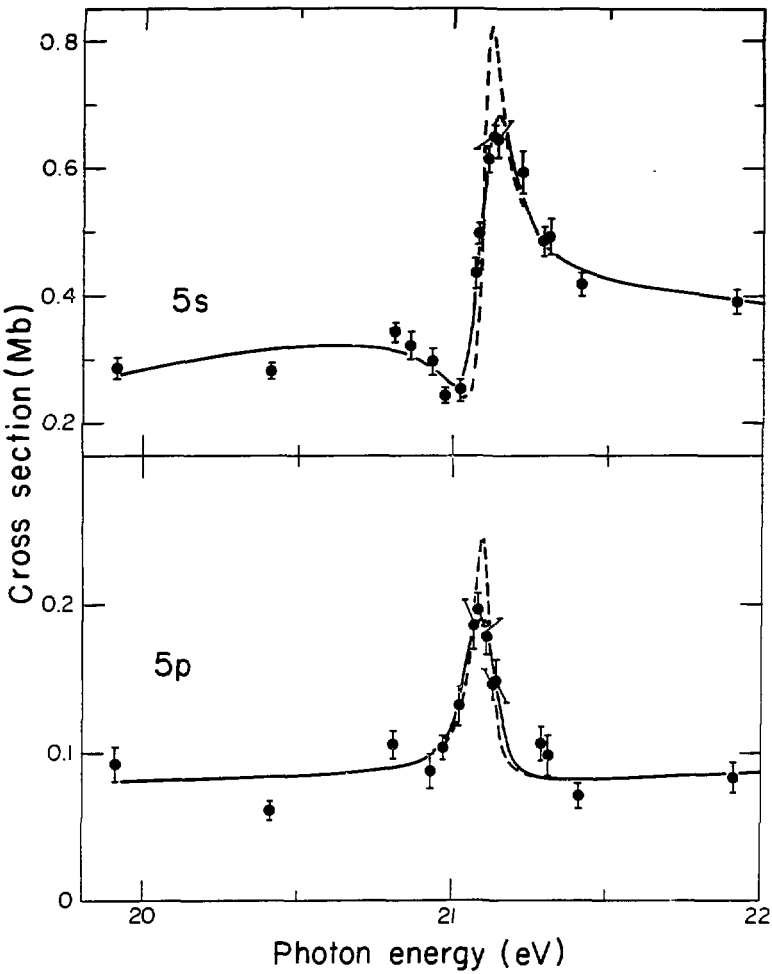

Fig. 7

XBL 8110-7349

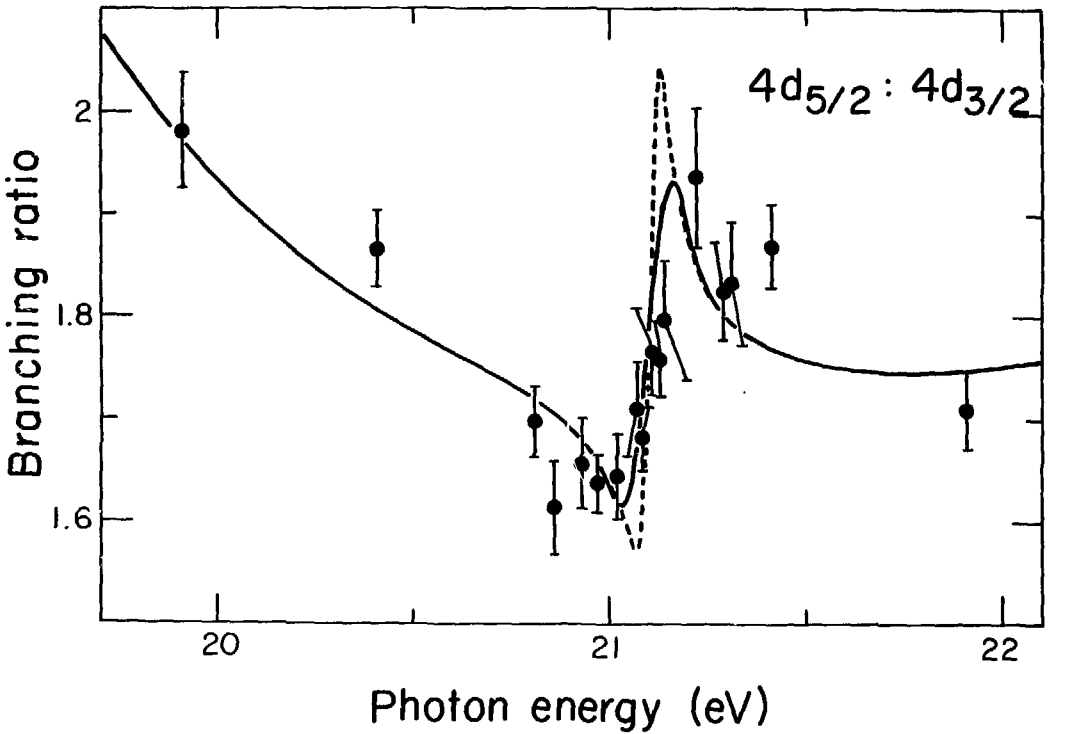

Fig. 8

XBL8110-7347

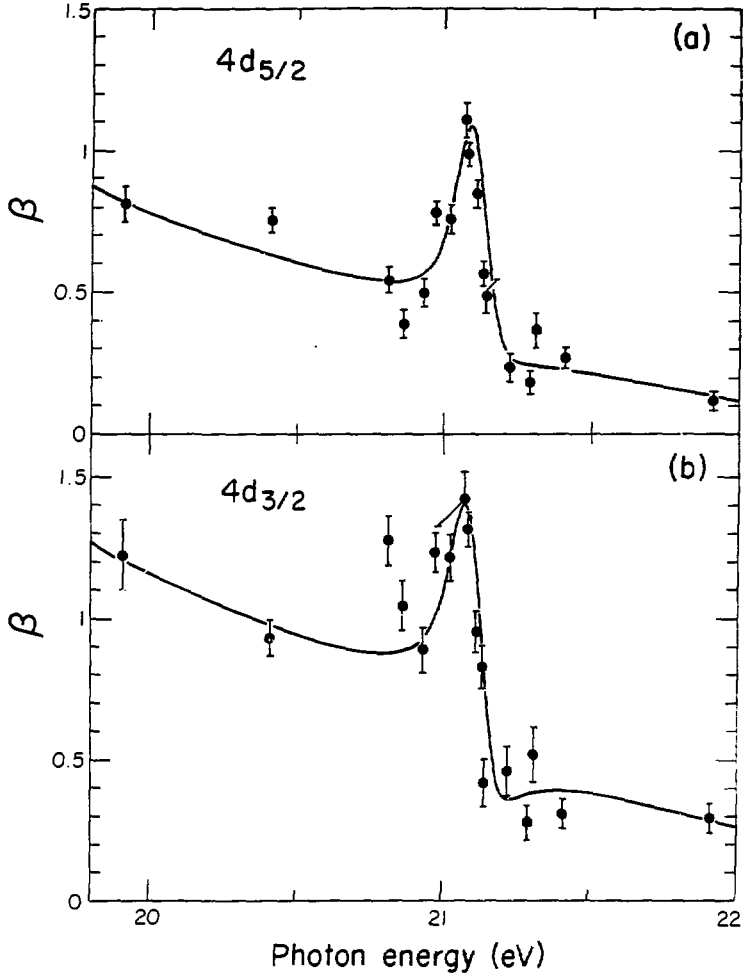

Fig. 9

XBL8110-7343

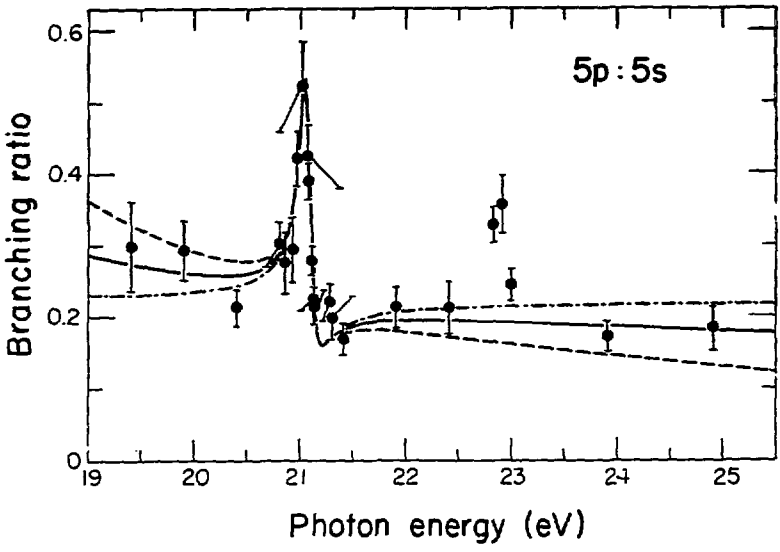

XBL8110-7345A

Fig. 10

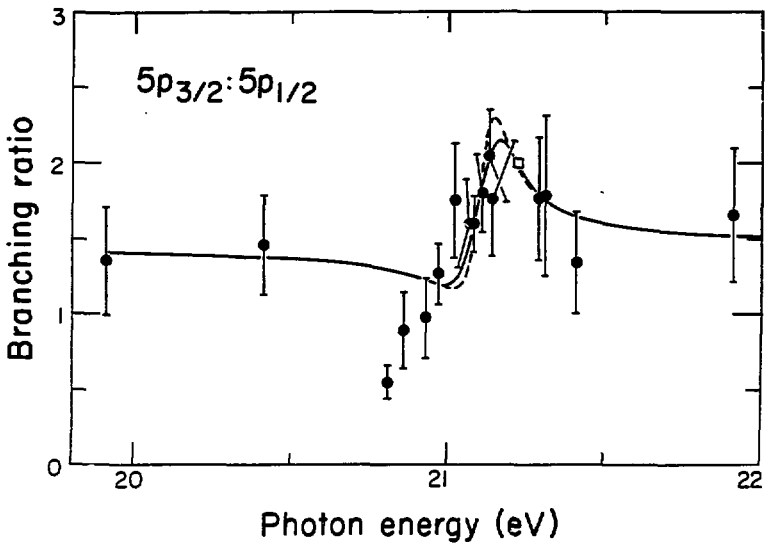

Fig. 11

XBL8110-7346A

IV. PHOTOELECTRON MEASUREMENTS OF THE MERCURY 4f, 5p, AND 5d SUBSHELLS*

ABSTRACT

Photoelectron spectra of atomic mercury have been taken using photon energies between 50 and 270 eV. The relative cross sections, subshell branching ratios and angular distribution asymmetry parameters of the 4f, 5p, and 5d subshells are reported. In addition, the 4f asymmetry parameter was measured up to 600 eV. These quantities show dramatic effects accompanying Cooper minima in the 5d and 5p subshells and a large centrifugal barrier in the $4f \rightarrow \varepsilon g$ channel. Comparisons are made with relativistic random-phase approximation (RRPA) and Dirac-Slater (DS) calculations. Intershell correlations appear responsible for features in the measured 4f asymmetry parameter at the 4d threshold and in the calculated 5d branching ratio at the 5p threshold.

A. INTRODUCTION

Mercury is the heaviest stable element with closed electronic subshells and an appreciable vapor pressure at low temperatures. Relativistic effects in photoionization are thus readily studied in mercury. An absorption spectrum has been reported over a wide energy range,[1] but photoemission studies have been limited to photon energies below 50 eV,[2] and to the discrete energies 132.3 eV[3] and 1486.6 eV.[4] In this paper, we report the first photoemission studies of atomic mercury throughout the photon energy range 50–270 eV, with some additional data, based on second-order light, up to $h\nu = 600$ eV. The 4f, 5p, and 5d subshells were studied.

Several theoretical approaches, which treat exchange, correlation, and relativistic effects in varying degrees of approximation, have been developed and applied to mercury. The 4f partial cross section and photoelectron angular distribution have been calculated by both Shyu and Manson[5] and by Keller and Combet Farnoux[6] with both the Hartree–Slater (HS) and Hartree–Fock (HF) models. Keller and Combet Farnoux have also calculated the 5d and 5p partial cross sections. These studies highlight the influence of intrachannel interactions that are included in HF but not in HS. Walker and Waber[7] have done Dirac–Slater (DS) calculations on the 5d subshell. With this relativistic theory, they are able to predict the branching ratio and the spin–orbit resolved angular distributions. More recent DS calculations have been performed by Tambe and Manson[8] and by Keller and Combet Farnoux.[9] Tambe and Manson[8] have done calculations on the

4f, 5p and 5d subshells. Keller and Combet Farnoux have done calculations on the 4f, 5d and 4d subshells. Radojević and Johnson[10] have used the relativistic random-phase approximation (RRPA) to model the photoionization of mercury over the energy range covered by our experiment. Their method includes both relativistic effects and electron correlations (intershell as well as intrashell). They have coupled all 17 relativistic outgoing channels originating from the 4f, 5p and 5d subshells and have calculated cross sections, branching ratios, and photoelectron angular distributions for each subshell.

Keller and Combet Farnoux[6] have pointed out that the choice of threshold energies in ab initio calculations affects not only the positions of features but also the shapes of the curves. In their HS and HF calculations, they used HS ionization thresholds in order to be self-consistent. On the other hand, Radojević and Johnson employed experimental binding energies in an attempt to account for some of the many-body effects not included in RRPA calculations. Tambe and Manson have used DS values. These various models differ greatly. For the 4f subshell, the DS binding energy lies 30 eV from the HS value, and neither is within 10 eV of experiment. The effects of changing thresholds on the shapes of the curves have not yet been fully explored.

The experiment is described in Sec. B. Results are presented and discussed in Sec. C, and conclusions are summarized in Sec. D.

B. EXPERIMENTAL

The experiment was performed at the Stanford Synchrotron Radiation Laboratory on a grazing incidence "grasshopper" monochromator with a 1200 ℓ/mm holographically-ruled grating. The ultra-high vacuum monochromator was vacuum isolated from our sample chamber by a 1500Å thick window. We used an aluminum window for energies below the aluminum $L_{2,3}$ edge at 72 eV, and we used a vitreous carbon window for energies above 75 eV. For the spectra taken with second-order light above 280 eV, we again used the aluminum window.

The magnitude of the second-order light was determined by comparing the first-order and second-order intensities of the neon 2p photoline. It was only appreciable (>2%) at photon energies less than 150 eV with the carbon window. A correction for second-order light is necessary in the relative cross-section measurements, where the total light intensity, as monitored by a sodium salicylate scintillator and phototube, is used to normalize the data at different photon energies. Because accurate measurements of the energy dependence of the sodium salicylate efficiency are not available, it was assumed to be constant.[11]

Photoelectron spectra were measured with the double-angle time-of-flight (DATOF) system, in which the pulsed time structure of the synchrotron radiation is used to measure the flight times of electrons ejected at two angles. This method has been described in detail elsewhere.[12,13]

The angular distribution of photoelectrons emitted by linearly polarized light in the nonrelativistic dipole approximation has the form

$$\frac{d\sigma(\epsilon,\theta)}{d\Omega} = \frac{\sigma(\epsilon)}{4\pi}[1 + \beta(\epsilon)P_2(\cos\theta)] \qquad (1)$$

where θ is the angle between the polarization vector of the radiation and the momentum vector of the photoelectron. By measuring electron spectra at two angles, it is possible to determine both the cross section, $\sigma(\epsilon)$, and the angular distribution asymmetry parameter, $\beta(\epsilon)$, as functions of electron energy, ϵ. In this work, one analyzer was placed at $\theta = 54.7^\circ$, the "magic" angle where $P_2(\cos\theta) = 0$, and another at $\theta = 0^\circ$. Cross-section measurements require knowing the relative transmission of the 54.7° analyzer as a function of kinetic energy and retarding voltage. The asymmetry-parameter measurements, however, only require knowing the ratio of the transmissions of the two analyzers. Calibration of the spectrometer is accomplished by measuring count rates for the neon 2s and 2p lines, for which $\sigma(\epsilon)$ and $\beta(\epsilon)$ are known.[14] We have corrected for the collection solid angle and an estimated linear polarization of 98%. However, because of the calibration procedures,[12] our derived $\beta(\epsilon)$ values are quite insensitive to the actual value of the polarization.

Representing the angular distribution by Eq. 1 assumes the validity of the dipole approximation, and it is important to know for what values of the photon energy, atomic number, and quantum numbers n and ℓ this is approximation true. The measurement of cross sections at 54.7° (the "magic" angle) are also dependent upon Eq. 1. Kim et al.[15]

found that, for the inner shells of heavier elements, multipole effects are important even at threshold. For outer subshells, they found that the non-dipole effects are small for photoelectron energies below 1 KeV. Recent work by Wang et al.[16] has shown that while the quadrupole matrix element may be small, its contribution to low-energy angular distributions can be appreciable when the dipole intensity is at a minimum (e.g. a Cooper minimum). This whould be particularly pronounced in s-subshell ionization where only $s \rightarrow \varepsilon p$ matrix elements occur. For subshells with $\ell > 0$, the $\ell \rightarrow \varepsilon(\ell-1)$ dipole channel should still dominate over non-dipole channels in regions where the $\ell \rightarrow \varepsilon(\ell+1)$ dipole matrix element is small. We therefore expect the dipole approximation, and therefore Eq. 1, to be valid for all of the subshells addressed in this study.

The oven used to produce the mercury vapor was described earlier.[12] A vapor pressure of ~0.3 torr (100°C) was attained behind a 1.6 mm diameter nozzle. The temperature was monitored by a thermocouple, but the vapor-pressure corrections needed for cross-section measurements were determined by frequently repeating spectra.

Systematic errors introduced into the asymmetry parameter are probably less than 5% of the quantity $\beta+1$. For branching ratios, the probable magnitude of the errors will depend upon the difference between the kinetic energies of the two peaks. If the energy separation is large, the errors may be ~5%; if small, the systematic error will be less. Additional random scatter in the absolute cross-section measurements, on the order of 10%, is due to uncertainty in the sample

pressure correction. This scatter appears as correlated fluctuations in the cross sections of the different subshells and is not present in the branching ratios.

A representative spectrum is shown in Fig. 1. The observed photoelectron lines are listed in Table I, along with their binding energies. In addition to the lines in Table I, a set of $N_{6,7}O_{4,5}O_{4,5}$ Auger lines with constant kinetic energies between 59 and 72 eV were observed.[17]

A retarding cage inside each analyzer allows us to slow the electrons for the final 17 cm of the 28 cm path length. The analyzer resolution, which results primarily from the finite interaction volume, was ~3% of the kinetic energy after retarding. Retarding potentials up to 115 volts were used to resolve the 4f and 5d spin-orbit doublets. Generally, the analyzer and monochromator resolutions were adjusted to provide a total resolution (FWHM) of <2 eV for the 4f doublet and, for some spectra, <1 eV for the 5d doublet. We deconvoluted some of these doublets by a least-squares fitting method that used Gaussian functions with low-energy exponential tails. The weak $5p_{1/2}$ and $5p_{3/2}$ peaks have large natural linewidths (6.2 and 5.6 eV, respectively).[3] The 5p peaks were fitted by Lorentzians with fixed widths and, where possible, fixed doublet spacings.

The error bars for the fitted data represent standard deviations from the computer fits. For the raw data the error bars represent counting statistics only.

C. RESULTS AND DISCUSSION

The format of this section will be to describe in each subsection a derived parameter (e.g. cross section) for all three subshells, with a discussion given in the text for each subshell. A summary paragraph appears at the end of each subsection.

1. Cross Sections

To put our cross-section data on an absolute scale it is necessary to have an experimental measurement of the total cross section at one energy. Using the absorption data of Cairns et al.,[18] with the adjustment of Dehmer and Berkowitz,[19] we have normalized our data so that the 5d partial cross section is 8 Mb at 70 eV. We note that the adjustment in Ref. 19 is only approximate, but should be good to within 30%. We have plotted all of the theoretical curves, which were given in terms of kinetic energy, from the experimental thresholds, thus eliminating energy shifts due to the different choices of thresholds in the calculations.

In Fig. 2 are plotted our 5d cross-section measurements, together with earlier absorption measurements and the RRPA and DS curves. Two RRPA curves are represented in Fig. 2. The calculated curve[20] below 65 eV included interchannel coupling with the 6s channels, while for higher energies, the calculation[10] included coupling with the 4f and 5p channels. These different sets of coupled channels are probably responsible for the discontinuity between the two curves at 65 eV. Both data and theories show the 100-fold decrease from 50 eV to the

Cooper minimum, which can be seen near 190 eV in the data. The minimum is not apparent in the theoretical curves. Above 190 eV, the DS curve lies significantly below the data. Above 70 eV, the RRPA curve has about the same shape as the DS curve, but its magnitude is larger by a factor of 2. Neither of the calculations include core relaxation or double ionization. A Dirac-Fock calculation that includes core relaxation has been performed[21] below 55 eV, and it gives better agreement than either the DS or RRPA calculations.

Although the 6s photoelectron peak (8.E. = 10.4 eV) is unresolved from the 5d peak in almost all of our spectra, we expect its effect to be insignificant, because the cross section for the 6s subshell is much smaller than that for the 5d subshell above 70 eV photon energy.

The 4f cross section is plotted in Fig. 3. The large centrifugal barrier acting on the εg continuum electrons causes a "delayed onset" of the 4f cross section, clearly exhibited in the data. In fact, the decrease in the $4f \rightarrow \varepsilon d$ partial cross section can be seen below 150 eV, before the εg contribution to the 4f cross section becomes dominant. Both the RRPA and the DS curves show larger fractional increases than the data between 150 and 270 eV, but the RRPA curve agrees better with the data both in this respect and in the position of the minimum. The RRPA 4f:5d branching ratio (not shown) is in good agreement with our measurements below 170 eV, while it deviates by a factor of 2 near 270 eV. The agreement of this ratio with the DS theory is significantly worse.

The $5p_{3/2}$ and $5p_{1/2}$ cross sections are plotted in Fig. 4. In both subshells, the experimental cross section below 180 eV drops more quickly than the theoretical curves. The changes in curvature in $\sigma(5p_{3/2})$ near 180 eV and in $\sigma(5p_{1/2})$ near 190 eV are assigned to Cooper minima in these subshells.

In summary, the experimental cross sections generally show the expected energy variations, with minima being readily observed in every case. The 4f "delayed onset" character due to the angular momentum barrier for the g-wave is clearly present. The RRPA cross sections are a factor of 2 too large. However, the RRPA calculated 4f:5p:5d branching ratios generally agree to within 10%, with the notable exceptions being those involving $\sigma(4f)$ above 200 eV and $\sigma(5p)$ below 160 eV. The DS calculated 5p and 5d cross sections are in better agreement with experiment.

2. Spin-Orbit Branching Ratios

Deviations of spin-orbit branching ratios from their statistical $(\ell+1)/\ell$ value arise from the "kinetic-energy" effect,[22] caused by the photoelectrons from the two spin-orbit members having different kinetic energies at a given photon energy. Additional deviations are due to differences in the radial wavefunctions of the initial and final states. Ron, Kim, and Pratt[23] have recently surveyed some of the non-kinetic-energy effects that cause deviations in subshell branching ratios. They found that, for higher Z elements, deviations are amplified by the presence (and by the energy separation) of Cooper minima in dominant channels. They also concluded that these effects should

be larger for np subshells than for nd or nf subshells.

The DS[8] and RRPA[10,20] calculations of the $5d_{5/2}$:$5d_{3/2}$ branching ratio are shown in Fig. 5, along with experimental points from this work and from experiments with line sources. The 5d cross section (Fig. 2) has a large shape resonance peaking near 40 eV photon energy and a Cooper minimum near 190 eV. The experimental branching ratio starts well above the statistical value near threshold[2] and then drops monotonically to a minimum value of ~1.1 near 90 eV. The DS theory predicts this trend qualitatively, while the RRPA result shows an additional feature at 85 eV that may be due to intershell correlations with the 5p subshell. The RRPA curves above and below 65 eV do not join smoothly, presumably due to the different sets of coupled channels used in the two calculations, as mentioned earlier in connection with the 5d cross section. This point needs further study.

The 4f subshell cross section has no Cooper minimum because the 4f radial wavefunction has no nodes, but there is a shape resonance due to the εg centrifugal barrier, and a cross-section minimum near 150 eV. Our 4f branching-ratio data are shown in Fig. 6 with a curve predicted by both the RRPA and DS theories. The curve shows a maximum in the branching ratio between 150 and 200 eV. Our branching-ratio measurements confirm the existence of a maximum rising above 1.5, but the detailed shape is unclear from the data because of non-statistical scatter arising from uncertainties in background corrections. The slower increase in the measured cross section than in the calculated cross sections above 160 eV (Fig. 3) should appear as a smaller branch-

ing ratio, due to the kinetic-energy effect. This is apparent near 200 eV in Fig. 6.

The large spin-orbit splitting in the 5p subshell (18.6 eV) leads to large deviations in the branching ratio from its statistical value of 2.0. Calculation of the 5p → εs and 5p → εd cross sections by Keller and Combet Farnoux[6] show that the εs channel is dominant for the first 200 eV above threshold and that the εd channel goes through a Cooper minimum. The RRPA calculation[10] of the branching ratio shown in Fig. 7 shows an increase from ~1.1 at 110 eV to ~2.8 at 220 eV. Our data show the ratio starting near 0.85 at 25 eV above the $5p_{1/2}$ threshold and increasing to ~2.2 at $h\nu$ = 200 eV. The DS curve is in much better agreement with the data. The gap in the data arises from the Auger group moving through the 5p lines. A much more careful study would be required to fill in the gap.

In summary, deviations from statistical ratios, and variations with energy, were observed for all three subshells. Both RRPA and DS theory predicted the experimental ratios quite well, although the RRPA is in better agreement for the 5d subshell, and the DS is in better agreement for the 5p subshell. Evidence was found for a large kinetic-energy effect in the 5p subshell and for a small shape resonance effect in the 4f subshell. The RRPA theory alone predicted details in the 5d curve that may arise from interchannel coupling. More experimental work is clearly needed on these branching ratios.

3. Asymmetry Parameters

The energy variation of the calculated angular distribution asymmetry parameter, $\beta(\epsilon)$, often complements the variations in the cross section and branching ratio. In the case of Cooper minima, the predicted effects on the $\beta(\epsilon)$ parameter are typically more pronounced than the effects on the other parameters. Few data are available to test these predictions. For example, we report below the first $\beta(\epsilon)$ measurements on any 4f and 5d subshells over a substantial energy range.

The 5d-subshell $\beta(\epsilon)$ parameter shows large oscillations. These are due to a Coulomb phase-shift change just above threshold,[15] then a shape resonance, and then a Cooper minimum. Using the central-field approximation, the $\beta(\epsilon)$ parameter is given in LS coupling by the Cooper-Zare formula[26]

$$\beta(\epsilon) = \frac{(\ell-1)R_{\ell-1}^2 + (\ell+1)(\ell+2)R_{\ell+1}^2 - 6\ell(\ell+1)R_{\ell-1}R_{\ell+1}\cos(\Delta_{\ell+1,\ell-1})}{(2\ell+1)[\ell R_{\ell-1}^2 + (\ell+1)R_{\ell+1}^2]}, \quad (2)$$

where $R_{\ell+1}$ and $R_{\ell-1}$ are radial dipole matrix elements and $\Delta_{\ell+1,\ell-1}$ is their phase difference. At a Cooper minimum, where $R_{\ell+1} = 0$ Eq. 2 simplifies to

$$\beta(R_{\ell+1} = 0) = \frac{\ell-1}{\ell(2\ell+1)} . \quad (3)$$

Equations 2 and 3 were derived neglecting configuration interaction, fine-structure splitting, and the spin-orbit interaction between the

outgoing electron and the ion. If we ignore these complications, we find that the Cooper minimum for the 5d subshell should be located where $\beta(\epsilon)$ reaches 0.1, which is at 190 eV in Fig. 8. The data in Fig. 2 confirm this value, whereas the theoretical curves do not show a minimum.

The DS and RRPA curves for $\beta(\epsilon)$ are generally in good agreement with our data, but they differ by 10–20 eV in the energy of greatest negative slope and in the value of $\beta(\epsilon)$ for energies above the Cooper minimum. It may be that the position of the Cooper minimum, which is due to a cancellation in the R_f radial integral, is extremely sensitive to both the accuracy of the integrating code and the nature of the theory. A similar sensitivity was observed in the position and depth of the minimum in $\beta(\epsilon)$ for the Xe 5s Cooper minimum.[29]

The theoretical curves of $\beta(\epsilon)$ for the unresolved 4f subshell, together with our results, are displayed in Fig. 9. All of these theories show the same general features, but none reproduce the data quantitatively. The most sophisticated of the theories (RRPA) has the energy of the maximum in $\beta(\epsilon)$ 10 eV too high and the $\beta(\epsilon)$ curve above 200 eV 0.2 β-units too large.

The two 4f spin-orbit members have different $\beta(\epsilon)$ values at the given photon energy. Most of this difference results from a kinetic-energy effect. In Fig. 10, we have plotted $\beta(7/2)$-$\beta(5/2)$ against photon energy along with the RRPA calculated curve. The differences calculated from DS theory are almost identical. The data and the theory are in qualitative agreement.

Figure 11 shows $\beta(\epsilon)$ for the 4f subshell from threshold to a photon energy of 600 eV. All but three of the points above 280 eV were taken using second-order light and an aluminum window. The calibration of the relative efficiencies of the analyzers was done with second-order Ne 2s and 2p photoelectrons. The uncertainty in the calibration for kinetic energies above 300 eV introduces an uncertainty in the slope of the data in Fig. 11 (~0.2 β units at $h\nu$ = 600 eV). The calibration is, however, a smooth function. The sudden increase in $\beta(\epsilon)$ at 380 eV is probably the result of interchannel coupling with the 4d ionization channels. Using first order perturbation theory, each 4f transition amplitude is the sum of a direct and a correlation amplitude, the latter resulting from a virtual excitation of the 4d subshell.[30] This correlation amplitude can affect both the 4f cross section and the 4f angular distribution.

The $4d_{5/2}$ and $4d_{3/2}$ thresholds are at 366.0 and 385.4 eV, respectively,[3] where the monochromator bandpass was approximately 7 eV. DS calculations of the 4d subshell[9] show its cross section to be a factor of 10 less than the 4f cross section at 400 eV. The calculated 4d spin-orbit branching ratio[31] and the $\beta(\epsilon)$ parameter[9,31] are calculated to have large fluctuations near threshold which may be manifesting themselves in the 4f $\beta(\epsilon)$. We were unable to measure the 4d photoelectron peaks directly because of their small cross sections and large natural linewidths (4 eV).

Large changes in $\beta(\epsilon)$ due to coupling with newly opened channels have been observed in $\beta_{5p}(\epsilon)$ at the 4d threshold in Xe.[32] However,

in the Xe case the 4d cross section near threshold is much larger than the cross section of the 5p subshell.

Figure 12 shows the $5p_{1/2}$ and $5p_{3/2}$ asymmetry parameter measurements. Again, the gaps in these data are caused by the presence of Auger electrons. The two states show substantial differences beyond that due to the kinetic-energy effect. Our data show $\beta(5p_{1/2})$ dropping to zero, while $\beta(5p_{3/2})$ drops to a value of -0.3. The minimum in each parameter is due to a Cooper minimum in the ϵd channels. If we apply Eq. 3, we would expect the unresolved $\beta_{5p}(\epsilon)$ to drop to zero. Because we have measured the resolved $\beta(\epsilon)$'s, it may be more appropriate to know what value of $\beta(\epsilon)$ we would expect at the minimum in the limit of jj coupling. Walker and Waber[17] have shown that for s-subshell ionization (j=1/2), in which only two relativistic continuum channels are accessible, the expression for $\beta(\epsilon)$ takes on a simple form in jj coupling:

$$\beta(\epsilon,j=1/2) = \frac{2R_{3/2}^2 + 4|R_{3/2}R_{1/2}^*|}{R_{1/2}^2 + 2R_{3/2}^2} \quad . \tag{4}$$

For ionization from a $p_{1/2}$ subshell (again j=1/2), the expression for $\beta(\epsilon)$ is identical. For the $p_{1/2}$ subshell, $R_{1/2}$ and $R_{3/2}$ are radial matrix elements with the $\epsilon s_{1/2}$ and $\epsilon d_{3/2}$ continuum orbitals. When the $R_{3/2}$ matrix element equals zero we obtain $\beta(5p_{1/2}) = 0$, in agreement with experiment. It is not as easy to apply Walker and Waber's formalism to $\beta(5p_{3/2})$, because there are three continuum orbitals ($\epsilon s_{1/2}$, $\epsilon d_{3/2}$ and $\epsilon d_{5/2}$) and the $R_{3/2}$ and $R_{5/2}$ matrix elements

(for the εd channels) need not go through zero at the same energy. If they did, we would again obtain $\beta = 0$. Of course, in the general many-electron case the radial matrix elements are complex and need not go identically to zero.

The RRPA calculation of $\beta(5p_{1/2})$ shows $\beta(\epsilon)$ falling only to 0.5. This is a result of mixing with the 4f-subshell ionization channels, because an 11-channel calculation, which includes only the 5p and 5d subshells, shows $\beta(5p_{1/2})$ dropping to 0.0 at 280 eV.[31] The DS calculation is significantly closer to experiment for the $5p_{3/2}$ subshell, but not for the $5p_{1/2}$ subshell.

In summary, the asymmetry parameter of the mercury 4f, 5p, and 5d subshells behave approximately as predicted by the DS and RRPA models, but there are important differences between experiment and theory. Both theories predict the centrifugal-barrier induced maxima in the 4f subshell to be too wide, with the consequent overestimation of the photon energies where $\beta(\epsilon)$ decreases most rapidly. In addition, a feature was observed in $\beta(4f)$ at 380 eV which we attribute to interaction with the 4d-ionization channels.

D. CONCLUSIONS

Several noteworthy features have been exhibited in the photoionization of Hg above 50 eV.

The Cooper minimum in the 5d-subshell photoionization is observed in both the cross section and the asymmetry parameter. The 5d branch-

ing ratio was found to drop as low as 1.1, although we were unable to test the RRPA prediction that shows oscillating features due to interaction with 5p-subshell ionization.

In the 4f subshell, the centrifugal barrier in the εg channel was observed as a shape resonance in the asymmetry parameter and as a delayed onset in the cross section. An additional oscillation in β(ε) has been attributed to interaction with 4d-subshell ionization.

The 5p subshell, which has the largest spin-orbit splitting, was found to have a branching ratio of 0.85 at low kinetic energies. The two spin-orbit members were found to have different values of β at their respective Cooper minima.

The DS and RRPA theories correctly predict the shapes of all of the parameters, although there are several quantitative differences. Among these, the delayed onset of the 4f cross section shows the worst agreement. There is good agreement with the 4f:5p:5d branching ratios calculated by RRPA, but there is a factor of 2 difference between the calculated absolute cross sections and the present results. The DS cross sections are in better agreement with experiment. Experimentally, there is a need for a reliable absolute absorption measurement, as well as measurements of the Hg^{++}/Hg^{+} ratio.

REFERENCES

*Work done in collaboration with P.A. Heimann, H.G. Kerkhoff, D.W. Lindle, C.M. Truesdale, T.A. Ferrett, U. Becker, and D.A. Shirley (Phys. Rev. A to be published.)

1. J.P. Connerade and M.W.D. Mansfield, Proc. R. Soc. Lond. A. 335, 87 (1973).
2. S.P. Shannon and K. Codling, J. Phys. B 11, 1193 (1978) and references therein.
3. R. Nilsson, R. Nyholm, A. Berndtsson, J. Hedman, and C. Nordling, J. Elec. Spectr. 9, 337 (1976).
4. S. Svensson, N. Martensson, E. Basilier, P.Å. Malmqvist, U. Gelius, and K. Siegbahn, J. Elec. Spectr. 9, 51 (1976).
5. J.S. Shyu and S.T. Manson, Phys. Rev. A 11, 166 (1975).
6. F. Keller and F. Combet Farnoux, J. Phys. B 12, 2821 (1979).
7. T.E.H. Walker and J.T. Waber, J. Phys. B 7, 674 (1974).
8. B.R. Tambe and S.T. Manson, private communication.
9. F. Keller and F. Combet Farnoux, J. Phys. B 15, 2657 (1982).
10. V. Radojević and W.R. Johnson, Physics Lett. 92A, 75 (1982).
11. J.A.R. Samson and G.N. Haddad, J. Opt. Soc. Am. 64, 1346 (1974).
12. S. Southworth, C.M. Truesdale, P.H. Kobrin, D.W. Lindle, W.D. Brewer, and D.A. Shirley, J. Chem. Phys. 76, 143 (1982).
13. P.H. Kobrin, U. Becker, S. Southworth, C.M. Truesdale, D.W. Lindle, and D.A. Shirley, Phys. Rev. A 26, 842 (1982).
14. F. Wuilleumier and M.O. Krause, J. Elec. Spectr. 15, 15 (1979).
15. Y.S. Kim, R.H. Pratt, A. Ron, and H.K. Tseng, Phys. Rev. A 22, 857 (1980).

16. M.S. Wang, Y.S. Kim, R.H. Pratt, and A. Ron, Phys. Rev. A 25, 857 (1982).

17. H. Aksela, S. Aksela, J.S. Jen, and T.D. Thomas, Phys. Rev. A 15, 985 (1977).

18. R.B. Cairns, H. Harrison, and R.I. Schoen, J. Chem. Phys. 53, 96 (1970).

19. J.L. Dehmer and J. Berkowitz, Phys. Rev. A 10, 484 (1974).

20. W.R. Johnson, V. Radojević, P. Deshmukh, and K.T. Cheng, Phys. Rev. A 25, 337 (1982).

21. B.R. Tambe, W. Ong, and S.T. Manson, Phys. Rev. A 23, 799 (1981).

22. T.E.H. Walker and J.T. Waber, J. Phys. B 6, 1165 (1973).

23. A. Ron, Y.S. Kim, and R.H. Pratt, Phys. Rev. A 24, 1260 (1981).

24. S. Süzer, P.R. Hilton, N.S. Hush, and S. Nordholm, J. Elec. Spectr. 12, 357 (1977).

25. S. Süzer, S.T. Lee, and D.A. Shirley, Phys. Rev. A 13, 1842 (1976).

26. J. Cooper and R.N. Zare, Lectr. in Theor. Phys. Vol 11C, pp 317-337, ed. S. Geltman (1969).

27. G. Schönhense, J. Phys. B 14, L187 (1981).

28. A. Niehaus and M.W. Ruff, Z. Physik 252, 84 (1972).

29. M.G. White, S.H. Southworth, P. Kobrin, E.D. Poliakoff, R.A. Rosenberg, and D.A. Shirley, Phys. Rev. Lett. 43, 1661 (1979).

30. M.Ya. Amusia and V.K. Ivanov, Phys. Lett. 59A, 194 (1976).

31. V. Radojević and W.R. Johnson, private communication.

32. M.O. Krause, T.A. Carlson, and P.R. Woodruff, Phys. Rev. A 24, 1374 (1981)

Table I. Binding Energies in eV for Observed Mercury Subshells

Subshell	B.E. (From Ref. 4)
$5d_{5/2}$	14.9
$5d_{3/2}$	16.7
$5p_{3/2}$	71.6
$5p_{1/2}$	90.3
$4f_{7/2}$	107.1
$4f_{5/2}$	111.1

Table II. The 5d cross section, asymmetry parameter, and subshell branching ratio.

hν (eV)	σ (Mb)	β	γ
50	...	0.39(8)	
60	...	0.58(8)	1.21(2)
65	...	...	1.16(2)
70	8.00(7)	0.87(9)	1.23(1)
75	...	0.99(6)	1.22(3)
80	5.86(3)	1.07(1)	
85	...	1.17(9)	1.09(3)
90	4.15(2)	...	
95	...	...	1.08(3)
100	2.76(1)	1.44(1)	
105	2.03(1)	1.50(2)	
110	1.580(6)	1.60(1)	
115	1.298(5)	1.64(1)	
120	0.932(5)	1.88(2)	
125	0.795(6)	1.75(2)	
130	0.595(4)	...	
135	0.502(4)	1.98(3)	
140	0.442(3)	1.90(2)	
145	0.352(3)	1.97(3)	
150	0.225(2)	...	
155	0.214(3)	1.83(4)	
160	0.183(4)	1.55(6)	
165	0.189(5)	1.12(6)	
170	0.142(2)	1.09(4)	
175	0.137(2)	0.67(3)	
180	0.120(3)	0.47(5)	
185	0.110(3)	0.24(5)	
190	0.111(3)	0.19(4)	
195	0.143(5)	-0.26(4)	
200	0.136(7)	-0.15(6)	
205	0.111(7)	-0.16(7)	
210	0.129(4)	-0.39(6)	
220	0.143(7)	-0.35(5)	
230	0.162(13)	-0.42(7)	
240	0.129(8)	-0.27(7)	
250	0.153(12)	-0.30(8)	
260	0.144(8)	-0.20(6)	
270	0.096(2)	...	
275	0.151(19)	-0.31(12)	

Table III. The 4f cross section, asymmetry parameter, subshell asymmetry parameter difference, and subshell branching ratio.

hν (eV)	σ (Mb)	β	$\beta_{7/2}-\beta_{5/2}$	γ
120	0.555(7)	0.71(3)	0.17(6)	1.54(4)
125	0.519(7)	0.734(3)	0.17(6)	1.40(4)
130	0.400(5)	...	0.14(7)	1.34(3)
135	0.495(5)	1.04(3)	0.13(5)	1.37(3)
140	0.379(3)	1.35(2)	0.27(5)	1.18(2)
145	0.344(4)	1.62(3)	-0.22(7)	1.64(4)
150	0.360(3)	...	-0.36(8)	1.82(4)
155	0.421(6)	1.31(4)	-0.11(7)	1.56(4)
160	0.378(7)	1.30(5)	-0.19(10)	1.59(6)
165	0.52(1)	0.83(4)	-0.29(10)	1.73(8)
185	0.64(2)	0.45(4)	-0.33(10)	1.70(10)
190	0.74(2)	0.42(3)	-0.14(7)	1.45(7)
195	0.85(3)	0.17(4)	0.00(8)	1.36(9)
200	0.91(2)	0.10(3)	-0.04(7)	1.41(8)
205	0.84(3)	0.15(4)	-0.04(8)	1.32(8)
210	0.91(1)	-0.01(3)	-0.09(7)	1.37(8)
220	1.07(3)	0.04(3)	-0.07(7)	1.40(8)
230	1.27(7)	-0.12(5)	0.16(11)	1.20(14)
240	1.13(6)	-0.03(5)	-0.04(11)	1.23(12)
250	1.31(6)	-0.01(5)	-0.22(11)	1.46(15)
260	1.30(7)	0.01(6)	-0.15(12)	1.55(17)
270	1.19(1)	...	...	...
275	1.40(11)	0.02(9)	...	...

Table IV. The $5p_{1/2}$ and $5p_{3/2}$ cross section and asymmetry parameter and the 5p subshell branching ratio.

hν (eV)	β(3/2)	β(1/2)	σ(3/2)	σ(1/2)	γ
100	1.52(2)	...	0.90(3)	...	...
115	0.682(8)	0.850(12)	0.96(3)	1.31(3)	0.80(1)
120	0.520(8)	0.613(11)	0.92(4)	1.14(4)	0.85(2)
135	...	0.343(7)	...	1.14(5)	...
140	...	0.235(5)	...	1.21(5)	...
150	0.237(5)	...	...	...	...
155	0.229(4)	...	-0.30(2)	...	...
160	0.182(8)	...	-0.24(5)	...	...
165	0.162(6)	0.099(6)	-0.28(4)	0.61(11)	1.64(11)
170	0.155(3)	0.101(2)	-0.27(2)	0.27(5)	1.51(4)
175	0.137(3)	0.075(3)	-0.36(2)	0.32(6)	1.75(7)
180	0.134(5)	0.078(5)	-0.34(4)	0.06(8)	1.73(12)
185	0.118(5)	0.062(5)	-0.32(4)	0.01(9)	1.89(15)
190	0.120(4)	0.054(4)	-0.14(4)	0.50(12)	2.22(17)
195	0.128(6)	0.057(6)	-0.22(5)	0.22(15)	2.3(3)
200	0.132(10)	0.60(10)	-0.11(8)	0.05(20)	2.2(4)
205	0.126(9)	0.058(8)	-0.01(8)	0.10(19)	2.2(3)
210	0.134(5)	0.048(4)	-0.27(8)	0.2(3)	2.8(2)
220	0.102(8)	...	0.15(11)	...	...
230	0.123(12)	0.063(10)	-0.13(12)	-0.2(2)	1.9(4)
240	0.101(10)	...	0.23(14)	...	...
250	0.121(14)	0.058(14)	0.03(15)	0.1(3)	2.1(6)
260	0.100(8)	0.047(7)	0.26(12)	0.3(2)	2.1(4)
270	0.078(2)	0.043(2)	...	...	1.82(10)

Table V. The 4f asymmetry parameter.

hν (eV)	β	hν (eV)	β
120	0.71(3)	260	0.01(2)
125	0.73(3)	270	-0.07(1)
135	1.04(3)	280	-0.15(2)
140	1.33(2)	300	0.00(2)
145	1.62(3)	310	-0.14(2)
155	1.31(4)	320	-0.09(4)
160	1.30(5)	340	0.07(2)
165	0.83(4)	360	0.09(3)
185	0.45(4)	380	0.43(3)
190	0.42(4)	400	0.46(1)
195	0.17(4)	420	0.26(2)
200	0.07(2)	440	0.29(3)
205	0.15(4)	450	0.12(1)
210	-0.01(3)	460	0.23(3)
220	0.05(3)	480	0.29(3)
230	-0.06(4)	500	0.40(4)
240	-0.05(2)	540	0.46(4)
250	-0.02(3)	600	0.74(8)

FIGURE CAPTIONS

Fig. 1 TOF photoelectron spectrum of Hg taken at $\theta = 54.7°$. There are 5.08 channels per nanosecond, and the accumulation time was 500 sec. The 4f peak at 131 eV is due to second-order light with $h\nu \approx 240$ eV. The 5d peak reaches a maximum of 5200 counts/channel.

Fig. 2 The 5d cross section. The solid curves represent the RRPA calculations, Refs. 10 and 20. There is a discontinuity between the two calculations near 65 eV. The dashed curve represents the DS calculation, Ref. 8. The dashed-dot curve is from absorption measurements (Refs. 18 and 19). The data were normalized to $\sigma(70\ \text{eV}) = 8$ Mb. This sets the scale for all our cross-section data. Data tabulated in Table II.

Fig. 3 The 4f cross section. Solid curve- RRPA-length from Ref. 10; dashed curve- DS from Ref. 8. Data tabulated in Table III.

Fig. 4 The cross section of the $5p_{3/2}$ (upper) and $5p_{1/2}$ (lower) states. The RRPA curves are from Ref. 10 and the DS curves are form Ref. 8. Data tabulated in Table IV.

Fig. 5 The $5d_{5/2}$:$5d_{3/2}$ subshell branching ratio. The solid circles are from this work; open circles from Ref. 24; x's from Ref. 25; square from Ref. 4. The two lower energy x's coincide with measurements from Ref. 19. The solid curves are from two RRPA calculations, Refs. 10 and 20; dashed curve DS theory, Ref. 8. The accuracy of the first two open-circled measurements are ±20% and the third ±40%. No estimates of

the uncertainties for the other line-source measurements were published. Data tabulated in Table II.

Fig. 6 The $4f_{7/2}$:$4f_{5/2}$ branching ratio. Solid curve from RRPA, Ref. 10. The DS theory, Ref. 8, also follows the solid curve. Data tabulated in Table III.

Fig. 7 The $5p_{3/2}$:$5p_{1/2}$ branching ratio. The solid curve RRPA-length and dashed curve RRPA-velocity are taken from Ref. 10. DS curve from Ref. 8. Data tabulated in Table IV.

Fig. 8 The 5d angular distribution asymmetry parameter. The solid curve is RRPA, Refs. 10 and 20; dashed curve, DS from Ref. 8. Experimental measurements below 45 eV (Refs. 27 and 28) are in excellent agreement with the RRPA curve. Data tabulated in Table II.

Fig. 9 The 4f asymmetry parameter. The theoretical curves are: solid- RRPA, Ref. 10; dashed-dot HF, Ref. 6; dotted- HF, Ref. 5; dashed- DS theory, Ref. 8. Data tabulated in Table III.

Fig. 10 The difference between the $4f_{7/2}$ and $4f_{5/2}$ $\beta(\epsilon)$ parameters. The solid curve is the RRPA calculation from Ref. 10 which is almost identical to the DS curve from Ref. 8. Data tabulated in Table III.

Fig. 11 The 4f asymmetry parameter. Data tabulated in Table V.

Fig. 12 Asymmetry parameter, $\beta(\epsilon)$, for the $5p_{3/2}$ (top panel) and $5p_{1/2}$ (lower panel) states. The RRPA curves are from Ref. 10 and the DS curves are from Ref. 8. Data tabulated in Table IV.

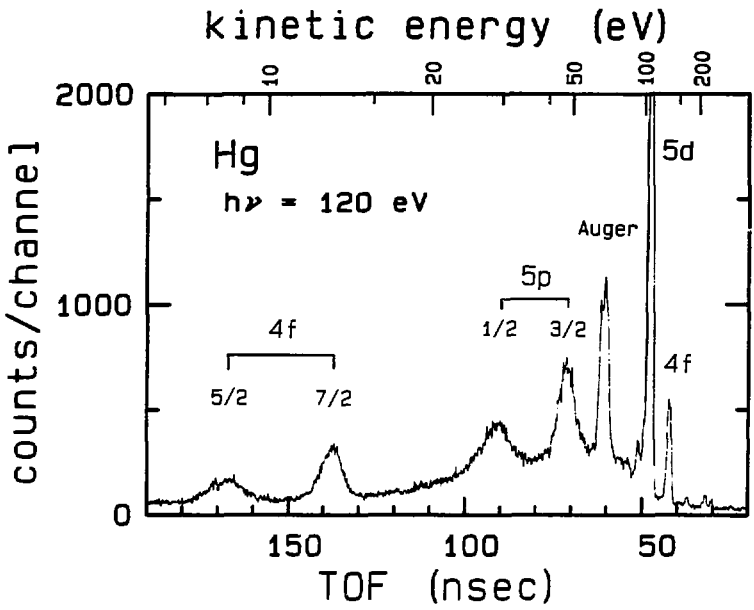
kinetic energy (eV)
10
20
50
100
200
2000
1000
0
counts/channel
Hg
hν = 120 eV
5d
Auger
5p
1/2
3/2
4f
5/2
7/2
4f
150
100
50
TOF (nsec)
XBL 9210-2998

Fig. 1

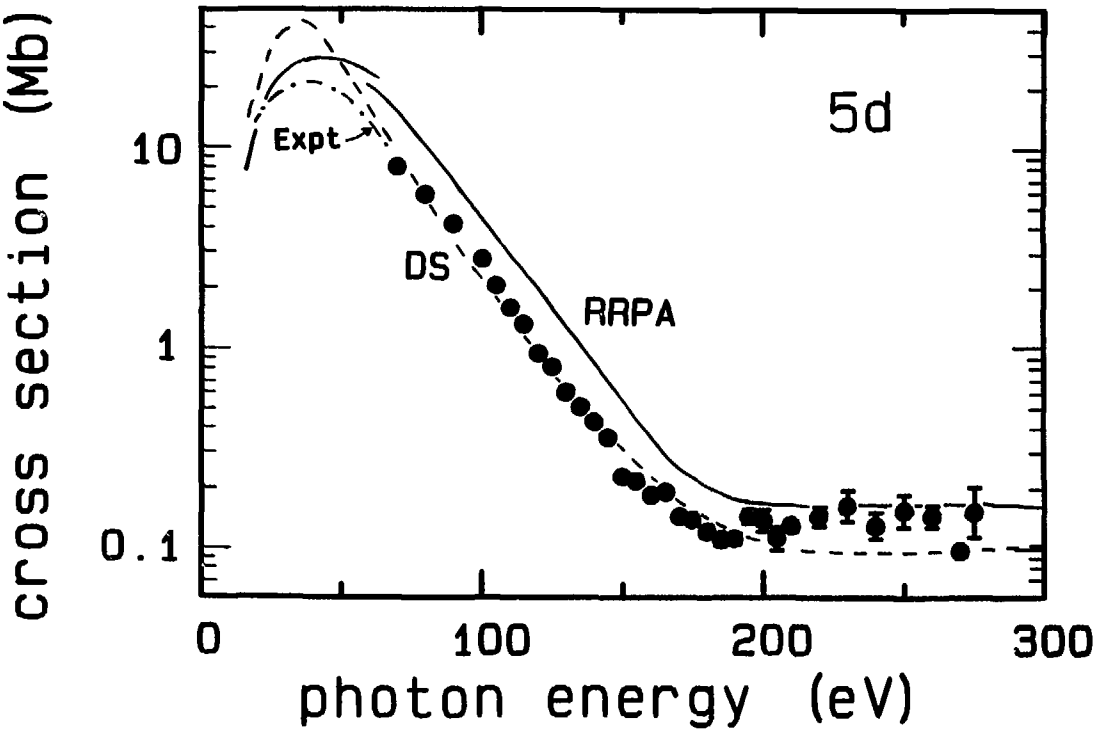

Fig. 2

XBL 8211-7448

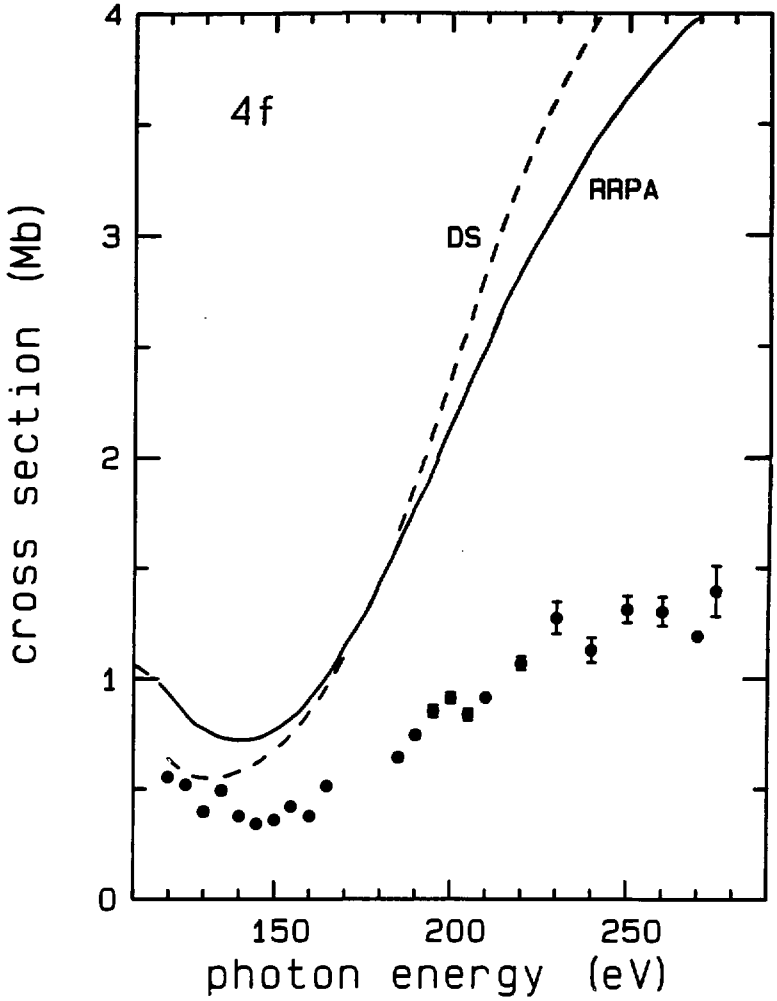

XBL 8210-2938

Fig. 3

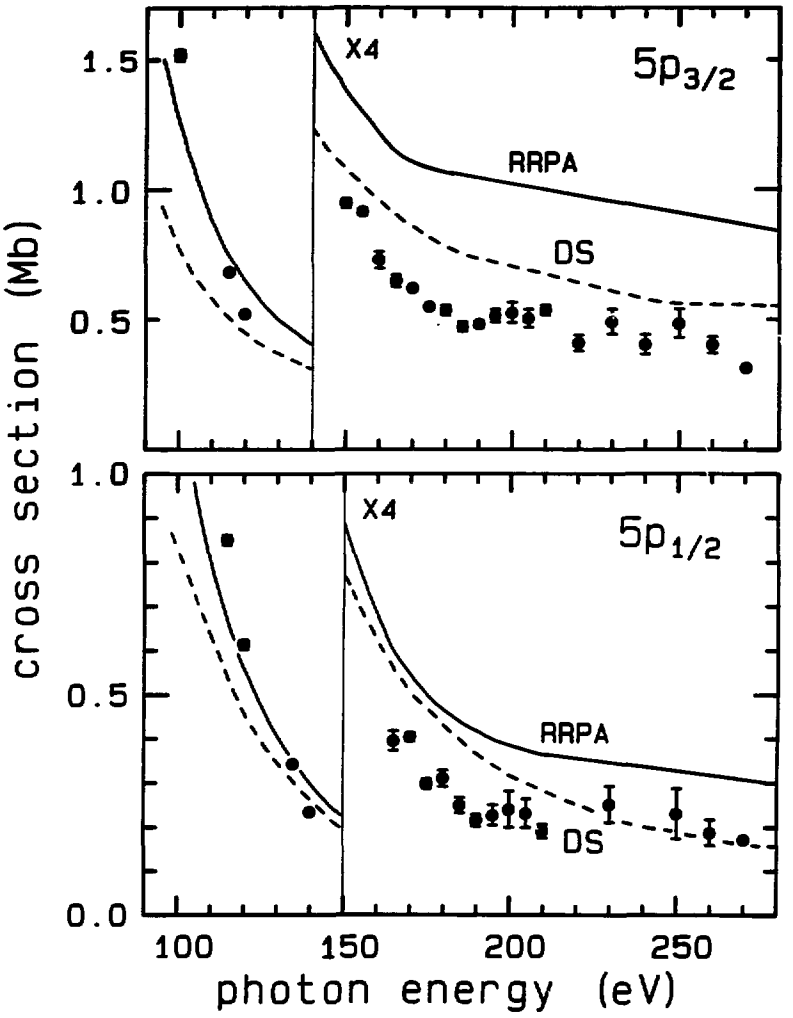
1.5
1.0
0.5
X4
5p3/2
RRPA
DS
cross section (Mb)
1.0
0.5
0.0
X4
5p1/2
RRPA
DS
100
150
200
250
photon energy (eV)
XBL 8210-3032A

Fig. 4

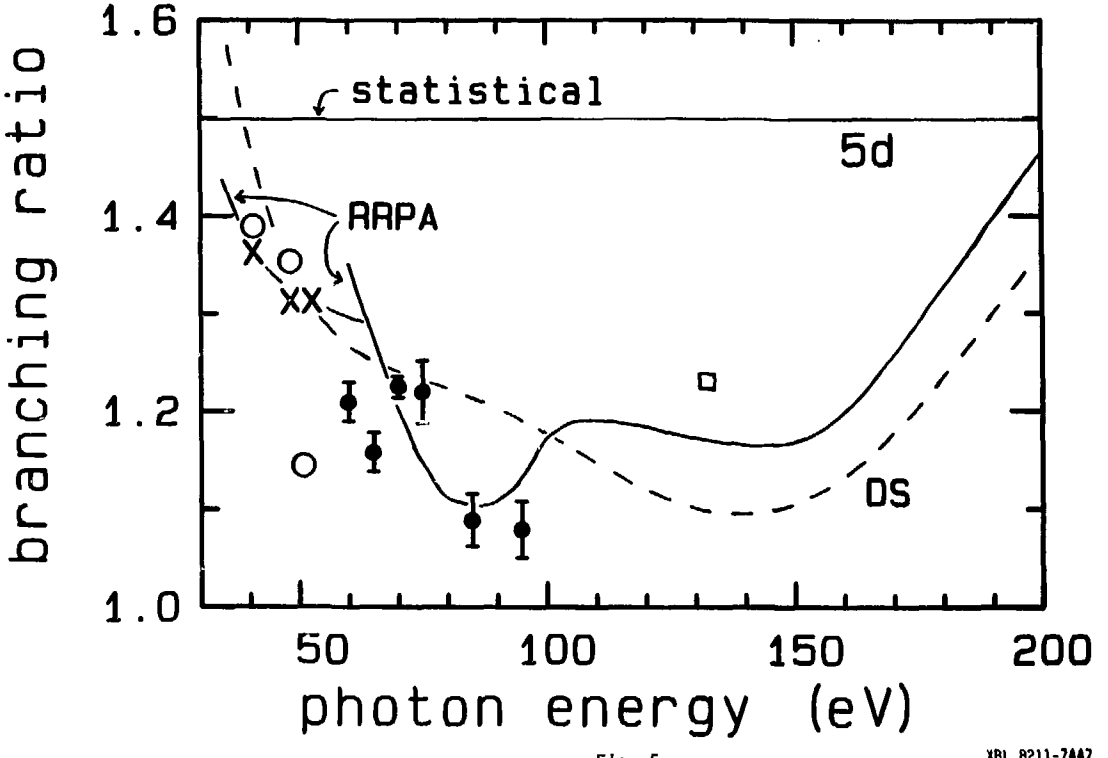

Fig. 5

XBL 8211-7447

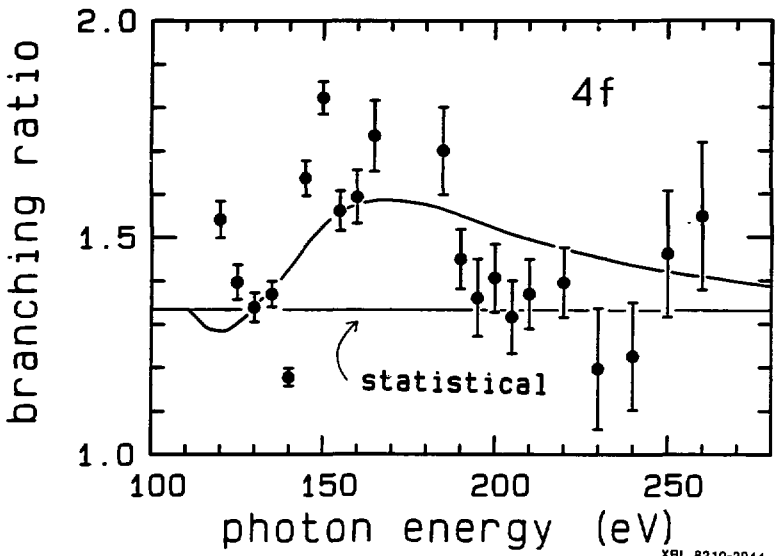
2.0
1.5
1.0
branching ratio
4f
statistical
100
150
200
250
photon energy (eV)
XBL 8210-2944

Fig. 6

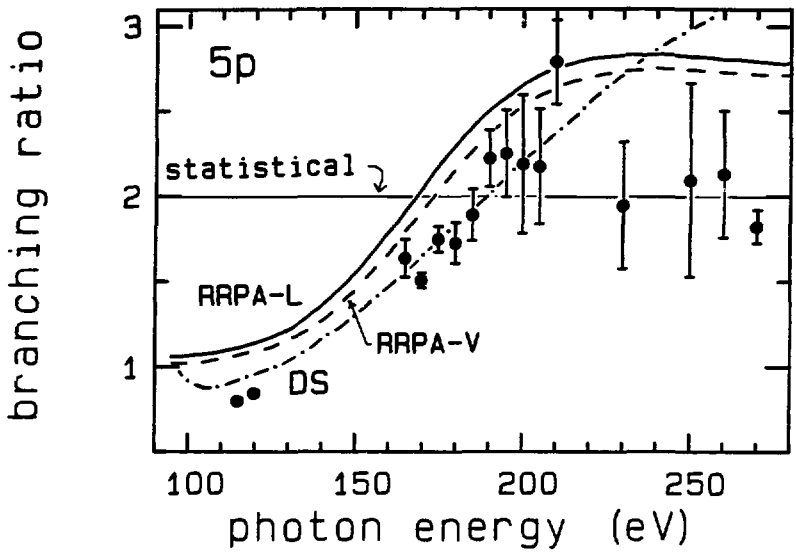
branching ratio
3
2
1
5p
statistical
RRPA-L
RRPA-V
DS
100
150
200
250
photon energy (eV)
XBL 9210-2997A

Fig. 7

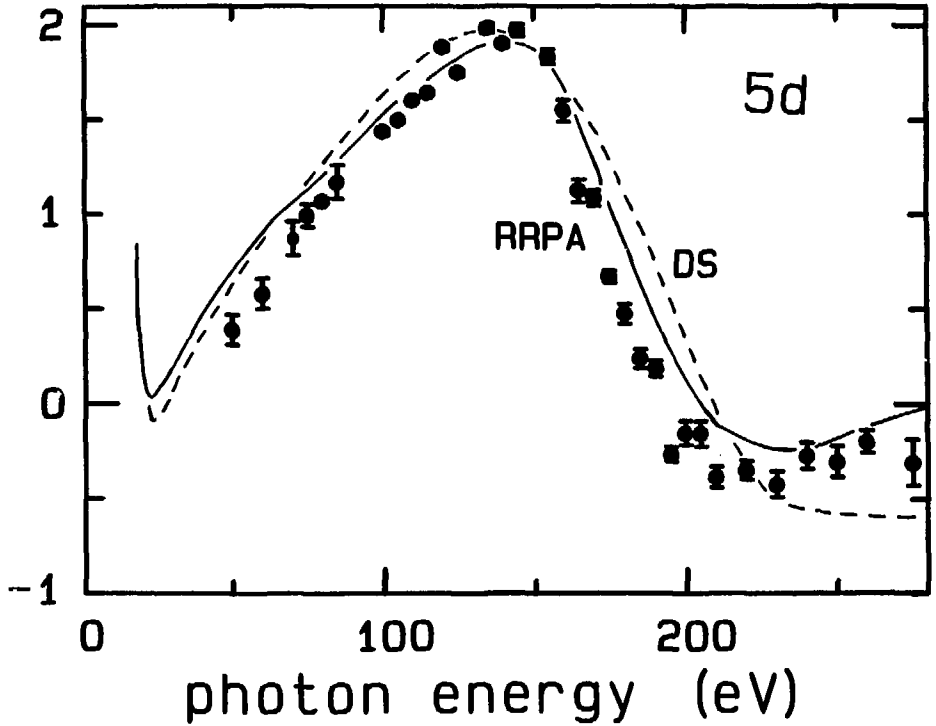

Fig. 8

XBL 8211-7446

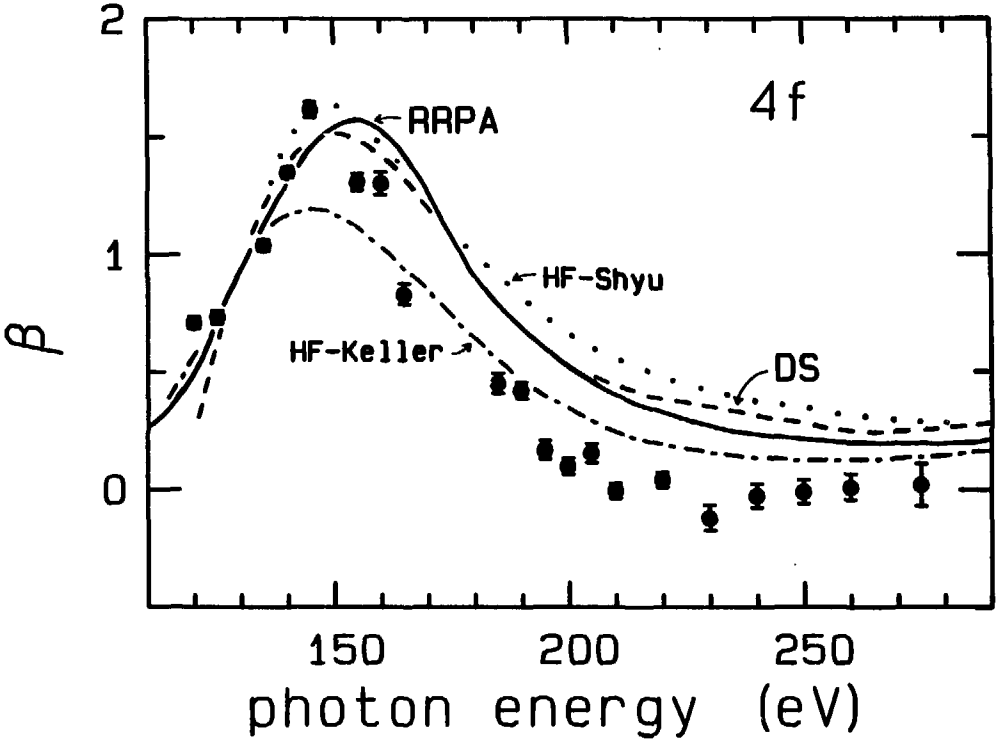

Fig. 9

XBL 8210-2941

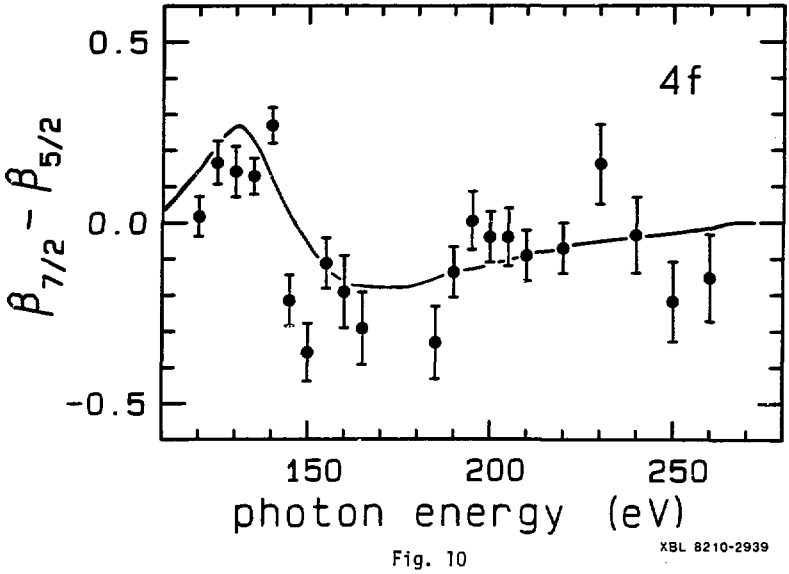
0.5
0.0
-0.5
$\beta_{7/2} - \beta_{5/2}$
4f
150
200
250
photon energy (eV)
XBL 8210-2939

Fig. 10

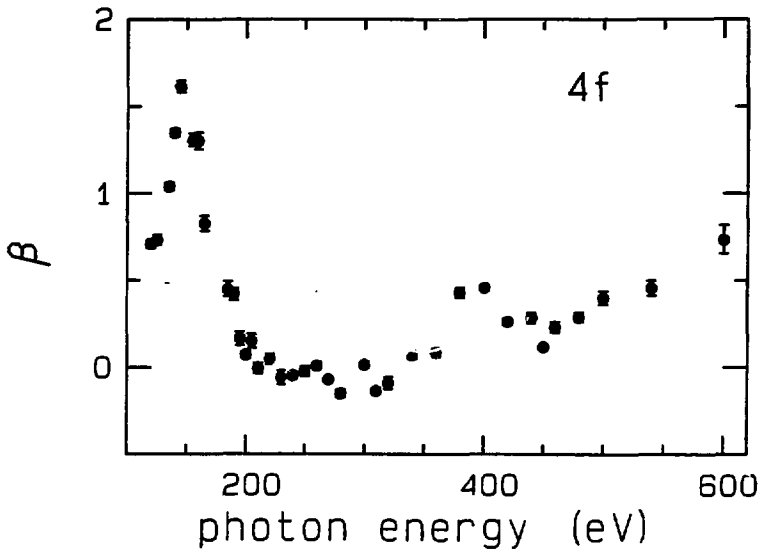

Fig. 11

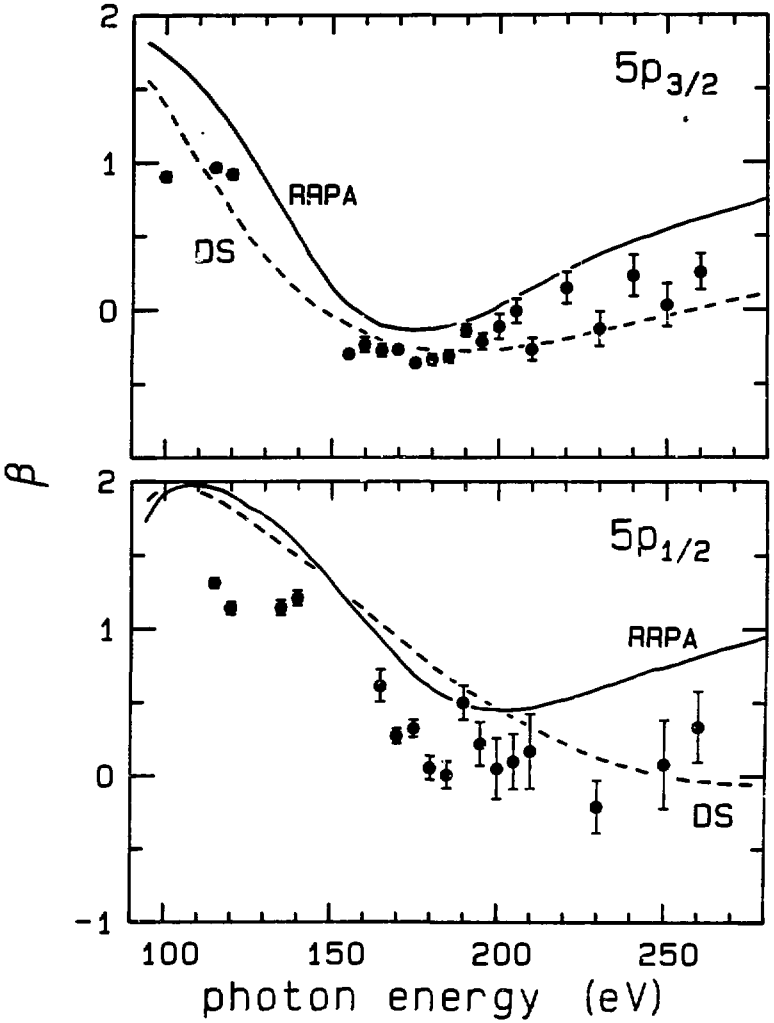

XBL 8210-3033A

Fig. 12

V. THRESHOLD MEASUREMENTS OF THE K-SHELL PHOTOELECTRON SATELLITES IN Ne AND Ar*

ABSTRACT

The relative intensities of K-shell photoelectron satellites in Ne and Ar have been measured near their respective thresholds using synchrotron radiation. The Ne satellites were found to be 20-40% smaller than in the high-energy limit. The 2p → 3s "conjugate shakeup" state of Ne^+ was not observed, in contrast to predictions of many-body perturbation theory. The asymmetry parameter of the neon Auger group was found to be equal to zero at the 1s → 3p resonance at 867 eV. This result suggests that the 3p Rydberg electron is essentially decoupled from the core in the Auger decay process. In argon, a K-shell satellite was observed at 24.6(3) eV with 6% intensity relative to the main line, confirming a theoretical prediction by Dyall. Tentative evidence was obtained that this branching ratio increases with energy in the first 90 eV above threshold.

A. INTRODUCTION

Inner-shell photoelectron spectra of closed-shell atoms typically show an intense peak at the binding energy of each electronic subshell, and weaker "satellite peaks" at higher binding energies. The satellites arise via photoionization to higher energy states of the ion, which are approximately described by configurations formed by the removal of a core electron and the promotion of a valence electron to a higher sub-shell. Thus, for example, the main peak in Ne 1s photoionization would correspond to the $Ne^+(1s2s^22p^6)$ state, while a typical satellite configuration would be $Ne^+(1s2s^22p^53p)$. Because the presence of satellites cannot be explained in an independent-particle description of the atom, but rather require a many-electron picture, they are known as "correlation satellites". The study of these satellites is important for an understanding of the many-particle nature of atomic structure and the photoionization process.

A heuristic approach to correlation satellites is the "shake" theory,[1] in which the above description is used to estimate satellite intensities by projecting the passive orbitals of the neutral atom onto those of the ion, in which these orbitals have relaxed in response to the new atomic potential. This procedure is best suited to phenomena well above threshold and is implicitly limited to a one-configuration description of each state.

A more general approach to correlation satellites, capable of extension to the energy range closer to threshold, is an explicit treatment of electron correlation with methods based on configuration

interaction (CI). In this framework, the equivalence of photoionization channels leading to the "main" ionic final state and the "satellite" states are explicitly recognized, as is the equivalence of these states as eigenstates of the N-1 electron Hamiltonian, independent of any reference to photoemission.[2,3] Three different CI mechanisms that contribute to satellite intensities have been classified: initial-state configuration interaction (ISCI) and final-ionic-state configuration interaction(FISCI), which are photon-energy independent; and continuum-state configuration interaction (CSCI), which is highly energy-dependent and more important near threshold. Many calculations have been made of satellite intensities in the high-energy, or sudden, limit where CSCI effects are less important.[3-9] For the Ne 1s correlation satellites, Martin and Shirley[9] have shown that both ISCI and FISCI are required to obtain good agreement with the experimental intensities observed at high energy.

Far less is known about the energy-dependence of satellite intensities.[10-12] In the photoionization of He, the relative intensity (the satellite to main line ratio) of the 2s state was found[13,14] to be constant up to 60 eV above threshold, while the relative intensity of the 2p state decreased by a factor of 3. The He 2s state is referred to as a "shake-up" satellite, because it differs from the main line by a $1s \rightarrow 2s$ excitation. The 2p state is referred to as a "conjugate shake-up" satellite, because it differs from the main line by a $1s \rightarrow 2p$ excitation and a consequent change in parity. CSCI is more important for conjugate shake-up satellites, and they are therefore

more energy dependent. For the Ne 2s and 2p shake-up states, the relative intensities near threshold were found to be less than half of their high-energy values.[10] Also, the relative intensities of the Ne 2s satellites reach a maximum at an intermediate energy.

Except for the special case of the $He^+(n=2)$ satellites, the only energy-dependent calculations to date have been on Li,[15] Fe,[16] and on the 2p → 3s satellite in the Ne K-shell spectrum. Ishihara, Mizuno, and Watanabe[17] have used many-body perturbation theory (MBPT) to model the continuum processes that give intensity to this Ne conjugate shake-up peak. Their calculated relative intensity of 0.1% at 600 eV kinetic energy is in good agreement with the Al Kα measurement.[18] They also predict that the satellite intensity increases to almost 5% of the main line near threshold. The MBPT calculation has, however, been performed only in lowest order and only in the dipole length form.

With the advent of the availability of high-energy synchrotron radiation, it is now becoming feasible to study correlation satellites near core-level thresholds, thereby addressing these more subtle questions of the energy-dependences of satellite intensities. We present in this report the first such measurements for K-shell satellites of neon (K-shell binding energy = 870.2 eV) and argon (K-shell binding energy = 3206 eV). The experimental procedures are described in Section B and results are given in Section C.

B. EXPERIMENTAL

Radiation from the electron storage ring SPEAR at the Stanford Synchrotron Radiation Laboratory was monochromatized by "JUMBO", a constant-deviation double-crystal monochromator on Beam Line III-2.[19] Beryl crystals were used for the Ne spectra between 860 and 960 eV, and germanium crystals were used for the Ar spectra between 3210 and 3320 eV. The photon flux was higher with the germanium crystals than with the beryl crystals. The monochromator bandpass (FWHM) was approximately 0.75 eV for the Ne spectra and approximately 1.7 eV for the Ar spectra. The storage ring was operated in the parasitic mode at 6-12 mA and 1.85 GeV so that the photon flux was an order of magnitude lower than during high-energy dedicated operation. Count rates for the satellite lines were low (0.1 - 0.2 sec^{-1} in Ne and 0.2 - 0.6 sec^{-1} in Ar), reflecting their low cross sections (0.01 Mb in Ne and 0.005 Mb in Ar). Despite these constraints, we were able to obtain the highest energy gas-phase photoelectron spectra ever recorded with synchrotron radiation. This was made possible by the high efficiency of our time-of-flight (TOF) electron analysis.

Our TOF spectrometer has been described previously.[20] Each spectrum was accumulated for 30-100 minutes. The sample pressure was $1X10^{-3}$ torr in the chamber, approximately $5X10^{-3}$ torr in the interaction region and less than $3X10^{-5}$ torr in the electron analyzers which were differentially pumped. A 1500Å thick vitreous carbon window was used to isolate the spectrometer from the ultra-high vacuum monochromator.

The electron energy resolution was increased by retarding the photoelectrons over part of their flight path. The energy resolution of the TOF analyzer is approximately a fixed fraction of the kinetic energy of the photoelectron after retardation. This fraction was 0.05 for this experiment. The resolution is limited by the size of the horizontal focus (5 mm) on the JUMBO monochromator.

Two TOF analyzers were operated at positions of 0° and 54.7° with respect to the photon polarization direction. The intensity, $I(\theta)$, of a given photoelectron peak is dependent on the photoelectron angular distribution

$$I(\theta) \propto \frac{d\sigma(\theta)}{d\Omega} = \frac{\sigma}{4\pi}\left[1 + \beta P_2(\cos\theta)\right]$$

where σ is the partial cross section and β is the angular distribution asymmetry parameter. For K-shell shake-up satellites, the satellite and the main line are expected to have $\beta = 2$. Because the 0° analyzer receives a factor of 3 more intensity for these lines, we have used it for the branching ratio measurements. Because the β values are equal, no angular correction to the intensity ratios should be necessary. For the Ne $2p \rightarrow 3s$ "conjugate shake-up" satellite the β parameter may be different from 2.0, and branching ratio measurements from the 0° analyzer must be treated accordingly.

Using the TOF method, all electrons are accumulated simultaneously so that the observed branching ratios are independent of photon flux and gas pressure fluctuations. The transmission of the analyzer as a

function of electron kinetic energy and retarding voltage was calibrated by comparing the intensity of the main Ne 1s peak to the intensity of the KLL Auger peak. Any variations in this ratio are attributed to a varying analyzer transmission for the (much lower energy) 1s peak.

Both analyzers are required to measure the β parameter.[21] We used this double-angle time-of-flight (DATOF) method to measure the β parameter of the KLL Auger electrons in Ne above the 1s threshold and the corresponding autoionization electrons at the 1s $\rightarrow$ 3p resonance below threshold.

C. RESULTS

Figure 1 shows a TOF spectrum of Ne taken at 930 eV, which is 23 eV above the threshold of the first shake-up satellite, $3p_L$ (see Table I). In this spectrum, the resolution in the energy region of the satellites is approximately 1.2 eV. No evidence of the 2p $\rightarrow$ 3s conjugate shake-up peak is seen between the main line and the $3p_L$ line. The $3p_L$ peak is well resolved, while the $3p_U$ and $4p_L$ peaks are unresolved but isolated from the remaining satellites. Above the $4p_L$ satellite in binding energy, there are known to be several weaker, unresolved satellites that are not discernible in this spectrum.

The satellite intensities relative to the main line from several spectra are displayed in Fig. 2. The error bars shown are standard deviations which represent both counting statistics and the uncertainty in back-ground subtraction. For the $3p_L$ satellite, we find that the

mean relative intensity is approximately 2.3(2)%, which is 25% below the value obtained at a photon energy of 1487 eV (Al Kα x-rays).[18] For the sum of the $3p_U$ and $4p_L$ satellites, we obtain a relative intensity of 3.2(2)%, 40% below the Al Kα value. The data in Fig. 2(b) appear roughly unvarying with energy, while those in Fig. 2(a) appear to be decreasing with increasing energy. The data in both plots show fairly large errors and considerable scatter. Nevertheless, they are unique in being the first core-level satellite intensity measurements very close to threshold, and thus some new conclusions can be drawn. First, the satellite intensities are substantially lower than observed in the high-energy limit (Al Kα x-rays). Similar behavior was observed by Wuilleumier and Krause[10] for the Ne 2s and 2p levels with fixed-energy photon sources. Their measurements differed markedly from ours in the photon energy range, data density, proximity to threshold, and the fact that they studied valence-shell photoemission satellites. Nevertheless, qualitatively similar behavior was observed. Wuilleumier and Krause plotted their relative satellite intensities against a reduced energy parameter, ϵ/E_0, where ϵ is the satellite kinetic energy and E_0 is the energy required to "promote" a 2p electron from the main ionic-state configuration to form the dominant satellite configuration. For their 2p-photoemission case, E_0 is 34.3 eV. For our 1s-photoemission case, E_0 is ~37-40 eV (Table I). Wuilleumier and Krause observed a constart relative satellite intensity in the high-energy limit, $\epsilon/E_0 \gg 1$, and a decrease in relative intensity for lower values of ϵ/E_0, which they interpreted as approaching a

finite limit for $\epsilon/E_0 \to 0$, although their lowest measurements fell at $\epsilon/E_0 = 2$. Our measurements, in contrast, cover the low energy range $0.1 \leq \epsilon/E_0 \leq 1.4$. Thus, our results extend these studies, for core levels, into a new reduced-energy domain—the adiabatic limit—in which the photoelectron is moving as slowly as even the most weakly bound passive electrons. Under these conditions, the wave functions of these passive electrons can relax adiabatically to follow the slowly varying atomic potential as the photoelectron leaves, and thus, the sudden approximation is no longer valid.

In the CI formalism for describing correlation satellites,[2,3] the satellites can be treated as eigenstates of the ion, completely equivalent to the "main" peak, and their intensities near threshold are expected to vary with kinetic energy in the same way as that of the main peak, to first approximation. Thus, the observed intensity ratio should vary as

$$\frac{I_i(h\nu)}{I_0(h\nu)} = C_i \frac{\sigma_0(h\nu - B_i)}{\sigma_0(h\nu - B_0)}$$

where i labels a particular satellite, 0 labels the main line, C is a constant, and B stands for binding energy. Using the Ne(1s) cross-section data of Wuilleumier,[22] we find that the above ratio is essentially constant throughout our data range, in agreement with our results.

The MBPT calculation by Ishihara, et al.[17] of the 3s conjugate shake-up satellite shows the intensity decreasing from 5% to 2% between threshold and 50 eV kinetic energy. The calculation also shows that

the β parameter changes from -0.4 to +1.7 in this energy range. Both of these parameters are required to predict the intensity observed at $\theta = 0^\circ$. The kinetic energy of the 3s satellite would be 25 eV for the spectrum shown in Fig. 1. At this energy, the MBPT calculated intensity at $\theta = 0^\circ$ is 2.7%. Satellite $3p_L$ in Fig. 1 has an intensity of 2.5%. We conservatively estimate that the conjugate shake-up satellite must have an intensity of less than 0.7% in order not to have been observed above background in this spectrum.

Also present in the neon TOF spectrum was a peak arising from the unresolved Ne KLL, KLM, etc. Auger lines. Figure 3(a) shows the intensity of this peak, taken with the 0° detector, plotted versus photon energy near the Ne 1s threshold. The photon flux was monitored by the electron yield from a carbon-coated plate in the back of the chamber. The Auger yield curve in Fig. 3(a), measured with a photon energy bandpass of 0.7 eV, looks quite similar to the absorption spectrum of neon.[21] The non-zero intensity at $h\nu = 866$ eV and below arises from unresolved valence photoelectrons, with some probable additional contributions from Auger transitions produced by scattered and second-order light. At 867.0 eV and 867.5 eV, the Auger yield rises sharply because of $1s \rightarrow 3p$ resonance absorption followed by Auger decay or valence autoionization. Additional $1s \rightarrow np$ resonances start at 869.0 eV and lead up to the direct ionization threshold at 870.2 eV.

The asymmetry parameter β of the total Auger group was measured as a function of photon energy (Fig. 3(b)). Above $h\nu = 870.2$ eV, the Auger group arises predominantly from decay of the 1s hole state:

$$Ne(1s^2 2s^2 2p^6; {}^1S) + h\nu(>870.\ eV) \rightarrow e^-(\varepsilon p) + Ne^+(1s2s^2 2p^6; {}^2S)$$

$$Ne^+(1s2s^2 2p^6; {}^2S) \rightarrow e^-(\text{Auger}) + Ne^{2+}(1s^2 2s^n 2p^{6-n}; {}^{1,3}L_J)\ ,\ n = 0,\ 1,\ 2.$$

These are the "normal" KLL Auger transitions following 1s ionization. There are five $^{1,3}L_J$ Auger peaks, all unresolved in our spectra. Because the $Ne^+(^2S)$ intermediate state is spherically symmetrical, it must be randomly oriented in space. Thus, β is required to be identically zero for <u>each</u> unresolved component and hence for the total unresolved Auger peak.[24] We have used this fact to calibrate the relative efficiency of the two analyzers. Thus β was <u>set</u> equal to zero for the average of the four highest energy points.

In Fig. 3(a), the two data points at $h\nu = 867.0$ and 867.5 eV arise almost entirely from the 1s → 3p resonance excitation. Electron spectroscopy studies of analogous inner-shell resonant states in Kr and Xe show that the resonant states decay predominantly by Auger processes in which the Rydberg electron remains as a spectator.[25,26] We assume here that similarly the Ne 1s → 3p resonant state decays primarily by KLL Auger transitions in which the 3p electron remains as a spectator. Thus, the excitation and decay steps are:

$$Ne(^1S) + h\nu(867\ eV) \rightarrow Ne^*(1s2s^2 2p^6 3p; {}^1P_1)$$

$$Ne^*(^1P) \rightarrow e^-(\text{Auger}) + Ne^+(1s^2 2s^m 2p^{7-m} 3p)\ .$$

The resonant Auger electrons are ejected from a $Ne^*(^1P_1)$ state, so one would expect in principle that they could be produced with anisotropic angular distributions. However the measured asymmetry of the

unresolved resonant Auger group was $\beta \approx 0$, which indicates one of the following:

(1) $\beta \approx 0$ because non-zero β values for individual Auger transitions average out to zero.

(2) $\beta \approx 0$ because the 3p electron acts as a non-participating "spectator", essentially decoupled from the core. Hence the Auger electrons are ejected isotropically from the unaligned $Ne^+(^2S)$ core, as they are above threshold.

High-resolution Auger studies are needed to decide between (1) and (2) and to isolate the valence electron signal from the Auger electrons. Probably both of these mechanisms contribute to some extent.

Finally, we note that the positive values of β for photon energies below 867 eV are consistent with the expected high-energy behavior of valence-shell photoemission, which accounts for most of the electron intensity in the region $h\nu < 867$ eV.

Figure 4 shows a TOF spectrum of Ar taken at $h\nu = 3270$ eV. At 4.6(3) eV above the 1s line in binding energy, there is a satellite with 6.0(5)% of the intensity of the main line. The width of the satellite peak in this spectrum is 3 eV FWHM. This satellite can be compared to the $3p^5 4p$ satellite of the Ar 2p peak observed by Bristow, et al.[7] with Mg $K\alpha$ x-rays. The 2p satellite is 23.5 eV from the 2p main line and has an intensity of 6.0%. This similarity for different core-shell vacancies is predicted by the simple shake-up model.[27] Shake theory calculations of the Ar 1s satellite spectrum by Dyall[28] show a $[1s3p]4p(^1S)^2S_{1/2}$ satellite with an excitation energy of 24.4 eV and an intensity of 6.2%. (The square brackets designate the

hole configuration.) These calculations also show 0.9% intensity in other satellite peaks at lower binding energies, but within 1 eV. Additional satellites with higher binding energies are calculated at positions over 3 eV from the $3p^5 4p$ peak. Thus, Dyall's predictions of the energy and approximate intensity are confirmed.

Our measurements of the [1s3p]4p satellite intensity between 23 and 84 eV kinetic energy (Fig. 5) show evidence for increasing relative intensity with increasing energy. This result is of interest because the data range in Fig. 5 lies in the intermediate region of relative energy ϵ/E_0, between the adiabatic low-energy limit and the sudden high-energy limit. For the Ar 1s data, E_0 is 24.6 eV, and the range $1.0 \leq \epsilon/E_0 \leq 3.6$ is covered. Wuilleumier and Krause[10] found strong increases in the relative intensities of the neon valence-shell satellites over a similar range of ϵ/E_0.

In a complementary experiment, Deslattes, et al.[29] have measured K-shell fluorescence spectra from Ar after excitation with monochromatized photons in the 3163-3606 eV range. They measured the relative intensity of fluorescent peaks from a single [1s] vacancy and from [1s3p] and [1s3s] double vacancies. Each of these three fluorescent peaks may have contributions from Ar neutral, Ar^+, and Ar^{2+}. The [1s3p] fluorescent intensity is ~30% relative to the [1s] intensity in the energy range of Fig. 5 which, in light of our results, implies that species other than [1s3p]4p are responsible for most of this intensity.

REFERENCES

*Work done in collaboration with S. Southworth, C.M. Truesdale, D.W. Lindle, U. Becker, and D.A. Shirley.

1. T. Åberg, Phys. Rev. 156, 35 (1967).
2. R.L. Martin and D.A. Shirley, J. Chem. Phys. 64, 3685 (1976).
3. S.T. Manson, J. Elect. Spect., 9, 21 (1976).
4. K.G. Dyall and F.P. Larkins, J. Phys. B 15, 203 (1982) and references therein.
5. K.G. Dyall and F.P. Larkins, J. Phys. B 15, 219 (1982).
6. J.D. Talman, G.M. Bancroft, and D.D. Johnston, Phys. Rev. A 24, 669 (1981).
7. D.J. Bristow, J.S. Tse, and G.M. Bancroft, Phys. Rev. A 25, 1 (1982).
8. H. Smid and J.E. Hansen, J. Phys. B 14, L811 (1981).
9. R.L. Martin and D.A. Shirley, Phys. Rev. A 13, 1475 (1976).
10. F. Wuilleumier and M.O. Krause, Phys. Rev. A 10, 242 (1974).
11. M.Y. Adam, F. Wuilleumier, N. Sandner, V. Schmidt, and G. Wendin, Journal De Physique 39, 129 (1978)
12. M.Y. Adam, F. Wuilleumier, S. Krummacher, V. Schmidt, and W. Mehlhorn, J. Phys. B 11, L413 (1978).
13. D.W. Lindle, T.A. Ferrett, U. Becker, P.H. Kobrin, C.M. Truesdale, H.G. Kerkhoff, and D.A. Shirley, to be published.
14. P.R. Woodruff and J.A.R. Samson, Phys. Rev. A 25, 848 (1982).
15. F.P. Larkins, in Proceedings of International Conference on X-Ray and Atomic Inner-Shell Physics - 1982 (X-82) Ed. B. Crasemann (AIP, New York) 1982.

16. H.P. Kelly, Phys. Rev. A 6, 1048 (1972).

17. T. Ishihara, J. Mizuno, and T. Watanabe, Phys. Rev. A 22, 1552 (1980).

18. U. Gelius, J. Elec. Spectr. 5, 985 (1974).

19. Z. Hussain, E. Umbach, D.A. Shirley, J. Stohr, and J. Feldhaus, Nucl. Instrum. Meth. 195, 115 (1982).

20. M.G. White, R.A. Rosenberg, G. Gabor, E.D. Poliakoff, G. Thornton, S.H. Southworth, and D.A. Shirley, Rev. Sci. Instrum. 50, 1268 (1979).

21. S.H. Southworth, C.M. Truesdale, P.H. Kobrin, D.W. Lindle, W.D. Brewer, and D.A. Shirley, J. Chem. Phys. 76, 143 (1982).

22. F. Wuilleumier, Adv. X-Ray Anal. 16, 63 (1973).

23. F. Wuilleumier, Journal De Physique Colloq. C4, Supp. 10, 32, 88 (1971).

24. S. Flugge, W. Mehlhorn, and V. Schmidt, Phys. Rev. Lett. 29, 7 (1972).

25. W. Eberhardt, G. Kalkoffen, and C. Kunz, Phys. Rev. Lett. 41, 156 (1978).

26. S. Southwork, U. Becker, C.M. Truesdale, P.H. Kobrin, D.W. Lindle, S. Owaki, and D.A. Shirley, Phys. Rev. A (in press).

27. D.P. Spears, H.J. Fischbeck and T.A. Carlson, Phys. Rev. A 9, 1603 (1974).

28. K.G. Dyall, private communication.

29. R.D. Deslattes, R.E. LaVilla, P.L. Cowan, and A. Henins, Phys. Rev. A 27 (1983).

Table I. Summary of the Neon K-Shell Peaks

Line	Assignment	Excitation Energy (eV)[b]	Relative Intensity 930 eV	1487 eV[b]
1s	$1s2s^2 2p^6\ ^2S$	(870.4)	100	100
3s	$1s2s^2 2p^5 3s\ ^2P$	33.4	<0.7[c]	0.06(1)
$3p_L$	$1s2s^2 2p^5 3p\ ^2S$ (lower)[a]	37.4	2.3(2)	3.15(8)
$3p_U$	$1s2s^2 2p^5 3p\ ^2S$ (upper)[a]	40.8	3.0(2)	3.13(10)
$4p_L$	$1s2s^2 2p^5 4p\ ^2S$ (lower)[a]	42.3		2.02(10)

[a]The "lower" and "upper" notation is used to distinguish between two states with the same configuration.[9]

[b]From Ref. 18

[c]Corrected for $\beta = 1.3$

FIGURE CAPTIONS

Fig. 1 Electron TOF spectrum of Ne. The accumulation time is 100 minutes, and there are 2.4 channels per nsec. The peak assignments are given in Table I. The 2p → 3s conjugate shake-up satellite is not observed. Not shown is the KLL Auger peak at channel 736. The K-shell shake-off threshold occurs at an excitation energy of 47.4 eV.

Fig. 2 The intensities of the $3p_L$ satellite (a), and the sum of the satellites $3p_U$ and $4p_L$ (b), relative to the intensity of the 1s main line (≡ 100), plotted versus satellite kinetic energy.

Fig. 3 Yield (a) and asymmetry parameter (b) of the unresolved high-energy peak from Ne, versus excitation energy. The unresolved peak contains KLL, KLM, etc. Auger lines, in addition to valence-shell photoelectrons. Of interest are the two 1s → 3p resonance emission points at 867.0 and 867.5 eV and the four points above the $Ne^+(1s)^{-1}$ threshold at 870.2 eV. By setting the mean value of β equal to zero for the points above 870.2 eV to calibrate the spectrometer, $\beta \equiv 0$ was determined for the 867.0 and 867.5 eV points. The five points between (with $\beta \equiv 0$) arise from several mechanisms, while those for $h\nu < 867$ eV (with $\beta \equiv 0.6$) arise mainly from valence electrons.

Fig. 4 Electron TOF spectrum of Ar at $h\nu = 3270$ eV with a 5 volt retarding potential. The accumulation time is 50 minutes, and there are 4.8 channels per nsec.

Fig. 5 Variation of the Ar 24.6 eV satellite intensity, relative to the main line (=100), as a function of satellite kinetic energy. Although the data scatter, the apparent increase is of interest because the data lie in the intermediate range of relative energy ϵ/E_0 between the adiabatic and sudden limits. Taking $E_0 = 24.6$ eV, the range for these data is $1.0 \leq \epsilon/E_0 \leq 3.6$.

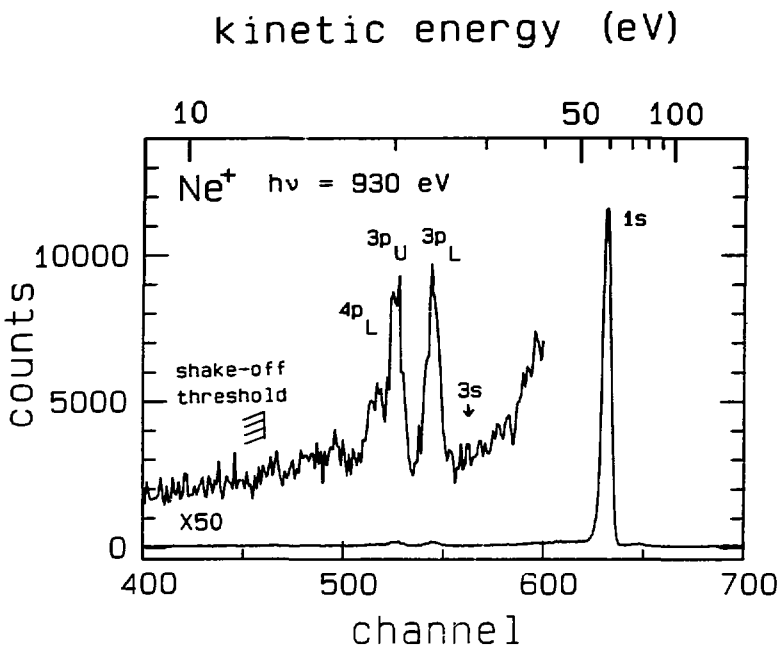
kinetic energy (eV)
10
50
100
Ne+ hν = 930 eV
3pU
3pL
1s
4pL
shake-off
threshold
3s
X50
10000
5000
0
counts
400
500
600
700
channel
XBL 8212-12153

Fig. 1

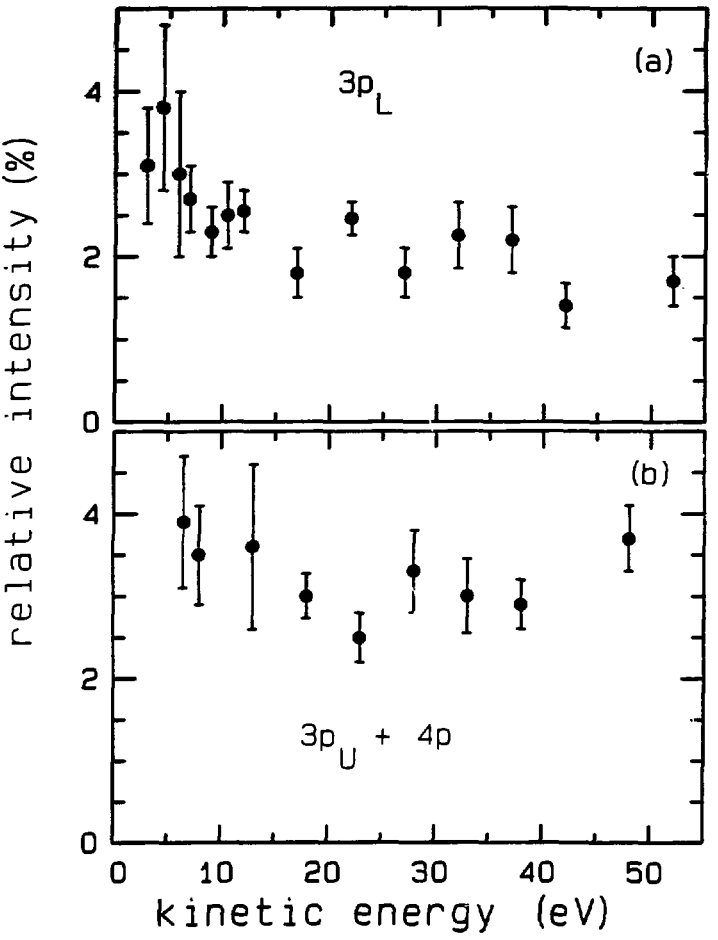

XBL 8212-12222

Fig. 2

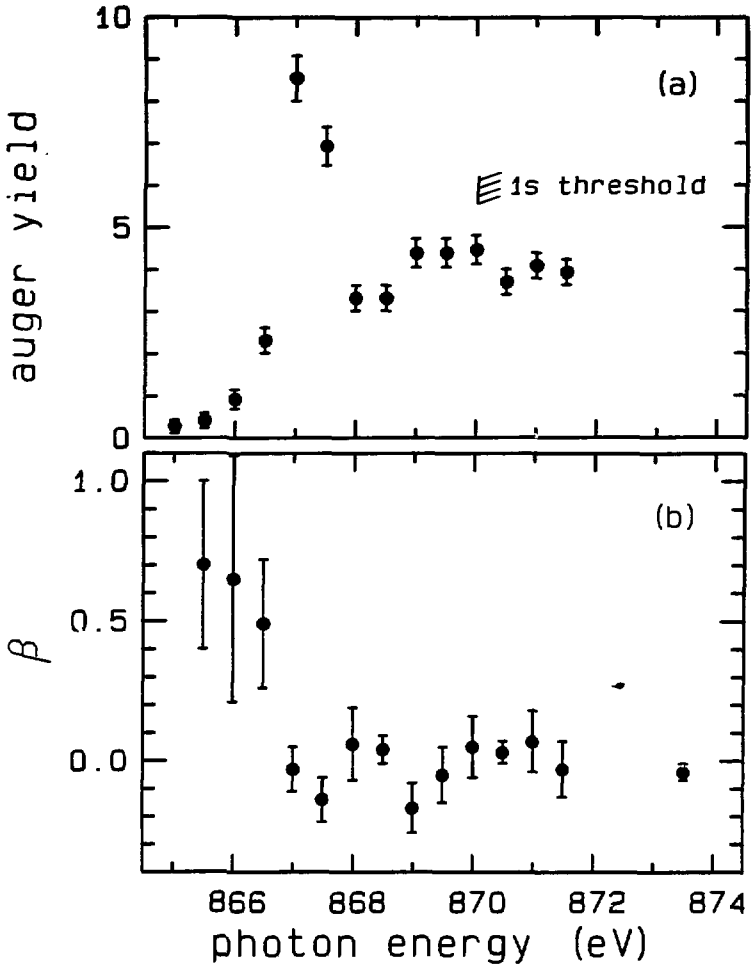
10
5
0
auger yield
(a)
1s threshold
1.0
0.5
0.0
β
(b)
866
868
870
872
874
photon energy (eV)
XBL 8212-12155

Fig. 3

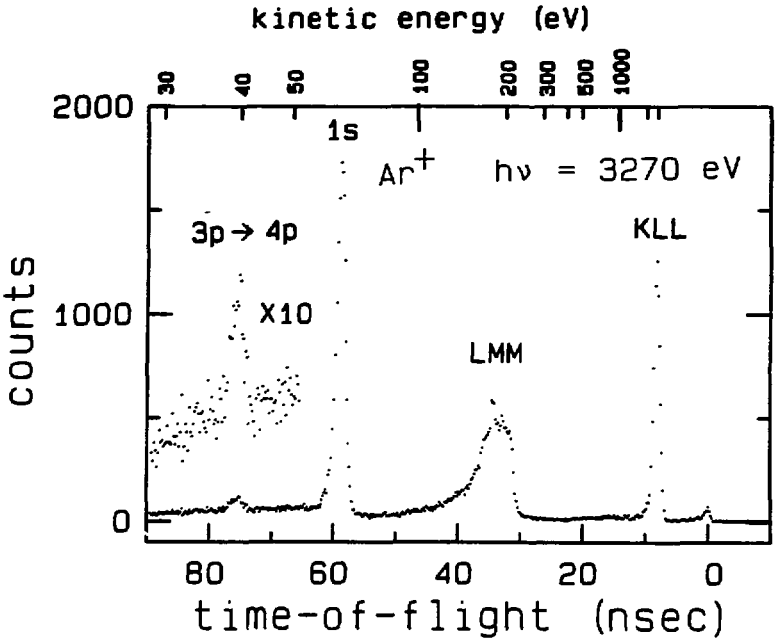

Fig. 4

XBL 8212-12152

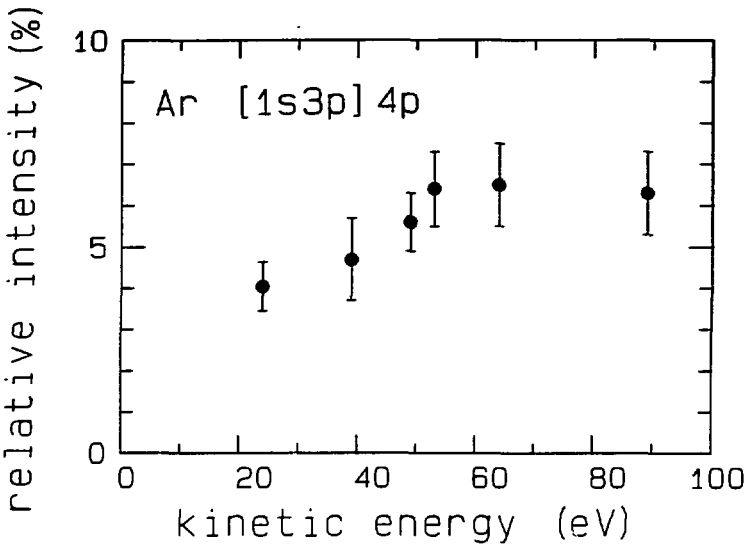
relative intensity (%)
10
5
0
Ar [1s3p] 4p
0
20
40
60
80
100
kinetic energy (eV)
XBL 8212-12154

Fig. 5

VI. RESONANCE PHOTOELECTRON SPECTROSCOPY OF 5p-HOLE STATES IN ATOMIC BARIUM*

ABSTRACT

Photoelectron spectra of atomic barium have been recorded at several photon energies in the range 20 eV $\leq h\nu \leq$ 29 eV. The variations of the $Ba^+ 5p^6nl$ (nl = 6s, 5d, 6p, 7s, and 6d) photoelectron peak intensities were measured in the 20-21 eV autoionization region. The results indicate that each autoionizing state decays to the various states of the ion in a characteristic way. In addition, angular-distribution measurements were performed for the 6s, 5d, and 5p states. Above 21 eV, 5p ionization begins to dominate, and the Auger spectra were used to monitor the production of the various 5p-hole states. As the photon energy is scanned over the autoionizing resonances, these Auger spectra indicate a propensity to produce very low energy photoelectrons ($\leq$2 eV) and the corresponding high-energy Auger electrons from two-step autoionization. Calculations suggest that a heretofore unobserved $5p^5 6p^2\ ^2P_{3/2}$ 5d autoionizing level is responsible for the Auger distribution measured at $h\nu$ = 28.9 eV.

A. INTRODUCTION

The creation and decay of a 5p-hole state in atomic barium has received considerable attention during the past decade. Complex interactions among the various Ba I, Ba II, and Ba III states and their associated continua are involved (see Fig. 1). The complexity is increased by strong mixing of the 6s and 5d levels in this high Z atom. Thus, the barium 5p shell provides a valuable system for studying electron-correlation phenomena. To place the present work in perspective, related work is briefly reviewed in this section.

The predicted 5p → 5d giant resonance[1,2] was found to be spread over many lines because of Ba I final-state mixing.[3,4] The creation of a 5p-hole state in Ba I lowers the energy of the 5d subshell relative to the 6s subshell. The $(5p)^{-1}$ part of the Ba II spectrum has been examined by Ba II absorption[5], Auger spectroscopy,[6-8] He II photoelectron spectroscopy,[9] Penning ionization electron spectroscopy,[10] and He^+ and Ne^+ collision electron spectroscopy.[11] Multiconfigurational Dirac-Fock calculations have been used to assign most of the observed Ba II states.[12]

The distribution of ionic states produced by direct photoionization (process B in Fig. 1) is governed by dipole matrix elements that vary slowly with photon energy. The matrix elements for producing the $5p^6nl$ ($nl \neq 6s$) satellite lines are relatively small, and these lines are weak in the Ne I photoelectron spectrum.[13] Direct photoionization to the 5p-hole states, as in the He II photoelectron spectrum,[9] also involves slowly varying matrix elements, but the intensity is

more evenly distributed among several lines because of strong ionic-state mixing.

Using resonance lamps, it was found that He I radiation at 21.22 eV excited an autoionizing transition which produced both excited Ba II states and an unexpectedly large Ba^{++}/Ba^{+} ratio.[13-16] Explanations of these observations and identification of the Ba I and Ba II states involved have been given.[17-19]

Photoexcitation at 21.22 eV coincides with a highly excited 5p-hole state of neutral Ba (process A in Fig. 1). This state subsequently autoionizes, producing $5p^6nl$ and $5p^5nln'l'$ states of Ba^{+} (e_1 and e_2 in Fig. 1). The distribution among the various $5p^6nl$ states in the Ba^{+} ions is very different from that following direct ionization from the barium ground state. Most of the $5p^5nln'l'$ ions ionize further, producing Auger electrons (e_3 in Fig. 1) and the ground-state Ba^{++} ion. This process has been called "two-step autoionization." The branching ratio of the e_2 to e_1 autoionization channels thus controls the Ba^{++}/Ba^{+} ratio at energies for which direct photoionization is negligible.

Examination of the outgoing channels from photoexcitation with tunable radiation was begun by Rosenberg et al.[20] who measured photoelectron spectra at two autoionizing energies and by Holland and Codling[21] who measured the Ba^{++}/Ba^{+} ratio in the 5p excitation region. Higher resolution Ba^{++}/Ba^{+} measurements have been made more recently.[22,23]

Photoelectron spectroscopy with tunable radiation is capable of providing uniquely definitive information about the photoexcitation and decay of barium. To extend our knowledge of these processes, we have made quantitative measurements of the variation of $5p^6nl$ partial cross sections and photoelectron angular distributions over part of the autoionizing region. We have also measured Auger spectra at several photon energies between 21 and 29 eV, and found that two-step autoionization is frequently responsible for the distribution of observed peaks. In the following section we briefly describe the experimental arrangement, and in section C we present and discuss the results.

B. EXPERIMENTAL

Radiation from SPEAR at the Stanford Synchrotron Radiation Laboratory was monochromatized (2.5Å FWHM) by a Seya-Namioka normal incidence monochromator. An effusive beam of atomic Ba was produced by a non-inductively wound, resistively heated oven.[24-26] The photoelectrons were analyzed by the double-angle time-of-flight (DATOF) method.[27,28]

The spectra reported here were recorded during three widely-separated experimental runs. The monochromator energy calibration may have changed between runs, but this ±1Å uncertainty does not effect any of the conclusions presented below. The time-to-energy converted electron energy scales also differ between runs, but the energies of most of the strong Auger lines are well known, and were used to calibrate the electron energy scales internally.

C. RESULTS AND DISCUSSION

The Ba^{++} threshold energy is at 15.21 eV, but most of the Ba^{++} ions detected below 21 eV are produced by a direct double-ionization process. Above 21 eV, double ionization through Ba^{+} intermediate states becomes dominant. Figure 2 shows a scan of the total electron yield between 596Å and 632Å (19.6 - 20.8 eV). Only electrons with kinetic energies greater than ~4 eV were collected. The photon intensity was not monitored, but changes during this short scan were probably small. In Fig. 2 we also reproduce the relevant portion of the absorption spectrum of Connerade et al.[4] The agreement of the two spectra is very good for some lines, with other lines being absent in the electron yield. Differences in resolution render the comparison difficult in general, but it is straightforward, for example, around 610Å where absorption features are not observed in the total electron yield. This implies that Ba I fluorescence is a competitive process at 610Å. The ionization between 596Å and 632Å is almost entirely due to autoionization (process A then channel e_1 in Fig. 1), with a very small contribution from direct ionization, because of the high density of absorption lines in this region.

Several photoelectron spectra were taken in the energy range of Fig. 2. Almost all of the electron intensity fell in the $5p^6nl$ peaks with nl=6s, 5d, 6p, 7s, and 6d. The partial cross sections for these channels are shown in Fig. 3. The total electron yield from Fig. 2 is reproduced in Fig. 3 for ease of comparison. The total of the five partial cross sections is equal to the total electron yield at each energy.

Inspection of Fig. 3 shows that the autoionizing resonances enhance the five nl states by different amounts. For instance, the largest resonance at 617.8Å, labeled as $(5p^5 6s^2)^2P_{3/2}$ 5d by Connerade et al.,[4] is found predominantly to enhance the $5p^6 6s$ state of the ion. The resonance near 622.9Å, which receives most of its intensity from the $[(5p^5 5d)^3D\ 6s\ ^2D_{3/2}]5d$ state, shows more enhancement of the $5p^6 5d$ channel than of the $5p^6 6s$ channel. At most photon energies the enhancements of the smaller satellite lines (nl = 6p, 7s, and 6d) follow those of the two largest lines (5d and 6s). An exception occurs near 608Å, where the $5p^6 7s$ line alone shows a substantial resonance. This hints at the underlying complexity of the autoionization process in barium and documents the need for photoelectron experiments with higher photon resolution.

In Fig. 4 we show values of the photoelectron angular distribution asymmetry parameter, β, for the 6s, 5d, and 6p states, which were measured simultaneously with the partial cross section data using the DATOF method.[28] These measurements of β over such an unresolved autoionizing region are not amenable to quantitative interpretation. In addition, because they are the first photoelectron angular-distribution measurements from barium, we cannot make any comparisons to off-resonance values. The off-resonance value of β for an s electron from a closed-shell atom would ordinarily be ~2.0.[29] At autoionizing resonances, β will still be ~2.0 if the remaining s electron and the outgoing p-wave are coupled to a singlet. This has been observed at the $3p \rightarrow 3d$ giant resonance in Mn.[30] That we observe β appreciably less

than 2.0 for the 6s state may be due to the triplet nature of most of the autoionizing levels.

We note that a definitive study of β in the autoionization region would require a photon bandwidth much narrower than the resonance lines themselves, as was the case for cadmium.[25] We shall therefore make only one general observation about the β values displayed in Fig. 4. They tend to fall in the order $\beta(6s) > \beta(6p) > \beta(5d)$. In fact, the majority of the β values lie in the ranges $1 < \beta(6s) < 2$, $0 < \beta(6p) < 1$, and $-1 < \beta(5d) < 0$. To the extent that the system passes through the same (oriented) resonant states enroute to the ^2S, ^2P, and ^2D final states in Ba II, it is to be expected that the system will undergo a successively greater decrease in its orientation (and in β) as the final-state (and outgoing electron) angular momentum increases. This is required because

$$\vec{J}_{int} = \vec{J}_f + \vec{J}_e \quad ,$$

where the subscripts denote intermediate-state, final-state, and electron angular momenta, respectively.

Above 21 eV, Auger electrons may be observed following decay of the Ba^+ 5p hole-states, which can be created both by direct ionization (process B in Fig. 1) and by autoionization (process A and e_2). Potts et al.[9] showed that the peak intensity distribution pattern in the He II photoelectron spectrum could be approximately accounted for by final-state configuration-interaction calculations. This shows that

the intensity produced by direct photoionization is a result of mixing with the primary Ba^+ $5p^5 6s^2$ configuration.

Figures 5 and 6 show Auger spectra taken during two separate experiments, with spectra at $h\nu = 23.7$ eV included in both. The spectra in Fig. 6 were taken with a detector at 54.7° relative to the photon polarization direction and are therefore independent of angular distribution effects. Those in Fig. 5 were taken with an analyzer at 0° to the polarization direction. We display the latter spectra because the 0° analyzer provided better resolution than the 54.7° analyzer, and the branching ratios measured by each analyzer were not noticeably different. This implies that the angular distributions of the various Auger peaks are approximately the same. The differences between the two $h\nu = 23.7$ eV spectra are caused by differences in resolution, transmission, and possibly photon energy calibration, as discussed in Sec. II.

Most of the Auger peaks in Figs. 5 and 6 have been observed in electron impact ionization, and their assignments are given in Table I. In the $h\nu = 28.9$ eV spectrum, we apparently also observe the primary photoelectrons at 4.2, 5.4, and 6.2 eV from the three states of Ba^+ that produce the 9.5, 8.3, and 7.5 eV Auger electrons, respectively. The background levels in these spectra are uncertain so that the magnitude of the continuum of electrons from direct Ba^{++} production cannot be ascertained.

As the photon energy is increased in Figs. 5 and 6, new 5p-hole states become energetically accessible and new Auger peaks appear. Many of the Auger peaks become negligibly small at higher energies and are very small in the 500 eV electron impact Auger spectrum.[7] This is the case for most of the peaks observed at photon energies 21.4 and 22.8 eV. The two highest kinetic energy Auger peaks in the 28.9 eV spectrum also appear as small peaks in the 500 eV electron impact spectrum[7] and in the low-energy electron impact spectrum.[8]

The unusually large intensity of the two high kinetic energy Auger peaks in the 28.9 eV spectrum must come from two-step autoionization, however no absorption spectra have been reported in this energy range. The absorption spectrum of Connerade[4] extends in energy only up to 27.5 eV. Therefore, to determine if any absorption features are likely to be found near 28.9 eV, we have performed multiconfigurational Hartree Fock (MCHF) calculations (with a relativistic correction) using the code of Cowan[31] on the Ba^+ $5p^5(6s^2 \times 5d6s \times 5d^2 \times 6p^2)$ manifold. In the J=3/2 manifold, two states of primarily $5p^56p^2$ character were calculated to have binding energies of 31.4 and 31.6 eV and to have 3% admixtures (squared CI coefficient) of the $5p^56s^2$ configuration. In the J=1/2 manifold one state of primarily $5p^56p^2$ character was calculated to have a binding energy of 33.5 eV and to have a 7% admixture of the $5p^56s^2$ configuration. In addition to this final-state mixing with the Ba^+ $5p^56s^2$ configuration, the ground state of barium has been calculated to have 6% $5p^66p^2$ character.[32] This initial-state mixing should provide further intensity to a $5p^56p^2nl$ absorption ser-

ies. The absolute energies of the ionic states were obtained by adjusting the MCHF energies to those from multiconfigurational Dirac-Fock (MCDF) calculations of the $5p^5(6s^2 \times 5d6s \times 5d^2)$ manifold.[12] The spacings of the levels in our J=3/2 MCHF calculation agreed with those from the MCDF calculation to within ~0.3 eV (standard deviation). The first members of the three strong J=3/2 nd series observed by Connerade lie 2.6 ±0.3 eV from their respective limits. Based on these numbers, it is likely that the first members of nd series leading to the 31.4 and 31.6 eV $5p^5 6p^2$ J=3/2 thresholds would lie at 28.8 ±0.4 and 29.0 ±0.4 eV. Thus the spectrum at 28.9 eV with a 2.5Å (=0.17 eV) monochromator bandwidth may overlap an autoionizing resonance, producing Auger electrons by two-step autoionization. This may explain why the two high-energy Auger peaks are observed with such high intensities in the hν = 28.9 eV spectrum.

Photoionization above 21 eV does not always lead to double ionization. Mass spectrometry studies[22] show a Ba^{++}/Ba^{+} ratio that increases at each major threshold. In addition to this increase there is considerable structure. This structure appears because the discrete autoionizing resonances each have different decay characteristics. Some decay predominantly to $5p^6nl$ states of Ba^{+} while others decay by two-step autoionization to Ba^{++}.

Using the 54.7° spectra obtained at the photon energies in Fig. 5, we have compared the total intensity of the $5p^6nl$ peaks from Ba^{+} to the total intensity of the Auger peaks from Ba^{++}. Our Ba^{++}/Ba^{+} ratios are listed in Table II along with the He I ratio and the mass spectrometry values. Although our ratios are accurate only to within a

factor of two because of uncertainties in the analyzer transmission, better measurements of this type could provide information about the Ba^{++}/Ba^{+} ratio not obtainable by other means. If the Ba^{++}/Ba^{+} ratio from the photoelectron spectrum could be determined accurately enough, it would be possible to obtain, by difference, the amount of Ba^{++} that is directly formed through the emission of two electrons. These electrons should have a continuum of energies and thus would not appear as peaks in the photoelectron spectrum.

In assuming that each 5p-hole state Auger decays to Ba^{++}, we have assumed that deexcitation by fluorescence in Ba^{+} is negligible by comparison. This assumption is supported by the Auger and x-ray emission calculations of Chen and Crasemann.[33] These calculations were done with non-relativistic Hartree Fock wavefunctions and included the effects of initial-state configuration interaction.

Regarding the Ba^{++}/Ba^{+} ratio, Connerade et al.[34] have proposed that the two channels leading to production of Ba^{+} states, direct photoionization and autoionization, may show an interference effect. The possibility of interference exists for both the $5p^{6}nl$ states and the $5p^{5}nln'l'$ states. This interference could produce asymmetric autoionizing lineshapes in the absorption and partial cross section spectra as well as in the Ba^{+} and Ba^{++} yield spectra. We note, however, that no asymmetric peaks are observed in the high resolution absorption spectrum[4] or in the high resolution Ba^{++} yield spectrum.[23] Therefore any apparently asymmetric features in the low resolution Ba^{++}/Ba^{+} spectrum must result from the superposition of unresolved features.

REFERENCES

*Work done in collaboration with R.A. Rosenberg, U. Becker, S. Southworth, C.M. Truesdale, D.W. Lindle, G. Thornton, M.G. White, E. D. Poliakoff, and D.A. Shirley.

1. U. Fano, Comm. At. Mol. Phys. 4, 119 (1973).
2. G. Wendin, Vacuum UV Radiation Physics ed. E.E. Koch et al. (Braunschweig: Pergamon) 1974, pp 235.
3. D.L. Ederer, T.B. Lucatorto, and E.B. Saloman, Vacuum UV Radiation Physics ed. E.E. Koch et al. (Braunschweig: Pergamon) 1974, pp 245.
4. J.P. Connerade, M.W.D. Mansfield, G.H. Newsom, D.H. Tracy, M.A. Baig, and K. Thimm, Phil. Trans. R. Soc. A 290, 327 (1979).
5. R.A. Roig, J. Opt. Soc. Am. 66, 1400 (1976).
6. W. Mehlhorn, B. Breuckmann, and D Hausamann, Phys. Scr. 16, 177 (1977).
7. D. Rassi and K.J. Ross, J. Phys. B 13, 4683 (1980).
8. R.A. Rosenberg, S.T. Lee, and D.A. Shirley, Phys. Rev. A 21, 132 (1980).
9. A.W. Potts and E.P.F. Lee, J. Phys. B 12, L413 (1979).
10. K. Gerard, H. Hotop, and D. Mahr, Adv. Mass Spec. A7, 192 (1977).
11. W. Hultzsch, W. Kronast, A. Niehaus, and M.W. Ruf, J. Phys. B 12, 1821 (1979).
12. S.J. Rose, I.P. Grant, and J.P. Connerade, Phil. Trans. R. Soc. Lond. A 296, 527 (1980).

13. S.T. Lee, S. Süzer, E. Matthias, R.A. Rosenberg, and D.A. Shirley, J. Chem. Phys. 66, 2496 (1977).

14. B. Brehm and A. Bucher, Int. J. Mass Spec. Ion Phys. 15, 463 (1974).

15. B. Brehm and K. Höfler, Int. J. Mass Spec. Ion Phys. 17, 463 (1975).

16. H. Hotop and D. Mahr, J. Phys. B 8, L301 (1975).

17. J.E. Hansen, J. Phys. B 8, L403 (1975).

18. G. Wendin, "Photoionization of Atoms and Molecules," Proceedings of the Daresbury One-Day Meeting, 16 Feb. 1978 (unpublished).

19. J.P. Connerade, S.J. Rose, and I.P. Grant, J. Phys. B 12, L53 (1979).

20. R.A. Rosenberg, M.G. White, G. Thornton, and D.A. Shirley, Phys. Rev. Lett. 43, 1384 (1979).

21. D.M.P. Holland and K. Codling, J. Phys. B 13, L293 (1980).

22. D.M.P. Holland, K. Codling, and R.N. Chamberlain, J. Phys. B 14, 839 (1981).

23. B. Lewandowski, J. Ganz, H. Hotop, and M.W. Ruf, J. Phys. B 14, L803 (1981).

24. R.A. Rosenberg, Ph.D. Thesis, University of California (1979 unpublished).

25. P.H. Kobrin, U. Becker, S. Southworth, C.M. Truesdale, D.W. Lindle, and D.A. Shirley, Phys. Rev. A 26, 842 (1982); and Chapt. III.

26. Chapt. II.

27. M.G. White, R.A. Rosenberg, G. Gabor, E.D. Poliakoff, G. Thornton, S.H. Southworth, and D.A. Shirley, Rev. Sci. Instrum. 50, 1263 (1979).

28. S. Southworth, C.M. Truesdale, P.H. Kobrin, D.W. Lindle, W.D. Brewer, and D.A. Shirley, Phys. Rev. A 26, 842 (1982).

29. T.E.H. Walker and J.T. Waber, J. Phys. B 6, 1165 (1973).

30. P.H. Kobrin, U. Becker, C.M. Truesdale, D.W. Lindle, H.G. Kerkhoff, and D.A. Shirley (to be published); and Chapt. VII.

31. R.D. Cowan and J.B. Mann, J. Comput. Phys. 16, 160 (1974).

32. S.J. Rose, N.C. Pyper, and I.P. Grant, J. Phys. B 11, 755 (1978).

33. M.H. Chen and B. Crasemann (private communication).

34. J.P. Connerade and M.A.P. Martin, J. Phys. B 13, L373 (1980).

Table I. Kinetic Energies in eV for Observed Auger Lines

Line No.[a]	Kinetic Energy[a]
1	5.80
2	5.85
3	5.93
4, 5	6.09, 6.10
7	6.43
8	6.57
9 or 10	6.76 or 6.81
12	7.06
13	7.29
14, 15	7.48, 7.58
16	8.31
22	9.55
29	12.00[b]
34	13.54[b]

[a]From Rosenberg et al.[8]

[b]In the MCDF Mn II calculations of Rose et al.[12] the 10th and 12th levels in the J=1/2 manifold include 13% and 3% admixtures of the $5p^5 6s^2$ configuration and have calculated Auger energies of 12.0 and 13.5 eV, respectively.

Table II. Ba^{++}/Ba^{+} Ratios

hν	PES	Mass Spectroscopy	
		Holland[c]	Lewandowski[d]
21.22	0.65[a]	1.05	0.7
21.4	0.3 - 0.65[b]	1.0	0.7
22.8	3.4 - 5.6[b]	3.5	1.9
23.7	7.8 - 11.7[b]	6.5	

[a]From Lee et al.[13]

[b]This work. A correction has been made for the analyzer transmission. The uncertainty in this correction is responsible for the uncertainty in these ratio.

[c]From Holland et al.[22] with a 2.0Å bandwidth. Note that Lewandowski et al.[23] state that the monochromator calibration in the work of Holland et al. may be off by 2Å.

[d]From Lewandowski et al.[23] with a 0.9Å bandwidth.

FIGURE CAPTIONS

Fig. 1 Energy-level diagram for barium, including the various excitation and decay channels.

Fig. 2 The total electron yield spectrum from this work and the absorption spectrum of Connerade et al. (1979a). The ordinate scale refers to the yield spectrum only. The absorption spectrum is plotted on an arbitrary scale.

Fig. 3 The partial cross sections of the $Ba^+ 5p^5nl$ states where (nl = 6s, 5d, 6p, 7s, and 6d). The bottom panel shows the total electron yield as in Fig. 2. The units of the ordinate scales are the same, but arbitrary.

Fig. 4 The angular distribution asymmetry parameter, β, of the 6s, 5d and 6p photoelectrons. The error bars represent counting statistics only. The solid curve is the total electron yield, shown for comparison.

Fig. 5 Electron kinetic-energy spectra at three different photon energies, showing the Auger peak intensities. The peaks at kinetic energies above 6.6 eV in the $h\nu$ = 21.4 eV spectrum and at kinetic energies above 7.6 eV in the $h\nu$ = 22.8 eV spectrum are from $Ba^+ 5p^6nl$ photoelectrons, not Auger electrons.

Fig. 6 Electron kinetic energy spectra at three photon energies showing Auger peak intensities. Primary photoelectrons peaks are also observed in the $h\nu$ = 28.9 eV spectrum, as discussed in the text.

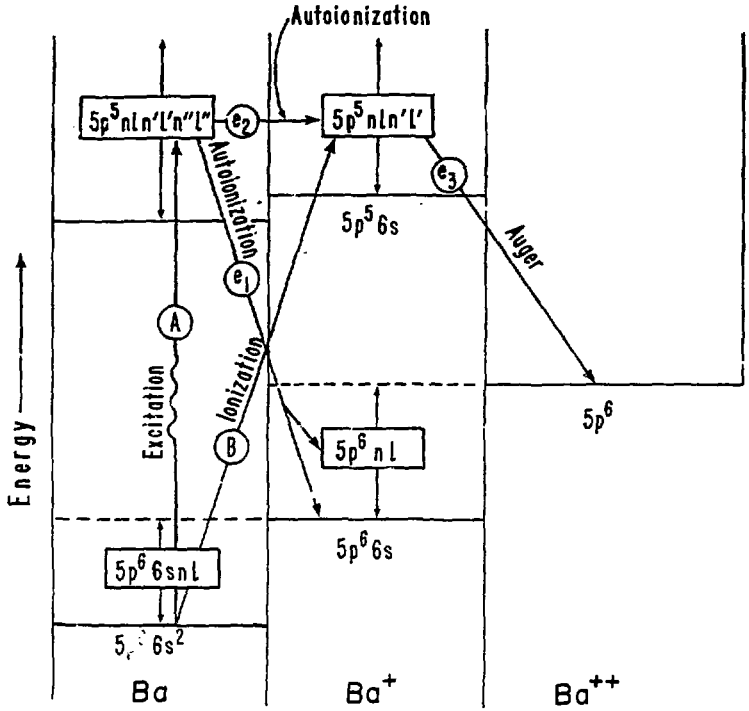

XBL 794-1342A

Fig. 1

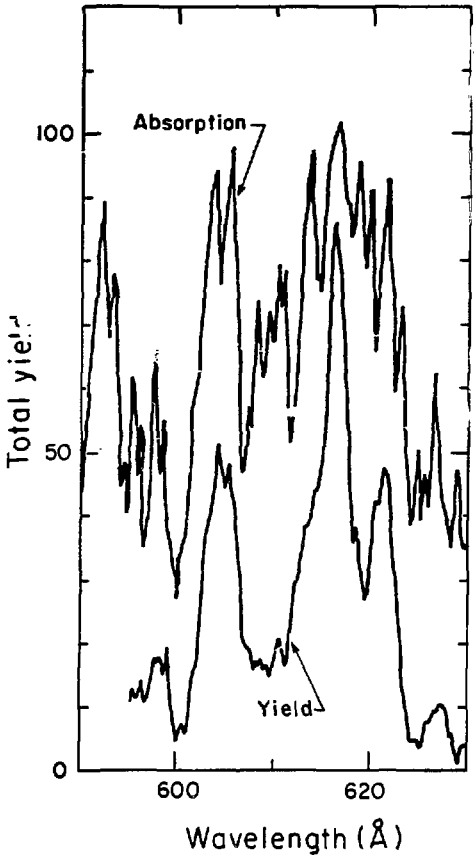

Fig. 2

XBL 8211 – 7354

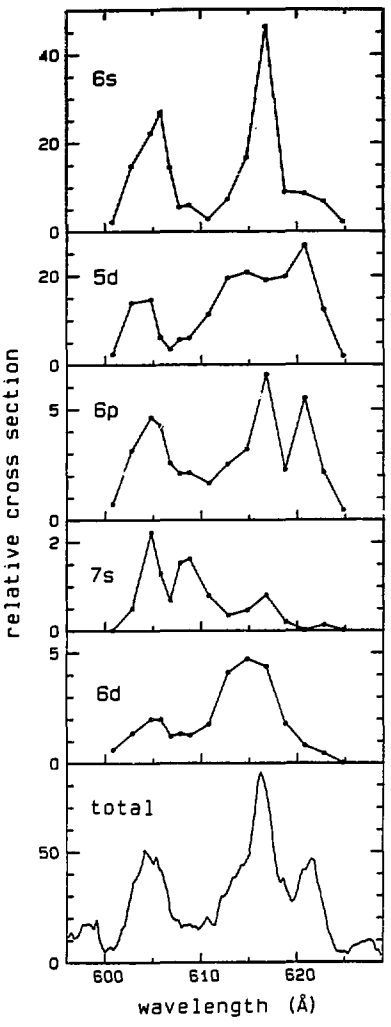
6s
5d
6p
7s
6d
total
relative cross section
wavelength (Å)
600
610
620
XBL 832-7845

Fig. 3

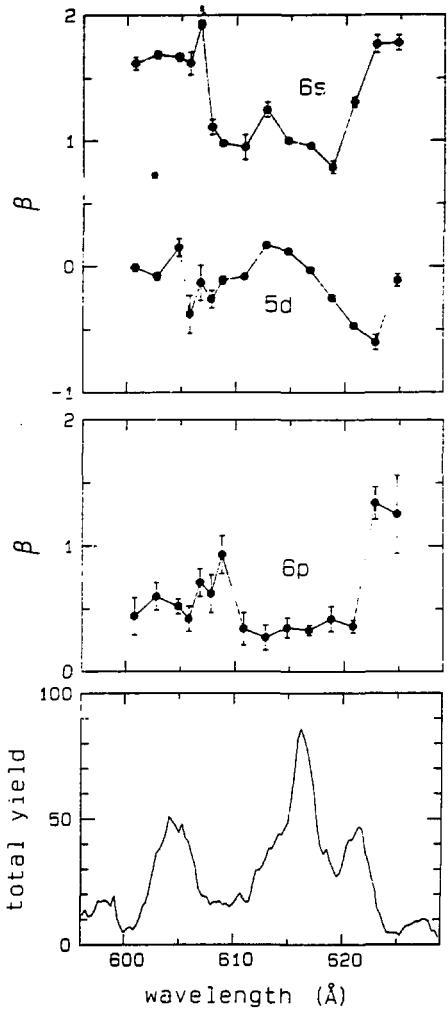

XBL 832-7844

Fig. 4

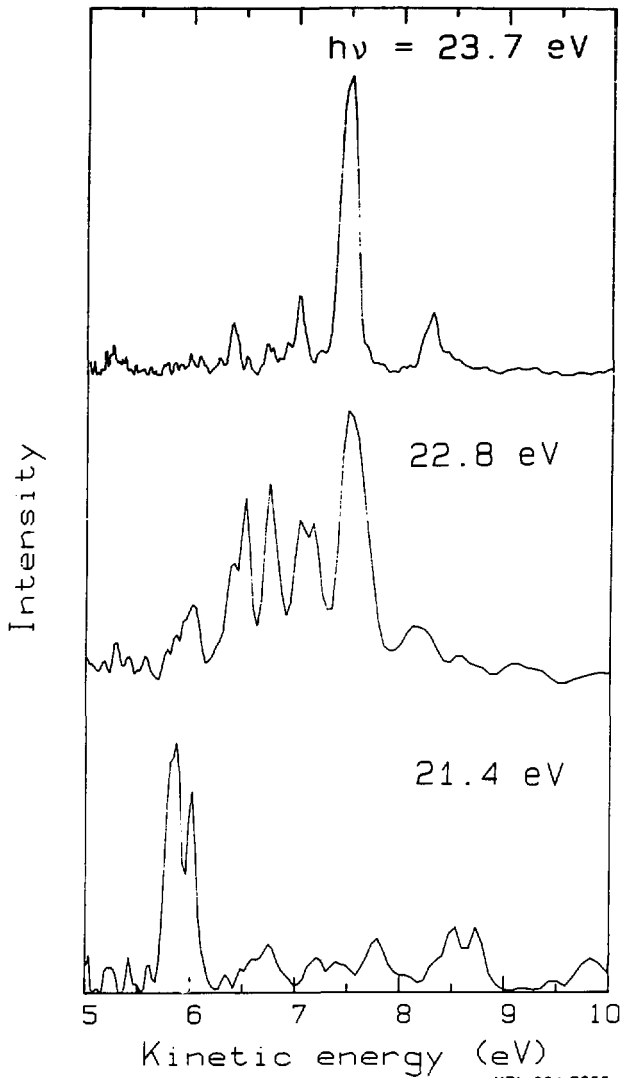
hν = 23.7 eV
22.8 eV
21.4 eV
Intensity
5
6
7
8
9
10
Kinetic energy (eV)
XBL 831-7655

Fig. 5

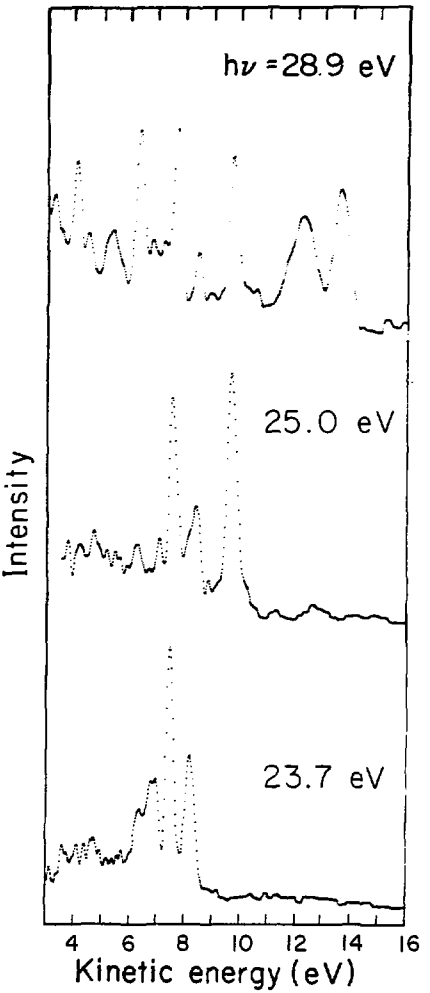

Fig. 6

XBL 797-2304B

VII. PHOTOELECTRON ASYMMETRIES AND TWO-ELECTRON SATELLITES NEAR THE 3p THRESHOLD IN ATOMIC MANGANESE*

ABSTRACT

The partial cross sections and photoelectron angular distributions for several lines in atomic Mn have been measured at photon energies between 50 and 72 eV. The intensities of the 3d correlation satellites at 24–26 eV binding energy behave similarly to the main line near the 3p → 3d giant resonance, but show an enhancement near the 3p threshold which is not present in the main line. A configuration interaction analysis is applied to help identify the origins of the satellites.

A. INTRODUCTION

The 3p absorption spectrum of Mn I was first observed by Connerade, Mansfield and Martin,[1] who found it to be dominated by a strong, broad asymmetric resonance at ~50 eV. They also reported discrete features below and above the largest resonance as well as a broad modulation in the continuum absorption immediately above the 3p-threshold. The "giant resonance" is attributed to transitions from the ground state $3p^6 3d^5 4s^2\ ^6S$ to the dipole-allowed states $3p^5(3d^6\ ^5D)4s^2\ ^6P_{3/2,5/2,7/2}$. The shape and width of the resonance were explained by the mixing of the ^6P resonance with the $3p^6 3d^4 4s^2 \varepsilon f\ ^6P$ continuum. Using Hartree-Fock calculations, the lower energy features were identified as $3p^5 3d^6 4s^2\ ^6F$ and ^6D and the higher energy features as $3p^5(3d^5\ ^6S)4s^2\ ^7P$ nl (nl = 4d, 5s, and 5d). The broad peak between 55 and 58 eV was identified as the maximum in the $3p^5(3d^5\ ^6S)4s^2\ ^7P$ εs, εd continua.

Davis and Feldkamp[2] applied Fano's theory[3] of the interaction of discrete and continuum states and single-configuration Hartree-Fock calculations to model the absorption spectrum. They confirmed that super-Coster-Kronig decay from the ^6P state to the $(3d)^{-1}$ continuum was responsible for the shape and width of the ^6P resonance. A higher quality absorption spectrum[4] and a many-body random phase approximation with exchange (RPAE) calculation[5] provided further confirmation of the earlier analysis.

With resonant photoemission, it is possible to study some of the underlying details of photoabsorption. In this type of experiment, the total cross section observed in absorption is separated into the partial cross sections for production of the different final ionic

states by analyzing the energy distribution of the emitted photoelectrons.

In this paper we report the photon energy dependence of the partial cross sections and the angular distributions for the main lines and several satellite peaks in the photoelectron spectrum of Mn. An analysis is made of the intensities of the satellite lines based on Hartree-Fock configuration-interaction (HF-CI) calculations. Of particular interest is the enhancement of the satellite intensities relative to the main 3d line near the 3p threshold at ~55 eV.

The experiment is described in Sec. B, and the results of our measurements are presented in Sec. C. Section D contains the CI analysis of the satellites, and our conclusions are summarized in Sec. E.

B. EXPERIMENTAL

The experiment was performed at the Stanford Synchrotron Radiation Laboratory using a grazing-incidence grasshopper monochromator with a 1200 lines/mm holographically ruled grating. The monochromator cannot be used for energies less than 50 eV with this grating. The other available grating (300 lines/mm, interchangeable in vacuum) was usable down to 12.5 eV, but was far less efficient. Therefore, all of the spectra were taken above 50 eV. The bandpass of the monochromator was less than 0.5 eV for the spectra taken between 50 and 72 eV. A nickel grid and channeltron were used to monitor the photon intensity.

Manganese was vaporized from a resistively-heated oven similar to the one used earlier.[6] It was modified in order to reach higher temperatures, and an unheated skimmer was added to minimize the possibility of Mn coating the electron analyzers. Details of the oven will be given elsewhere.[7]

Spectra were taken using the double-angle time-of-flight (DATOF) method described earlier.[6,8] In brief, electrons are energy dispersed by their flight times through a 28 cm drift tube. Analyzers placed at 0° and 54.7° with respect to the polarization of the synchrotron radiation are used. Peak areas from the 54.7° ("magic-angle") detector are directly proportional to the photoelectron cross sections. The ratio of peak areas from the two detectors provides the angular distribution asymmetry parameter, β, which completely describes the spatial distribution of the photoelectrons.

The energy calibration of the analyzers was accomplished by measuring the time-of-flight of the 2s and 2p lines in neon. This also allowed for the simultaneous determination of the energy dependence of the relative transmission of each analyzer, which are used in correcting the cross-section and angular-distribution measurements

C. MEASUREMENTS

Figure 1 shows a TOF spectrum of Mn taken at $h\nu$ = 50 eV with the 54.7° analyzer. At this energy, which lies near the maximum of the giant-resonance absorption, we observe photoelectron peaks with binding energies both below and above the main 3d line at 14.3 eV. The lines with lower binding energy are very weak except near the giant

resonance, while those with higher binding energy are present in all the spectra up to hν = 72 eV and can still be seen (as an unresolved peak) at hν = 140 eV. The resonantly produced lines with lower binding energies are assigned as 4s peaks belonging to different couplings of the ionic configuration $3d^5 4s$. We shall refer to the group of peaks with binding energy near 21 eV as 3d* and those with binding energy near 25 eV as 3d**. Unfortunately, the Ne 2p photoelectron peak (binding energy = 21.6 eV) from residual calibration gas overlaps the 3d* satellites in most of our spectra.

The TOF analyzer resolution is ~3% of the electron energy, so most of the peaks in our spectra have widths of 0.7 to 1.7 eV FWHM. Peak positions are difficult to determine due to detector resolution and time-to-energy conversion uncertainties. Coincidental with this work, Bruhn et al.[9] have taken photoelectron spectra over the giant-resonance region and have fitted energy profiles to the partial cross sections of the main lines. In addition, Süzer[10] has observed four peaks with binding energies greater than 20 eV in a spectrum taken at the He II resonance line energy of 40.8 eV. The energy positions of the peaks observed with binding energies greater than 20 eV are listed in Table I. The assignments of these peaks will be discussed in Section IV.

In Fig. 2 we have plotted the partial cross sections of the 3d and the sum of the 4s peaks from our measurements together with the data of Bruhn et al.[9] Points taken off resonance were used to scale the two sets of data. Both the absorption spectrum[4], which shows a maximum split into two peaks, and the semiempirical calculation,[2]

which shows a low-energy shoulder, lead us to believe that the 3d partial cross section profile results from at least two overlapping resonances. Indeed, we find that a fit of the 3d partial cross-section data to two overlapping resonances[11] (solid curve in Fig. 2) gives much better agreement than the fit to a single resonance.[9] By separating the two overlapping resonances in our fit by 0.43 eV, which corresponds to the separation of the two maxima in the absorption spectrum,[4] we find an "effective q" of 2.4 for the larger component. Calculations using many-body perturbation theory (MBPT) suggest that the giant resonance is actually formed by a large number of overlapping resonances.[12] The 4s partial cross-section data can be equally well fitted by a single or an overlapping pair of nearly Lorentzian resonances.

We note that there is no evidence in the 3d partial cross-section data of the double-excitation absorption features between 54 and 56 eV or of the small maximum in absorption between 55 and 58 eV. A plot of the cross section of the 3d** lines shows a maximum near 50 eV similar to the main 3d line and an overall decrease out to 72 eV. To look for more subtle differences, we show in Fig. 3(a) the branching ratio of this group of satellites to the 3d line. Because the intensities of different peaks are measured simultaneously using the TOF method, these branching ratios are independent of the corrections in photon flux and vapor pressure that were necessary to produce Fig. 2. Thus they are intrinsically more accurate than partial cross sections. The branching ratio varies little between 50 and 54 eV, while the 3d line is changing by a factor of 3, demonstrating the similarity of the res-

onance behavior of the 3d** satellite lines and of the 3d main line. Between 54 and 55 eV, the branching ratio shows a sharp two-fold increase while the 3d-line intensity remains nearly constant. This sudden increase in the relative satellite intensity occurs at the same energy that the 3p Auger line first appears in our spectra. Because the 3p electrons are difficult to detect near threshold and because there should be an Auger electron for each 3p hole created, we have used the Auger electrons to monitor the 3p cross section. In Fig. 3(b), is plotted the branching ratio of the Auger line relative to the main 3d line. Also plotted in Fig. 3(b) is a MBPT curve of the 3p/3d branching ratio calculated by Garvin et al[12] which is in good agreement with these measurements.

The resonance behavior of the asymmetry parameter provides information about the structure of the resonance states and their decay characteristics.[6] The asymmetry parameter of the 3d peak for $50 \leq h\nu \leq 72$ eV is shown in Fig. 4. It is approximately 0.65 over this energy range except where it rises to 0.9 at the giant resonance. From the results of MBPT calculations on the separate εp and εf continuum channels,[12] we expect a pronounced change in β to occur below 50 eV where the εf cross section is going through a minimum. Recent measurements by Krause and Carlson[13] show a large decrease in β below 50 eV and good agreement with our measurements above 50 eV.

For the weak 3d** peaks, the β values show too much scatter to derive reliable values, but β tends to be below one.

The resonantly produced 4s satellites have a β value of 2.0(2). To obtain $\beta < 2$ would require large spin-orbit interactions in the discrete resonance state or in the continuum channels. Provided that the remaining s electron and the outgoing p-wave are coupled to a singlet, with very little triplet mixing, we would expect $\beta = 2$, showing that parity favored transitions are dominant.[14]

D. CALCULATIONS

In order to identify the peaks with binding energies greater than 20 eV, we have performed Hartree-Fock (HF) calculations on the Mn II ion. These calculations were done with the HF code of Froese-Fischer,[15] as modified by Cowan.[16] All energies have been referenced to the binding energy of the $3d^4 4s^2\ ^5D$ state (14.26 eV).[17] From comparisons with observed states of lower binding energy, we expect these calculated energies to be accurate to within ~0.3 eV.

With up to three open subshells for some configurations, the number of possible states in Mn II is quite large. In order to limit these, we examined the "spectator model" for the 3d electrons. With all of the ionic states under consideration having four 3d electrons, the spectator model assumes that the 3d electrons will remain coupled as ^5D. Table II lists the HF energies of the possible $3d^4 4s^2$ states. There is evidence in this work and in Ref. 9 for peaks between 15 and 20 eV binding energy near the "giant resonance", but their intensities are very small above 53 eV photon energy. Thus, the spectator model

appears to be valid. Therefore the remaining calculations were limited to states with a $3d^4\ ^5D$ subshell.

We then calculated energies for the states $(3d^4\ ^5D)nln'l'$ $(n,n' \leq 5)$. A further limitation of the number of states was achieved by selecting even parity states which are coupled to a ^5D term and odd parity states in which the outer two electrons are spin-coupled to a singlet. The binding energies of these levels are listed in Table III. The separation into groups of odd and even parity is important when we consider the mechanisms of production of satellite peaks.

The first group of satellites, 3d*, lies at an energy that fits the assignments $(3d^4\ ^5D)(4s4p\ ^1P)\ ^5P$ and ^5F. These two states are listed in the tables of Corliss and Sugar[17] with binding energies of 20.6 and 20.7 eV, respectively. These authors list observed states up to the threshold for production of Mn III at 23.1 eV and therefore do not include any of the higher binding energy states in Table III.

Because of the uncertainties in the calculations, the satellites cannot be unequivocally assigned based on energy alone. We therefore consider the mechanisms for producing photoelectron satellite lines.

It is useful to classify photoelectron satellites, which are caused by a breakdown of the one-electron model, into three types: initial-state configuration interaction (ISCI), final-ionic-state configuration interaction (FISCI), and continuum-state configuration interaction (CSCI).[18] These are not mutually exclusive classifications, and a given satellite may have contributions from more than one type. It is possible to look for the ISCI and FISCI contributions by doing configuration interaction (CI) calculations on the Mn I and Mn

II states. HF-CI calculations were performed with the inclusion of the main $3d^4 4s^2\ ^5D$ state and all of the even configurations listed in Table III. We have also done ISCI calculations with inclusion of the $3d^5 4s^2\ ^6S$ ground state and the $3d^5 4s4d$, $3d^5 4s5s$ and $3d^5 4p^2$ configurations. The only appreciable mixing in these calculations ($\geq$0.1%) was with the $3d^5 4p^2\ ^6S$ neutral state (5%) and with the $3d^4 4p^2\ ^5D$ ionic state (1%). We would therefore expect a $3d^4 4p^2\ ^5D$ photoelectron peak with an intensity on the order of 5% of the main $3d^4 4s^2\ ^5D$ line. This would account for one of the 3d** peaks, except that the calculated energy is at least 0.6 eV too high.

None of the odd parity states in Table III can mix with the even parity $3d^4 4s^2\ ^5D$ state, nor can their corresponding odd parity neutral states mix with the even parity ground state $3d^5 4s^2\ ^6S$. Production of such a satellite must therefore occur in the continuum state while the ejected electron is still present (CSCI).

Such continuum effects are more difficult to calculate. One example of such a calculation is by Davis and Feldkamp.[19] They estimated the intensity of the $3d^9 4p$ satellite relative to the $3d^9 4s$ main line in Cu^+. They refer to this continuum state mixing as inelastic scattering. It has also been described as "conjugate shakeup". In the Davis-Feldkamp picture, the outgoing electron inelastically scatters off the ion from which it is being ejected:

$$Cu^+: \quad 3d^9 4s\varepsilon f + 3d^9 4p\varepsilon' d + 3d^9 4p\varepsilon' g \quad . \qquad (1)$$

Davis and Feldkamp modeled this process, using Hartree-Slater wavefunctions, and found that the $3d^9 4p$ intensity is 6% of the intensity of the $3d^9 4s$ main line.

The $3d^4 4s4p$ and $3d^4 4s5p$ states in Mn^+ could be produced by a process analogous to Eq. (1). To calculate the inelastic scattering intensity, it is necessary to evaluate a complex, two-electron integral involving the continuum electrons (R^1 (εf, 4s; $\varepsilon' d$, 4p) in Ref. 19). By evaluating only the imaginary part of R^1, which involves real wavefunctions only, we obtain a lower bound to the inelastic scattering intensity. Using this approximation, we calculated the imaginary parts of R^1 for the production of the $3d^9 4p$ state in Cu^+ and the $3d^4 4s4p$ and $3d^4 4s5p$ states in Mn^+ using Cowan's Hartree-plus-statistical exchange (HX) code.[20] This code has a different approximate exchange term than Hartree-Slater. Our results are presented in Table IV.

We have no explanation for the differences between our HX results for Cu^+ and the HS results from Ref. 19. The total inelastic peak intensity is proportional to the sum of the squares of the εd and εf terms in Table IV plus the sum of the squares of the real parts. All of the factors involving the spin and angular momentum quantum numbers are the same for Cu^+ and Mn^+. The values in Table IV show that we may expect that the $3d^4 4s4p$ satellite in Mn^+ to be about the same intensity as the $3d^9 4p$ state in Cu^+ (~6%), while the $3d^4 4s5p$ satellite should be an order of magnitude smaller.

We assign the 3d satellites as follows:

1. The assignment of 3d* is $(3d^4\ ^5D)(4s4p\ ^1P)^5P$ and ^5F. This result is based on both the peak position and the inelastic scattering intensity. No other states are in thi energy range except for the $3d^44s^2\ ^3F$, which would require a breakdown of the spectator model.
2. The only assignment which produces appreciable intensity near the 3d** energy is the ISCI-FISCI produced $(3d^4\ ^5D)4p^2\ ^5D$, which is calculated to lie 1.1 eV higher than any peak in Ref. 9 and 0.6 eV higher than any peak in Ref. 10. Based on energy alone, there are several other possibilities for the two 3d** peaks.

E. CONCLUSIONS

The partial cross sections of the 3p and 4s main lines and of the 24–26 eV binding energy two-electron satellites are all enhanced at the 3p → 3d giant resonance near $h\nu$ = 55 eV. The 3p/3d branching ratio from $h\nu$ = 55–72 eV is reported and is in good agreement with MBPT calculations.

The off-resonant photoelectron spectrum of manganese includes two-electron satellites of the $3d^44s^2\ ^5D$ main line. The lines at 20.7 and 20.8 eV binding energy have been identified as $(3d^4\ ^5D)\ (4s4p\ ^1P)\ ^5P$ and ^5F, and their intensity has been partially attributed to inelastic scattering off the primary ion. Several possible lines have been discussed in conjunction with the satellites near 25 eV binding energy, but no definitive assignments have been made.

REFERENCES

*Work done in collaboration with U. Becker, C.M. Truesdale, D.W. Lindle, H.G. Kerkhoff and D.A. Shirley.

1. J.P. Connerade, M.W.D. Mansfield and M.A.P. Martin, Proc. R. Soc. Lond. A 350, 405 (1976).
2. L.C. Davis and L.A. Feldkamp, Phys. Rev. A 17, 2012 (1978).
3. U. Fano, Phys. Rev. 124, 1866 (1961).
4. R. Bruhn, B. Sonntag and H.W. Wolff, Phys. Lett. 69A, 9 (1978).
5. M. Ya Amusia, V.K. Ivanov and L.V. Chernysheva, J. Phys. B 14, L19 (1981).
6. P.H. Kobrin, U. Becker, S. Southworth, C.M. Truesdale, D.W. Lindle, and D.A. Shirley, Phys. Rev. A. 6, 842 (1982); and Chapt. III.
7. Chapt. II.
8. S. Southworth, C.M. Truesdale, P.H. Kobrin, D.W. Lindle, W.D. Brewer, and D.A. Shirley, J. Chem. Phys. 76, 143 (1982).
9. R. Bruhn, E. Schmidt, H. Schröder, and B. Sonntag, Physics Lett. A 90, 41 (1982).
10. S. Süzer, private communication.
11. B.W. Shore, Phys. Rev. 171, 43 (1968).
12. L. Garvin, E. Brown, S.L. Carter and H.P. Kelly (to be published).
13. M.O. Krause and T.A. Carlson, private communication.
14. D. Dill, Phys. Rev. A 7, 1976 (1973).
15. C. Froese-Fischer, Comp. Phys. Commun. 1, 151, (1969).
16. R.D. Cowan and J.B. Mann, Jr., J. Comput. Phys. 16, 160 (1974).
17. C. Corliss and J. Sugar, J. Phys. Chem. Ref. Data, 6, 1253 (1977).

18. S.T. Manson, J. El. Spec. 9, 21 (1976).

19. L.C. Davis and L.A. Feldkamp, Phys. Rev. A 24, 1862 (1981).

20. R.D. Cowan, Phys. Rev. 163, 54 (1967).

Table I. Binding energies of observed 3d satellites.

Line	This Work	Ref. 9[a]	Ref. 10[b]	intensity[c]
3d*	....	20.6(2)	20.7	8
		20.8(2)		
3d**	24.5	24.2(2)	24.3	7
	25.5	25.0(2)	25.2	15
			25.5	7

[a] $h\nu$ = 50.0 eV.

[b] $h\nu$ = 40.8 eV.

[c] $h\nu$ = 40.8 eV, Ref. 10. Intensities relative to the 3d main line (= 100).

Table II. Calculated binding energies of $3d^4 4s^2$ states.[a]

State	Binding Energy (eV)
^5D	14.3
$^3F(1)$	17.0
^3G	17.3
^3D	18.1
^1F	19.7
$^3F(2)$	20.7

[a]Relative to ^5D energy.[17]

Table III. Calculated binding energies of $(3d^4\ {}^5D)nln'l$ states.[a]

Parity	nln'l'	Binding Energy (eV)
even	4s4d	24.4, 25.4
even	4s5s	23.6, 24.5
even	$4p^2$	26.1
odd	4s4p	20.7, 20.8
odd	4s5p	25.0, 25.1
odd	4s4f	25.5–27

[a]Additional criteria for selection of states are given in text.

Table IV. Imaginary part of two-electron integral R^1.

			This Work	Davis and Feldkamp[20]
Cu^+ $3d^9 4s\varepsilon f$	→	$3d^9 4p\varepsilon d$	0.165	0.080
	→	$3d^9 4p\varepsilon g$	-0.020	0.021
Mn^+ $3d^4 4s^2 \varepsilon f$	→	$3d^4 4s4p\varepsilon d$	0.21	
	→	$3d^4 4s4p\varepsilon g$	0.03	
	→	$3d^4 4s5p\varepsilon d$	0.05	
	→	$3d^4 4s5p\varepsilon g$	-0.01	

FIGURE CAPTIONS

Fig. 1 Photoelectron spectrum of Mn vapor taken at $h\nu \approx 50$ eV taken with the 54.7° detector.

Fig. 2 Partial cross sections of the 3d and 4s main lines from this work (filled symbols) and from Bruhn et al.[9] (open symbols). The solid curves are fits to two overlapping resonances.

Fig. 3 The branching ratios of the (a) 3d** and (b) 3p Auger lines to the 3d main line. The solid curve in panel (b) is from the MBPT calculation of Garvin et al.[12]

Fig. 4 The photoelectron angular distribution asymmetry parameter of the 3d main line.

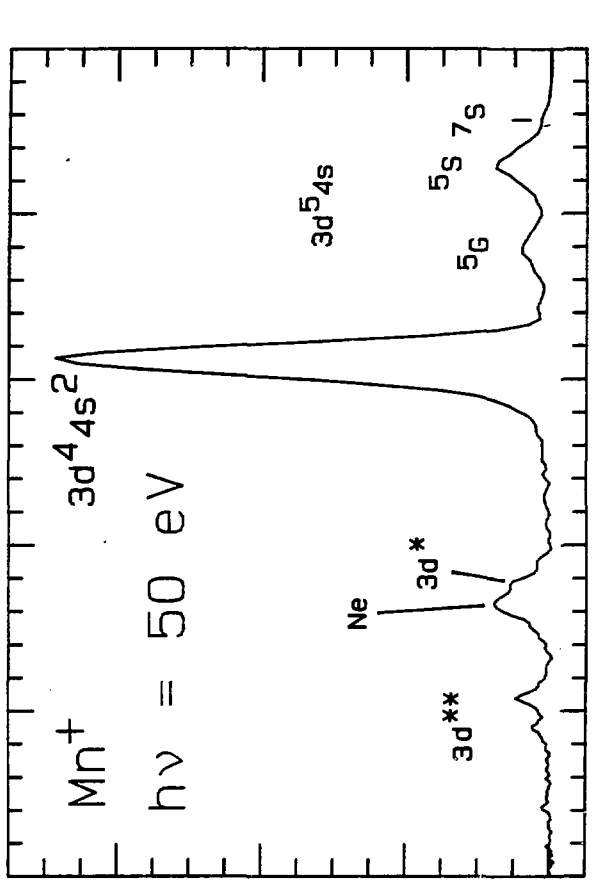

XBL 832-7859

Fig. 1

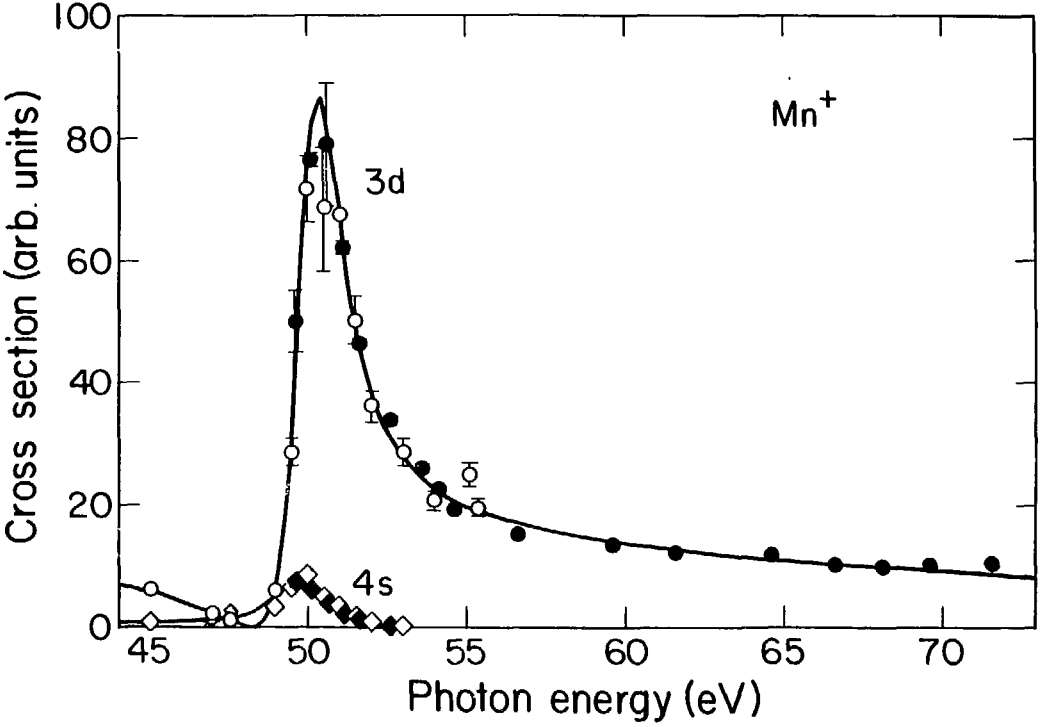

Fig. 2

XBL 832-1221

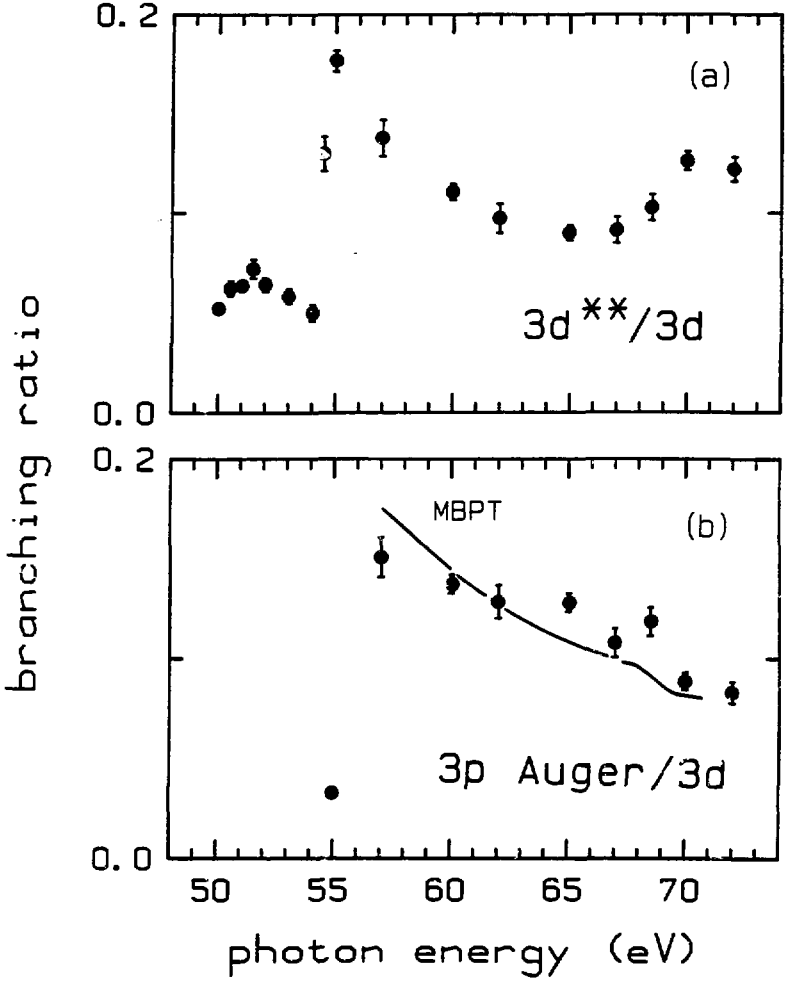

Fig. 3

XBL 832-7860

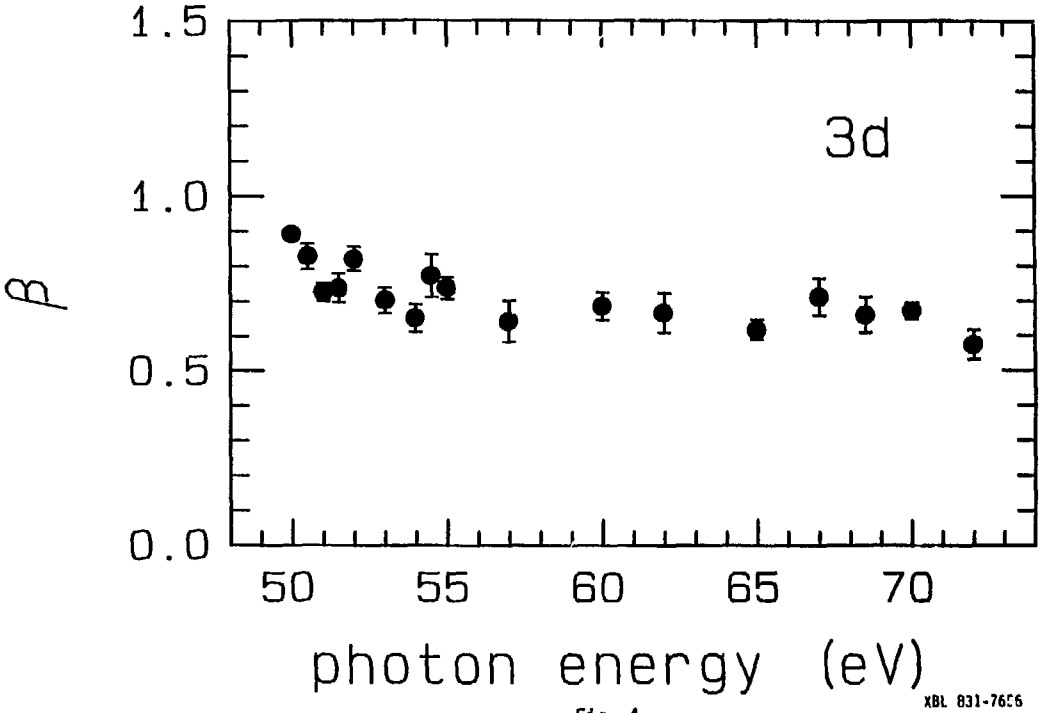

Fig. 4

XBL 831-7656

Acknowledgements

I would like to thank my research director, Dave Shirley, for his support, for his scientific insight, and for allowing me to pursue experiments of my choice.

All of the experiments in this thesis were carried out in collaboration with others: Dennis Lindle, Steve Southworth, and Carlton Truesdale, the students with whom I have worked for the longest period of time; Uwe Becker, Hans Kerkhoff, Bill Brewer, and Shige Owaki, who were visitors in our lab; and Phil Heimann and Trish Ferrett, who are new students in our research group. I am grateful to these individuals for their help and encouragement.

I would like to acknowledge Mike White and Dick Rosenberg, who first introduced me to photoelectron spectroscopy; Dennis Trevor, who provided invaluable advice for many years; and Tom Hayhurst, who helped me with the ab initio calculations.

I would also like to acknowledge Jim Pollard, Barbara Moriguchi, Wini Heppler, and the other members of the Shirley group for the help and camaraderie that they provided.

I received expert advice and technical assistance from the support staff at LBL in particular from Joe Katz, Bill Wilkie, and the mechanical engineers and machinests in building 70A. I would also like to thank the staff at SSRL for all of their help.

I thank my family for their love and support and my friends in Berkeley (particularly my traveling companions and the residents of Berryman House), whose companionship I enjoyed through these years.